



Eidgenössische Technische Hochschule Zürich  
Swiss Federal Institute of Technology Zurich



CRANFIELD UNIVERSITY

**Alejandro Valverde López**

**BENDING-TWIST SHAPE ADAPTATION BY  
COMPLIANT CHIRAL SPAR DESIGN**

SCHOOL OF AEROSPACE, TRANSPORT AND MANUFACTURING

MSc THESIS

CRANFIELD UNIVERSITY

SCHOOL OF AEROSPACE, TRANSPORT AND MANUFACTURING

MSc THESIS

Academic Year 2016-17

Alejandro Valverde López

Bending-twist Shape Adaptation By Compliant Chiral Spar Design

Supervisor: Dr. Simon Prince (Cranfield University)

Prof. Dr. P. Ermanni (ETH Zürich)

August 2017

This thesis is submitted in partial (45%) fulfillment of the requirements for the degree of Master of Science in Aerospace Dynamics

©Cranfield University 2017. All rights reserved. No part of this publication may be reproduced without the written permission of the copyright owner.

## **Abstract**

A project...

This project was realized within the Laboratory of Composite Materials and Adaptive Structures of the Eidgenössische Technische Hochschule Zürich (Swiss Federal Institute of Technology Zurich), under the supervision of Prof. Dr. P. Ermanni and the advisory of F. Runkel, K. Dominic and U. Fasel.

## **Acknowledgments**

To my mom

# Contents

Abstract . . . . .	i
Acknowledgments . . . . .	iii
List of figures . . . . .	x
List of tables . . . . .	xi
List of symbols . . . . .	xv
<b>1 Introduction</b>	<b>1</b>
1.1 Objetives 	1
<b>2 State-of-the-art</b>	<b>2</b>
2.1 Morphing aircraft . . . . .	2
2.2 Compliant chiral structure . . . . . 	6
2.3 Chiral wing rib . . . . .	9
2.4 Bending-Twist shape adaptation by compliant structural designs . . . . .	11
2.5 Rationale for the thesis . . . . .	14
<b>3 Wing-box model</b> 	<b>15</b>
3.1 Introducio 	15
3.2 Concept . . . . .	15
3.3 Analytical model . . . . .	17

3.4	Computational model . . . . .	19
3.4.1	Sub-parts and parametrization of the model . . . . .	21
3.4.2	Model mesh . . . . .	33
3.4.3	Attachment points modeling . . . . .	34
3.4.4	Parametric study method . . . . .	41
<b>4</b>	<b>Model analysis</b> 	<b>42</b>
4.1	Introduction . . . . .	42
4.2	Parametric study on the analytical model . . . 	42
4.2.1	Results . . . . .	42
4.2.2	Discussion of the results . . . . .	50
4.3	Computational model analysis . . . . .	50
4.3.1	Connection between the chiral lattice and the wing-box skin . . . . .	50
4.3.2	Mesh . . . . .	50
4.3.3	Load definition . . . . .	52
4.3.4	Boundary condition . . . . .	53
4.3.5	Results analysis . . . . .	54
4.3.6	Nonlinear problem and automatic stabilization . . . . .	55
4.3.7	Inner ribs . . . . .	59
<b>5</b>	<b>Simulations results</b> 	<b>62</b>
5.1	Introduction . . . . .	62
5.2	General response characterization . . . . .	62
5.3	Parametric study on the computational model . . . . .	66
5.3.1	Wing-box thickness . . . . .	66
5.3.2	Number of unit cells in the chiral lattice . . . . .	71

5.3.3 Chiral lattice parameters . . . . .	74
---	----

<b>Bibliography</b>	<b>90</b>
---------------------	-----------

<b>Appendix A</b>	<b>91</b>
-------------------	-----------

# List of Figures

2.1	Wright Brothers 1899 kite . . . . .	3
2.2	Shape morphing wing classification . . . . .	4
2.3	Chiral structure of rotatable nodes and bendable ligaments . . . . .	6
2.4	Experimental Poisson's ratio $\nu$ as a function of axial compressive strain on a chiral honeycomb . . . . .	7
2.5	Chiral cell elements showing different ligaments curvatures . . . . .	8
2.6	Investigated configurations for the truss-core of chiral topology . . . . .	9
2.7	Manufactured prototype of a truss-core airfoil with chiral topology . . . . .	9
2.8	Chiral sail concept . . . . .	10
2.9	Inner structure of the experimental wing build to test the concept of adaptive wing-box . .	12
2.10	Plate buckling on one of the webs of the wing-box beam . . . . .	13
3.1	Working principle for the adaptive beam . . . . .	16
3.2	Chiral unit cell undergoing buckling instabilities . . . . .	17
3.3	Schematic view of the beam closed section . . . . .	18
3.4	General assembly configuration for the computational model . . . . .	20
3.5	Default normals and thickness direction for continuum shell elements in Abaqus . . . .	20
3.6	Overview of the chiral lattice part . . . . .	22
3.7	Division of the lattice structure in cell units . . . . .	22
3.8	Internal parameters of the chiral lattice structure . . . . .	23

3.9	Pictured of the manufactured chiral lattice nodes . . . . .	24
3.10	Kinematic coupling constraint . . . . .	25
3.11	Overview of the elements that are involved in the coupling condition at the lattice nodes .	26
3.12	Overview of the tyre part . . . . .	27
3.13	Internal parameters of the tyre part . . . . .	28
3.14	Overview of the connection between tyre and lattice node . . . . .	28
3.15	Overview of the wing-box in C-profile part . . . . .	29
3.16	Internal parameters of the wing-box in C-profile part . . . . .	30
3.17	Internal parameters of the two different ribs parts . . . . .	31
3.18	Internal parameters of the two different ribs parts . . . . .	33
3.19	Detail of the connection between the lattice nodes and the skin . . . . .	34
3.20	Blocked translation and free rotation connection between the lattice nodes and the skin .	35
3.21	Free translation and rotation connection between the lattice nodes and the skin . . . . .	36
3.22	Coupling condition between the lattice node and the wing-box skin through tyre . . . . .	37
3.23	Local reference system at the lattice nodes . . . . .	39
3.24	Coupling condition between the lattice node and the wing-box skin through a local reference system . . . . .	40
3.25	Flow chart showing the execution of the parametric study code . . . . .	41
4.1	Influence of the cross-sectional aspect ratio $B/H$ on the torsional stiffness $GI_t$ . . . . .	43
4.2	Influence of the cross-sectional aspect ratio $B/H$ on the dimensionless shear centre position $y_{SC}/B$ . . . . .	44
4.3	Influence of the cross-sectional aspect ratio $B/H$ on the flexural stiffness $EI_y$ . . . . .	44
4.4	Influence of the cross-sectional aspect ratio $B/H$ on the deflection compliance . . . . .	45
4.5	Influence of the cross-sectional aspect ratio $B/H$ on the torsional compliance . . . . .	45
4.6	Influence of the wall thickness ratio $t_2/t_1$ on the torsional stiffness $GI_t$ . . . . .	46
4.7	Influence of the wall thickness ratio $t_2/t_1$ on the dimensionless shear centre position $y_{SC}/B$	46

4.8	Influence of the wall thickness ratio $t_2/t_1$ on the flexural stiffness $EI_y$	47
4.9	Influence of the thickness ratio $t_2/t_1$ on the deflection compliance	47
4.10	Influence of the thickness ratio $t_2/t_1$ on the torsional compliance	48
4.11	Influence of the slenderness ratio $L/B$ on the deflection compliance	48
4.12	Influence of the slenderness ratio $L/B$ on the torsional compliance	49
4.13	Distorted mesh elements in the model	51
4.14	Boundary condition for the model	53
4.15	Path of mesh elements on the solution model	54
4.16	Force-displacement curve for various values of constant artificial damping factor	56
4.17	External work and static dissipation for a damping factor equal to $2 \times 10^{-5}$	57
4.18	External work and static dissipation for a damping factor equal to $2 \times 10^{-8}$	57
4.19	External work and static dissipation for a damping factor equal to $2 \times 10^{-9}$	58
4.20	Vertical displacement $v$ at the tip rib	59
4.21	Model response without the use of inner ribs nor automatic stabilization	60
4.22	Model response without the use of inner ribs with automatic stabilization	60
4.23	Model response incorporating inner ribs and without automatic stabilization	61
5.1	Baseline model response when the fraction of load applied equals to 63% of the prescribed load (700 N)	63
5.2	Baseline model response when the fraction of load applied equals to 80% of the prescribed load (700 N)	63
5.3	External work and static dissipation for a simulation of the baseline configuration	64
5.4	Force-displacement curve for the baseline configuration	65
5.5	Baseline model response when the fraction of load applied equals to 82% of the prescribed load (700 N)	65
5.6	Force-displacement curve for various values of the wing-box thickness	67
5.7	Detail of the force-displacement curve for various values of the wing-box thickness	68

5.8	Color contour representation of the total angular displacement of the mesh elements on the deformed structure for $t_{\text{box}} = 1.2 \text{ mm}$	69
5.9	Color contour representation of the total angular displacement of the mesh elements on the deformed structure for $t_{\text{box}} = 0.8 \text{ mm}$	69
5.10	Force that induces the structure to collapse as a function of the wing-box thickness	70
5.11	Force-displacement curve for various values of the number of unit cells in the transversal direction	72
5.12	Force-displacement curve for various values of the number of unit cells in the spanwise direction	73
5.13	Model response when the fraction of load applied equals to 96% of the prescribed load (700 N) and $N = 10$	73
5.14	Force-displacement curve for various values of the dimensionless chiral ligament eccentricity	75
5.15	Model response when the fraction of load applied equals to 100% of the prescribed load (700 N) and $\hat{e}_{\text{chiral}} = 0.1$	75
5.16	Force that induces the structure to collapse as a function of the chiral ligament eccentricity	76
5.17	Model response when the fraction of load applied equals to 72% of the prescribed load (700 N) and $\hat{e}_{\text{chiral}} = 0.0$	76
5.18	Model response when the fraction of load applied equals to 68% of the prescribed load (700 N) and $\hat{e}_{\text{chiral}} = 0.001$	77
5.19	Force-displacement curve for various values of the dimensionless chiral node depth	79
5.20	Model response when the fraction of load applied equals to 86% of the prescribed load (700 N) and $B_{\text{chiral}} = 30 \text{ mm}$	79
5.21	Model response when the fraction of load applied equals to 62% of the prescribed load (700 N) and $B_{\text{chiral}} = 10 \text{ mm}$	80
5.22	Force that induces the structure to collapse as a function of the chiral node depth	80
5.23	Force-displacement curve for various values of the chiral node radius	82
5.24	Model response when the fraction of load applied equals to 100% of the prescribed load (700 N) and $r_{\text{chiral}} = 12.5 \text{ mm}$	82
5.25	Model response when the fraction of load applied equals to 100% of the prescribed load (700 N) and $r_{\text{chiral}} = 17.5 \text{ mm}$	83

5.26	Force that induces the structure to collapse as a function of the chiral node depth . . . . .	83
5.27	Force-displacement curve for various values of the chiral ligament half length . . . . .	84
5.28	Force that induces the structure to collapse as a function of the chiral ligament half length	85
5.29	Force-displacement curve for various values of the chiral structure thickness . . . . .	86
5.30	Force that induces the structure to collapse as a function of the chiral structure thickness	87

# List of Tables

3.1	Parameters used for the lattice model . . . . .	23
3.2	Parameters used for the wing-box in C-profile model . . . . .	30
3.3	Parameters used for the ribs model . . . . .	32
5.1	Results from parametric study on the wing-box thickness . . . . .	67
5.2	Results from parametric study on the number of unit cells in the transversal direction . . .	71
5.3	Results from parametric study on the number of unit cells in the spanwise direction . . .	72
5.4	Results from parametric study on chiral ligament eccentricity . . . . .	74
5.5	Results from parametric study on chiral node depth . . . . .	78
5.6	Results from parametric study on chiral node radius . . . . .	81
5.7	Results from parametric study on chiral ligament half length . . . . .	84
5.8	Results from parametric study on chiral structure thickness . . . . .	86

ACTIVE FLEXIBLE WING

# List of symbols

$\hat{e}_{\text{chiral}}$	Dimensionless ligament eccentricity	
$\hat{x}$	Dimensionless coordinate in the spanwise direction ( $x/L$ )	
$\hat{y}$	Dimensionless coordinate in the transversal direction in the computational model ( $y_{\text{comp}}/H_{\text{box}}$ )	
$\hat{z}$	Dimensionless coordinate in the chordwise direction in the computational model ( $z_{\text{comp}}/W_{\text{box}}$ )	
$A$	Cross sectional area for the analytical model	[mm <sup>2</sup> ]
$A_{\text{rib}}$	Rib frame width	[mm]
$B$	Width of the cross section for the analytical model	[mm]
$B_{\text{chiral}}$	Chiral node depth	[mm]
$c$	Artificial damping factor	
$d_{\text{chiral-rib}}$	Gap between lattice and inner ribs	[mm]
$E, E_1, E_2, E_{\text{chiral}}, E_{\text{box}}, E_{\text{rib}}$	Young's modulus	[N/mm <sup>2</sup> ]
$e_{\text{chiral}}$	Ligament eccentricity	[mm]
$G, G_1, G_2, G_{\text{chiral}}, G_{\text{box}}, G_{\text{rib}}$	Shear modulus	[N/mm <sup>2</sup> ]
$H$	Height of the cross section for the analytical model	[mm]
$H_{\text{box}}, H_{\text{rib}}$	Height for the wing-box and the ribs	[mm]
$I_t$	Torsional constant	[mm <sup>4</sup> ]
$L$	Length of the beam for the analytical model	[mm]
$L_{\text{box}}$	Length of the wing-box in the spanwise direction	[mm]
$L_{\text{chiral}}$	Chiral ligament half length	[mm]

$M$	Number of unit cells in transversal direction	
$N$	Number of unit cells in spanwise direction	
$q_0$	Constant shear flow	[N/mm]
$q_c$	Close section shear flow	[N/mm]
$q_{\parallel}$	Open section shear flow	[N/mm]
$Q_z$	Force in direction of $z$	[N]
$r$	Radial position in the local cylindrical reference system	[mm]
$R_{\text{chiral}}$	Ligament eccentricity radius	[mm]
$r_{\text{chiral}}$	Chiral node radius	[mm]
$S_c$	Course mesh size	
$S_f$	Fine mesh size	
$S_{E_y}$	First moment of area	[N mm]
$t, t_1, t_2, t_{\text{chiral}}, t_{\text{box}}, t_{\text{rib}}$	Wall thickness	[mm]
$u$	Displacement along the $x$ direction	[mm]
$v$	Displacement along the $y$ direction	[mm]
$w, w_0$	Displacements in direction of $z$	[mm <sup>2</sup> ]
$W_{\text{box}}, W_{\text{rib,close}}, W_{\text{rib,open}}$	Width for the wing-box and the ribs	[mm]
$x$	Coordinate in the spanwise direction	[mm]
$y_{\text{ana}}, z_{\text{comp}}$	Coordinate in the chordwise direction for the analytical and computations reference systems	[mm]
$z$	Perpendicular position in the local cylindrical reference system	[mm]
$z_{\text{ana}}, y_{\text{comp}}$	Coordinate in the transversal direction for the analytical and computations reference systems	[mm]
$\nu, \nu_{\text{chiral}}, \nu_{\text{box}}, \nu_{\text{rib}}$	Poisson's ratio	
$\phi, \phi_{\text{tip}}, \tilde{\phi}_{\text{tip}}$	Twist angle	[deg]
$\Phi_y$	Flexural stiffness	[N mm <sup>2</sup> ]

$\theta$	Angular position in the local cylindrical reference system	[rad]
$\vartheta w, w_0$	Specific twist angle	[deg/mm]

### Abbreviations

AAW	Active Aeroelastic Wing
ABS	Acrylonitrile butadiene styrene
AFW	Active Flexible Wing
CAE	Complete Abaqus Environment
CFRP	Carbon Fibre Reinforced Plastic
CMAS	Composite Materials and Adaptive Structures Lab
ETH	Eidgenössische Technische Hochschule Zürich
FEM	Finite element method
NASA	National Aeronautics and Space Agency

# **Chapter 1**

## **Introduction**

The aim of this project is to investigate the possibilities of a novel concept of airfoil twist morphing.

### **1.1   Objectives**



# Chapter 2

## State-of-the-art

In the present chapter, a review of the current technologies related to the topic of this work will be done. Firstly, a review of different morphing wing technologies will be introduced. Secondly, a particular focus on the state-of-the-art of technology exploit in the current project will be presented.



### 2.1 Morphing aircraft

The interest in morphing of the aerodynamic surfaces has accompany aerospace history since the beginning. Since the first heavier-than-air flight in 1903, when the Wright Brothers designed and build a powered heavier-than-air aircraft that achieved the first controlled and sustained flight. Their concept of aircraft did not provide importance to built-in stability but absolute control of the aircraft by the pilot. For this reason, they deliberatively designed their first aircraft with anhedral wing that make it dynamically unstable to perturbations in sideslip but more maneuverable in the lateral direction. In order to achieve roll control, they decided to incorporate a mechanism that would allow the wings to twist by pulling from cables, as it can be seen in Figure 2.1. This was the first ever use of morphing of an aerodynamic surface for aircraft control. Since them, the necessity of enhanced performance and higher airspeed brought the requirement of stiffer wing structures to avoid aeroelastic instabilities.



On conventional aircraft, the need to modify the airflow around the airfoil at different flight conditions is achieve through discrete hinged mechanics such as flaps and ailerons. This mechanism perform well in a limited range around the design point while the outside this range, they have a negative influence in the aerodynamics. The necessary discontinuities that these elements produce on the surface, advance the boundary layer transition point from laminar to turbulent regime. Being able to modify the airflow without discontinuities on the surface would come along with notable reductions in parasite drag and therefore in fuel consumption.



New interest has raised in the recent years in aircraft morphing, mainly due to the appearance of new smart materials that allow more efficient mechanical design that do not necessarily incur in weight

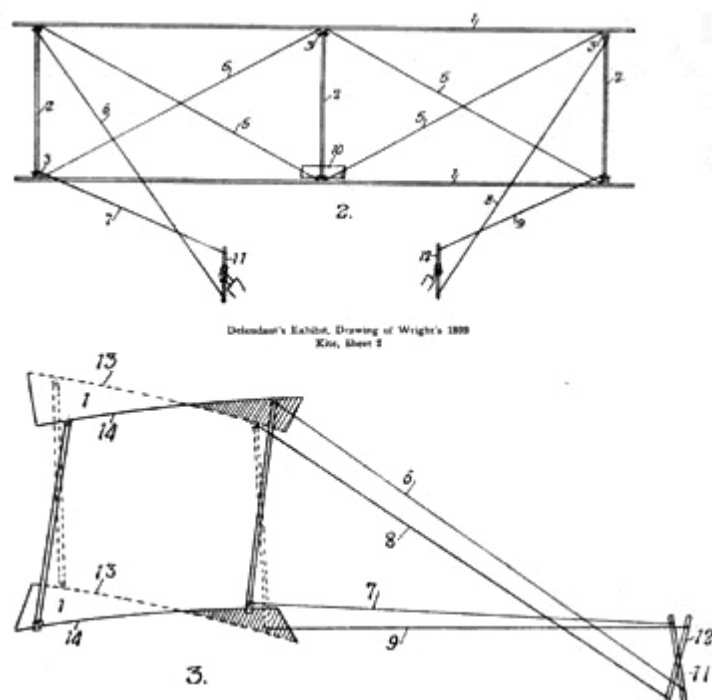


Figure 2.1: Wright 1899 kite: front and side views, with control sticks. Wing-warping is shown in lower view. [1]

increments [2]. Another reason that is pushing forward new aircraft morphing technologies is that missions today are in need of higher aircraft versatility to decrease operational costs in the commercial aviation field and aim to smaller and more distributed targets in the military field. For example, Airbus 

A general classification of different wing morphing concepts can be seen in Figure 2.2: planform modification through variation of sweep angle, span or chord; out-of-plane alteration involving twist, dihedral angle and spanwise bending, and airfoil adjustment achieved by modifications of the airfoil chamber and/or thickness. Under this classification, the morphing technology that is the focus of the work presented in this thesis is located under the out-of-plane branch and twist modification.

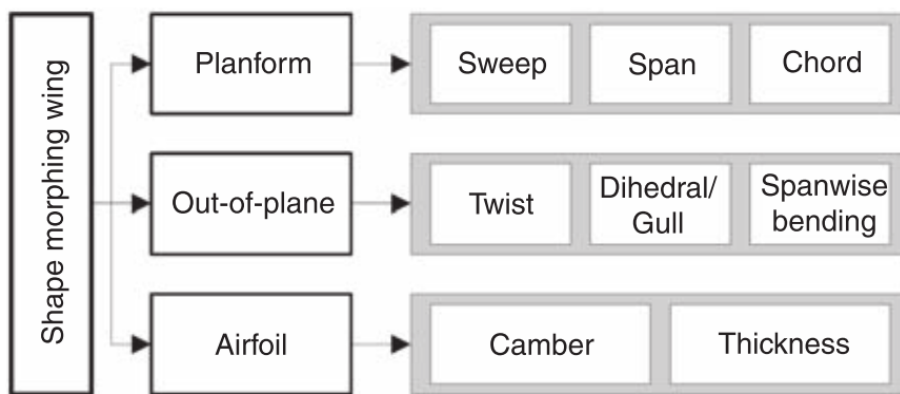


Figure 2.2: Shape morphing wing classification. [4]

In the field of wing morphing through active aeroelastic concepts, the pioneer program of the Active Flexible Wing (AFW) was developed by Rockwell International in the 1980s [5]. Under this program, a design of an aircraft where the wing aeroelastic twist was used to produce the required roll moments for control was generated. This enabled the aircraft to operate at dynamic pressures beyond those where conventional ailerons suffer from the appearance of reversal aeroelastic instabilities. Later, NASA continued with the AFW concept within their Active Aeroelastic Wing (AAW) project which used a modified F-18 fighter named X-53 to perform flight test and assess the viability of the proposed concept. The X-53 had its wings modified to reduce the torsional stiffness and had additional actuators added to operate the outboard leading-edge flaps separately from the inboard leading-edge surfaces [6]. Rolling moment was obtained by aeroelastic twist of the wing using trailing-edge control surfaces and leading-edge flaps. 

Following that initial attempts to deepen into the possibilities of wing twist morphing aircraft, many additional research literature can be found for other approaches. Many of those, consisted in modifying the wing properties by active means, i.e.: incorporating actuators that introduce energy into the system. However, wing twist morphing designs may also benefit from geometrically flexible structures if the aeroelastic energy from the airstream can be used to activate the shape changing mechanics. Such an approach may lead to passive morphings strategies that are always preferred since no additional energy is necessary to be introduced into the system and the usual weight penalties of morphing may be avoided 

if no additional actuators are needed. In such an approach the work presented in this thesis is embedded.

## 2.2 Compliant chiral structure

~~As mentioned in the introduction, it is the interest of this work to exploit the capabilities of material~~ with negative Poisson's ratio. Such materials expand laterally when stretched and contract laterally when compressed. In [7], R. Lakes proposed that negative Poisson's ratios can result from a hexagonal microstructure of rotatable nodes and bendable ligaments such as the one shown in Figure 2.3. Such structures are known as non-centrosymmetric, hemitropic, or chiral; they are distinguishable from their mirror image; that is, they cannot be superposed onto them and they are not isotropic.

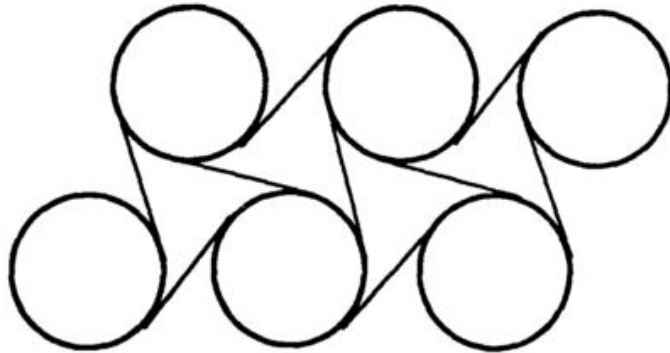


Figure 2.3: Chiral (noncentrosymmetric) hexagonal microstructure of rotatable nodes and bendable ligaments. Poisson's ratio is negative. [7]

In [8], experimental results showed that the a honeycomb chiral structure exhibited a Poisson's ratio of -1 for ~~deformations in plane~~. Indeed, this behavior was maintained over a significant range of strain, as shown in Figure 2.4, and therefore verifying that Poisson's ratio is independent upon the strain, in agreement with theory.

In [9] the properties of a chiral honeycomb are investigated, a manufacturing process using composite materials is proposed and the increase in the performance of using such materials is shown. Also, the experiments carried out allowed to characterize the possible failure modes of this structures and the nonlinear response when large displacements occur.

~~Until that moment~~, most of the work was concentrated in studying the in-plane behavior of the chiral structures. Then, in [10] the flatwise compression behavior of the chiral structures is investigated through FE modeling and simply analytical relations. This is the first consideration of buckling in a chiral structure in some way, in this case it was the out-of-plane buckling behavior based on the similar works presented in [11] and [12] for honeycomb structures. This research was extended by experimental studies in [13] and an anelastic characterisation of the buckling phenomena is presented in [14]. The use of controlled buckling for chiral honeycombs under a general macroscopic in-plane stress state was more recently investigated from a theoretical point of view in [15].

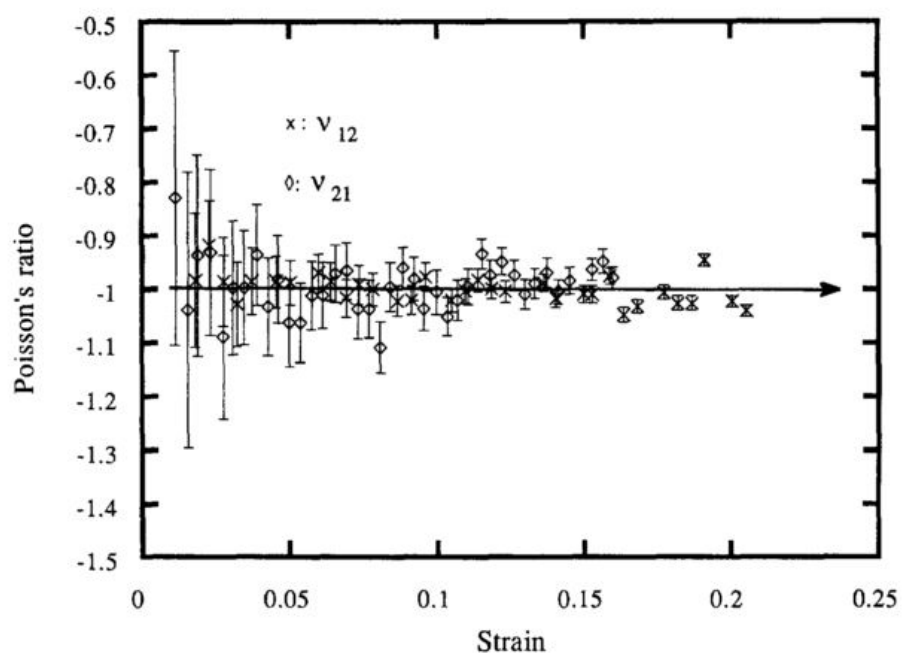


Figure 2.4: Experimental Poisson's ratio  $v$  as a function of axial compressive strain on a chiral honeycomb. The error bars represent inaccuracies due to the measurement resolution. [8]

Within the research undertaken at the Laboratory for Composite Materials and Adaptive Structures (CMAS) of the ETH Zürich in the field of variable stiffness structures, a new design for the ligaments of the chiral structures has been proposed. This consists in the introduction of curvature into the chiral ligaments, as shown in Figure 2.5(b). Each ligament posses double eccentricity which changes orientation at the centerline of it, in compliance with a equivalent connection with the cylinders located at the extremes [16]. Experimental evaluation of the mechanical response of such structures is evaluated.

This new design of the ligaments will provide additional tailorability over the buckling phenomena occurring on the lattice ligaments. This configuration is the one chosen for the chiral structure that is used in the concept presented in this work.

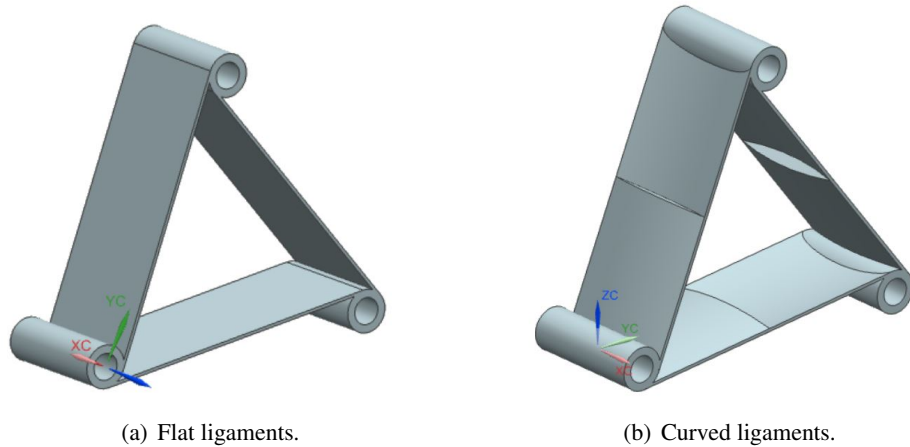


Figure 2.5: Chiral cell elements showing different ligaments curvatures. [16]

## 2.3 Chiral wing rib

Different approaches have been followed to exploit the particular characteristics of chiral structures on aerodynamic elements such as airfoils. In [17] a truss-core configuration such as the one shown in Figure 2.6(a) with chiral topology was utilized to design an airfoil for automotive competitions. The concept  exploit the elastic deformation of the chiral lattice to modify the airfoil mean chamber line and thus modifying the pressure distribution as required for the current desired performance of the car. In [18], a similar configuration was investigated by weakly coupled structural and CFD models, and the local and global deformations were characterized by consideration of the macroscopic chiral configuration. A prototype of the proposed design, as shown in Figure 2.7, was manufactured and tested in [19]. Results showed a remarkable tailoring of the chamber morphing performance by means of a limited number of parameters which define the core geometry. The dynamic properties of such chiral truss-core assemblies were investigated in [20].

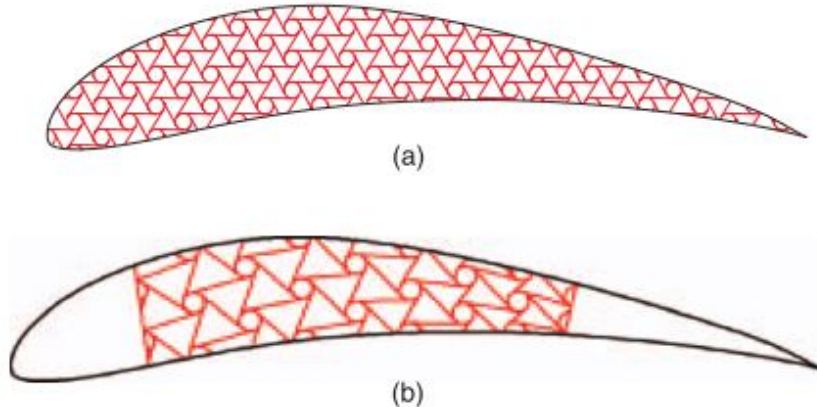


Figure 2.6: Investigated configurations for the truss-core of chiral topology. [18]

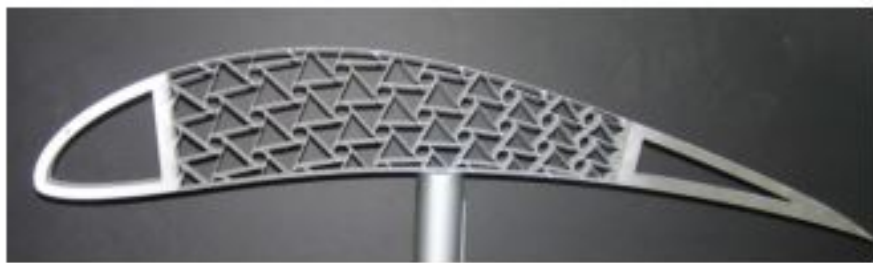


Figure 2.7: Manufactured prototype of a truss-core airfoil with chiral topology. They were manufactured in aluminum, using water-jet cutting techniques. [19]

~~In the recent years~~, A. Airolidi developed the “chiral sail” concept in [21] which exploits the chiral

topology of a chiral network embedded into the airfoil rib. The pressure difference between the upper and lower parts of the airfoil promotes the chamber variation as shown in Figure 2.8 and amplifying the lift when the angle of attack increases. This concept was implemented and validated by testing a demonstrator in [22]. The experimental side of this work showed the difficulties of manufacturing such complex structures.

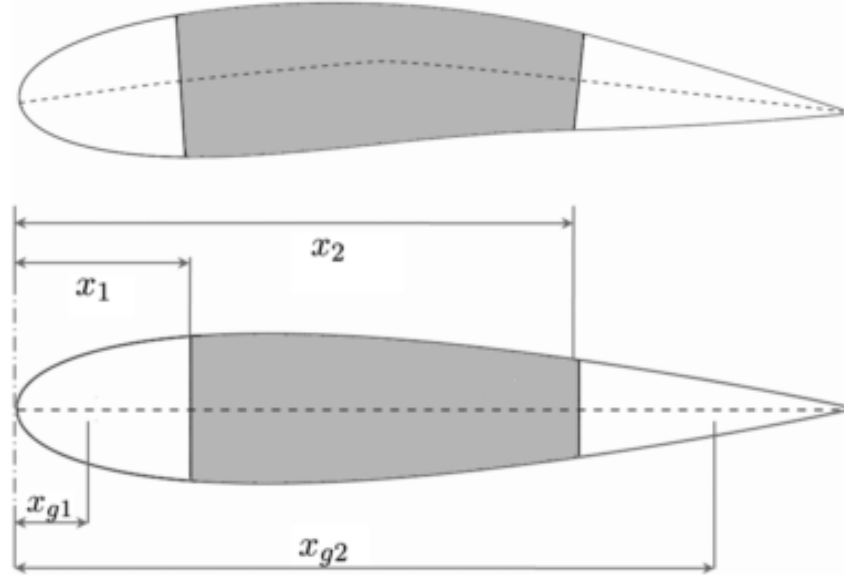


Figure 2.8: Chiral sail concept. The rib of the airfoil is constituted of a network of chiral unit cells. [21]

## 2.4 Bending-Twist shape adaptation by compliant structural designs

Following a different approach to achieve twist morphing compared to those presented in last section, W. Raither proposed in [23] a novel concept of adaptive aeroelastic tailoring by means of the wing-box torsional stiffness modification. In order to achieve this, the shear stiffness  $G_t$  of one of the webs that conform the wing-box beam is modified. This induces the section's shear centre shifting, which provides an additional torsional deformation for a constant load. This concept is later explained in Section 3.2 as the same working principle is used for the technology presented in this work.

Implementation of the proposed principle required ~~for a material that would provide~~ controllable in-plane shear modulus. A possible solution is proposed in [24] and consisted in the use of electro-bonded laminates that vary its bending stiffness by means of electrostatic forces applied different at points of the structure. Another approach is presented in [25], and exploits the time-variable lamination in laminate composite shells provided by the temperature dependence of the elastic modulus of polymers in proximity of their glass transition. Therefore, the proposed concept consists on a semi-passive approach since some energy needs to be spent for the activation of the adaptive interfaces. In [26] the demonstrator shown in Figure 2.9 was built to show the viability of this last approach.

Finally, in [27] the variation of in-plane shear modulus is proposed that can be achieved by inducing elastic instabilities on one of the webs of the wing-box. The component is manufactured with a particular material anisotropy utilizing unidirectional CFRP. The appearance of plate buckling at the root on the specially designed web, as shown in Figure 2.10, induces the shear centre location shifting and the torsional stiffness of the structure, thus leading to a purely passive bending-twist coupling. In [28], the mechanical response was investigated using FE simulations and experimental testing on a manufactured demonstrator of the concept.



Figure 2.9: Inner structure of the experimental wing build to test the concept of adaptive wing-box. [26]

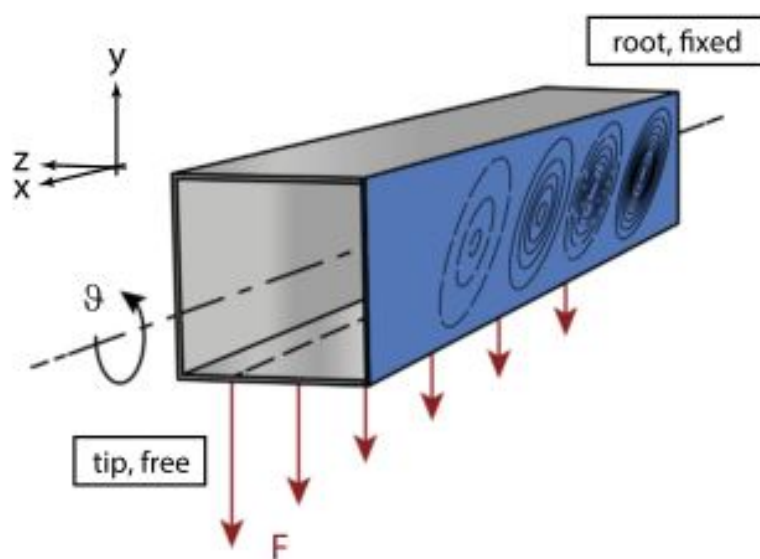


Figure 2.10: Plate buckling on one of the webs of the wing-box beam. The drawing shows a qualitative view of the buckling field. [27]

## 2.5 Rationale for the thesis

This thesis is embed within the current research that it is been carried out at CMAS in seek of wing twist morphing achieved through variable stiffness wing-box structures that acquire this property undergoing elastic instabilities.

As shown in the literature review  presented in [29] and [30], the use of buckling-induced technologies is a promising technique to achieve the desired behavior in recent developments of smart structures. Traditionally, elastic instabilities were avoided in the structural designs due to the significant loss of load-carrying capacity and large deformations occurring as a consequence of such an event. However, in the scope of the so called motion-related applications of buckling-induced technologies, the capability of small perturbations to generate sudden snapping behavior in elastic elements enables the structure to dynamically change its configuration, being this beneficial for applications such the one considered in the present work. Also, the possibility of minimizing the actuation force required during shape recovery due to the elastic state of the structure becomes interesting.

In parallel, when it comes to the bending-twist shape adaptation by compliant structural designs, some of the solutions already introduced in this chapter are able to modify the wing-box torsional stiffness for a pre-defined shape variation or are optimized for a given actuation lay-out, whereas the adoption of a structural concept such as a chiral lattice offers a wide range of possibilities in terms of tailoring. In particular, the chiral structures that posses curved ligaments are the design option for the concept proposed in this work. This design of chiral structure was already manufactured and tested in another project completed at CMAS [31].

Thereby, for the approach presented in this work, the working principle introduced by [23] and explained in Sections 2.4 is combined with the specific properties of the chiral structures exposed in Section 2.2 to conform the proposed principle. 

 In the scope of this thesis, a numerical model will be built of the whole wing-box assembly. The evolution of the buckling phenomena for in the structure will be characterized and the effect of the different design parameters on the structure pre-buckling and post-buckling response will be assessed. The aim is to provide a suitable computational environment to achieve in-deep understanding of the proposed working principle and assist the manufacture of a future demonstrator.

It is expected that the proposed technology will be suitable for environments where a rapid shape adaptation is required. Such applications may include to increase the critical speed for load alleviation purposes.

# Chapter 3

## Wing-box model

### 3.1 Introduction

In the present chapter the  model used for the wing-box design is presented. On first place, the working principle of the technology that it is the topic of this work is presented.

Next, the two different models developed to provide fully understanding of the structure response are presented. Firstly, a simple analytical model is presented to provide fast insight of the role of each of the parameters that characterize the ideal beam configuration of a beam with a web featuring variable stiffness properties. Important relevance is given to the section's shear centre  $y_{SC}$  shifting as this variable determinate the magnitude of the resulting torsional moment action on the beam as a result of a load acting on the beam's transversal plane.

Secondly, the computational model is introduced. The different constituting elements are explained together with the boundary conditions, loads and mesh that are used in the simulations

Finally, the program used to carry out automatic parametric studies is presented, together with its methodology.

### 3.2 Concept

As it was already introduced in last chapter, the proposed technology to achieve twist morphing through a variable torsional stiffness wing-box is based on the working principle presented in [23] and exploits the buckling characteristics of a lattice of chiral ligaments as a way of varying the stiffness on the adaptive spar of the wing-box.

The basic working principle consisted on employing profile beams in which the shear centre is shifted

as a result of the variable-stiffness capability of one of the webs. An schematic view of the working principle is shown in Figure 3.1 where an adaptive beam is displayed. In Figure 3.1(a), the four webs that constitute the rectangular profile of the beam have the same shear stiffness  $G_2 t_2 = G_1 t_1$ . The double symmetry characteristic of such a configuration indicates that the shear centre is located at the point where the two symmetry axes intersect. For this case, under a load applied on the shear centre, the beam experiences bending deformation with ~~null~~ twist. On the other hand, when considering the situation shown in Figure 3.1(b) where  $G_1 t_1 > G_2 t_2$ , the reduced shear stiffness of the adaptive web produces that shear centre moves along the  $y$  direction and towards positive values of  $y$ . In this case, if the load is maintained in the same application point as before, the beam experiences bending deformation and negative twist. Correspondingly, for the case shown in Figure 3.1(b) where  $G_2 t_2 > G_1 t_1$ , the shifting of the shear centre is towards negative values of  $y$  and the beam experiences a positive twisting under the prescribed load.

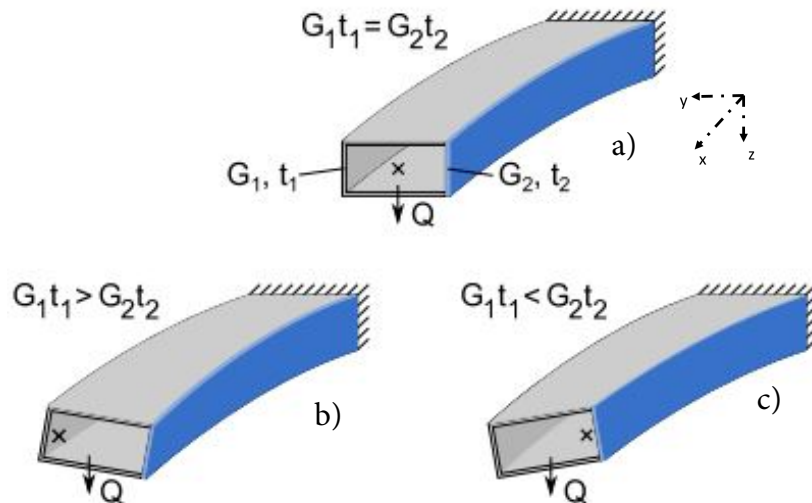


Figure 3.1: Working principle for the adaptive beam. [26]

The bending-twist coupling of the beam can therefore be controlled by the variable-stiffness web. The properties of the web can be modified by either adjusting the shear modulus  $G_2$  or the thickness  $t_2$  of the web.

In the technology presented in this work, the adaptive web is constituted of a lattice of chiral structures. On these elements, elastic buckling is intentionally induced and the resulting consequence is the reduction of the overall shear modulus  $G_2$  effectively introducing an effective shear modulus  $G_{2,\text{eff}} < G_1$ . An example of the chiral structure undergoing buckling instabilities can be seen in Figure 3.2. 

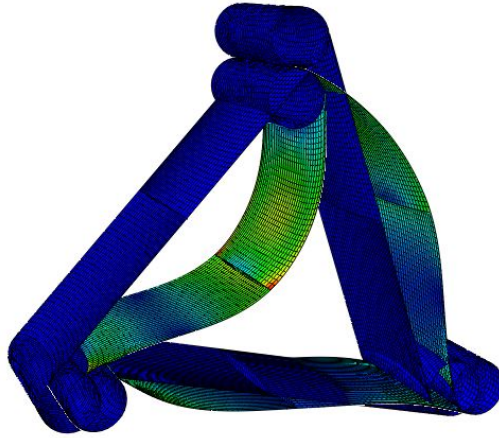


Figure 3.2: Chiral unit cell undergoing buckling instabilities. [16]

### 3.3 Analytical model

The analytical model of the wing-box is presented in the present section. An schematic view of the section of the beam can be seen in Figure 3.3. The main dimensions for the section are given by the height  $H$  and the width  $B$ . Such a structure if characterized by having three elements with identical thickness  $t_1$ , shear modulus  $G_1$  and Young's modulus  $E_1$ . For the element on the right, the adaptive web, the same parameters are  $t_2$ ,  $G_2$  and  $E_2$ , respectively.

As explained in Section 3.2, the shear stiffness  $Gt$  of the adaptive web can be modified by varying either thickness  $t$  or shear modulus  $G$ . For the remaining, it is assumed that  $t_1 = t_2 = t$  and therefore the thickness  $t$  will not be considered as a modifiable parameter on the adaptive web.

Now the bending-twisting coupling of the structure is investigated using well-known equation to describe the elastic behaviour of thin-wall beam elements. Based on the analytical approach to the problem of a beam bending-twisting coupling followed in [23], it is known that warping can be neglected for a configuration like the one presented in this section.

The bending displacement of the structure is therefore given by Equation 3.1 which is a solution of the well-known Bernoulli-Euler equation for a beam:

$$w_b = \frac{QL^3}{6\Phi_y} \left( -\frac{x^3}{L^3} + \frac{3x^2}{L^2} \right), \quad (3.1)$$

where  $w_b$  is the displacement along the  $z$  direction and  $\Phi_y$  is the flexural stiffness given by Equation 3.2:

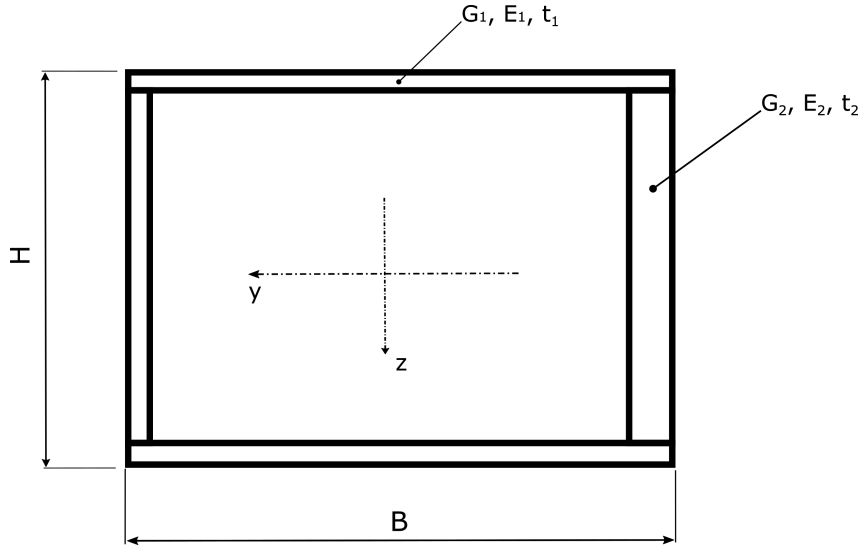


Figure 3.3: Schematic view of the beam closed section. The dimensions are given by the width  $B$  and the height  $H$ . For the upper, lower and left elements, the wall thickness, shear modulus and the Young's modulus are given by  $t_1$ ,  $G_1$  and  $E_1$ , respectively. For the right element, the same parameters are given by  $t_2$ ,  $G_2$  and  $E_2$ .

$$\Phi_y = \int \int E(y, z) z^2 dy dz. \quad (3.2)$$

On the other hand, the twist of a beam with closed section can be obtained from the St. Venant expression for the specific twist  $\vartheta$ , which is shown in Equation 3.3:

$$\vartheta = \frac{d\phi}{dx} = \frac{M_t}{4A_0^2} \oint \frac{ds}{Gt}, \quad (3.3)$$

where  $A_0$  represent the area enclosed by the profile's wall midline,  $\phi$  is the twist of the beam and  $M_t$  is the torsional moment applied. Additionally, the torsional stiffness for the closed section under study is given by the Equation 3.4:

$$GI_t = \frac{4A_0^2}{\oint \frac{ds}{G(s)t(s)}}. \quad (3.4)$$

In order to calculate the specific twist  $\vartheta$ , it is necessary to evaluate the shear centre position  $y_{SC}$  for a given configuration. In order to achieve this, evaluation of the shear flow distribution in the section also needs to be undertaken. To calculate the shear flow  $q(s)$ , the profile can be considered to be cut at one point, resulting on a opened section. The shear flow  $q_{||}(s)$  for this case can be calculated using Equation 3.5. The corresponding shear flow for a closed section can be obtained using the Equation 3.6:

$$q_{||}(s) = -\frac{Q_z}{\Phi_y} S_{E_y}(s), \quad (3.5)$$

$$q_C(s) = q_{\parallel}(s) + q_0, \quad (3.6)$$

where  $Q_z$  is the force applied in the z direction and  $S_{E_y}$  is the so called static moment or first moment of area, which is calculated through the integral shown in Equation 3.7. Also, the variable  $q_0$  represents the shear flow at the boundary that results from the torsion of the beam and can be calculated using the Equation 3.8:

$$S_{E_y}(s) = \int_0^s E(s)t(s)z(s)ds, \quad (3.7)$$

$$q_0 = \frac{Q_z \oint_s \frac{S_{E_y}(s)}{G(s)t(s)} ds}{\Phi_y \oint_s \frac{1}{G(s)t(s)} ds}. \quad (3.8)$$

Now, the shear centre position in the beam transversal section will be calculated for the case of open section. Given that beam mechanical properties and geometrical dimensions are symmetric around y axis, the shear centre position in the z axis will be  $z_{SC} = 0$ . On the other hand, the shear centre position in the y axis will be given by the Equation 3.9:

$$y_{SC,open} = \frac{1}{Q_z} \oint_s q_C(s)r(s)ds, \quad (3.9)$$

where  $r$  represents the perpendicular distance to the coordinate origin.

Now, it is necessary that equilibrium exists between the torsional moment due to the shift of the shear centre (caused during the opening of the profile) and the moment due to the torsional shear flow of the closed profile. This condition can be mathematically expressed through Equation 3.10:

$$\begin{aligned} M_t &= Q_z(y_{SC,open} - y_{SC,closed}) \\ &= 2A_0q_0. \end{aligned} \quad (3.10)$$

Finally, the total shear flow  $q(s)$  results from the superposition of the shear flow of the open profile  $q_C$  and the constant shear flow due to torsion  $q_0$ , as shown in the Equation 3.11:

$$q(s) = q_C(s) - q_0. \quad (3.11)$$

### 3.4 Computational model

The computational model of the wing box was built using Abaqus CAE commercial software. It consisted on three main elements: the wing-box with C-profile, the lattice constituted of the chiral elements,

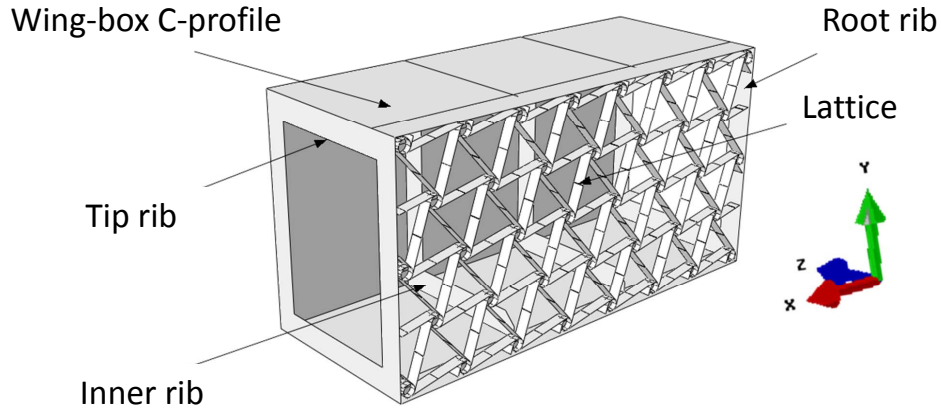


Figure 3.4: General assembly configuration for the computational model. The different parts for the general configuration include the wing-box profile, the lattice and the pair of ribs located at the tip and the root of the wing-box.

a closed rib at the tip of the box and a closed rib at the root of the box. A general overview of the assembly of the different parts can be seen in Figure 3.4.

The discretization of the structural element was done using continuum shell elements as the basic constituting part. An sketch of a continuum shell element as defined in Abaqus can be seen in Figure 3.5.

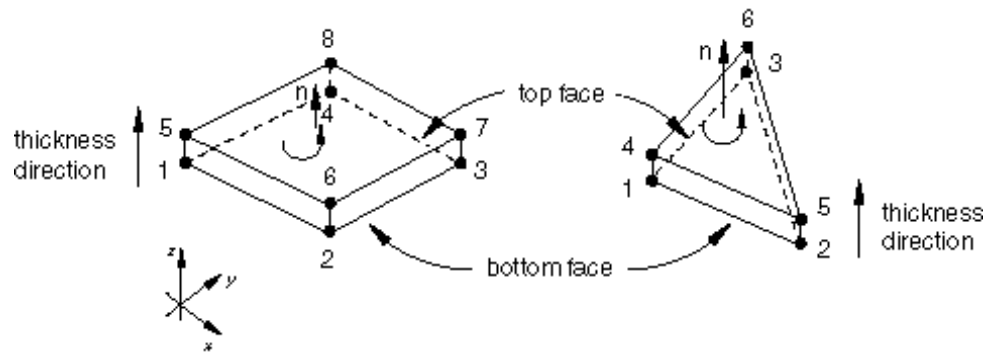


Figure 3.5: Default normals and thickness direction for continuum shell elements in Abaqus. [32]

### 3.4.1 Sub-parts and parametrization of the model

#### Lattice of chiral elements

The model of the lattice structure is constituted of a series of interconnected lattices and nodes. An overview of the corresponding part can be seen in Figure 3.6. The lattice structure is divided in an integer number of unit cells in the longitudinal (spanwise) and transversal directions. These parameters are identified with the variables  $N$  and  $M$  for the longitudinal and transversal directions, respectively. In Figure 3.7, an sketch of the internal division for  $N = 8$  and  $M = 3$  is shown. It displays a set of horizontal rectangles that represent each of the transversal  $M$  divisions while the set of vertical rectangles correspond to each of the  $N$  longitudinal divisions.

Furthermore, the internal geometry in the chiral lattices is determined by a number of parameters: the thickness  $t_{\text{chiral}}$ , the ligament eccentricity  $e_{\text{chiral}}$ , the ligament half length  $L_{\text{chiral}}$ , the lattice node depth  $B_{\text{chiral}}$  and the lattice node radius  $r_{\text{chiral}}$ . The geometrical meaning of these variables can be seen in Figure 3.8. The thickness  $t_{\text{chiral}}$  applies for both the ligaments and the lattice nodes geometries. The eccentricity  $e_{\text{chiral}}$  will be expressed as the dimensionless parameter  $\hat{e}_{\text{chiral}}$  which is obtained from  $\hat{e}_{\text{chiral}} = e_{\text{chiral}}/B_{\text{chiral}}$ .

In the sketch shown in Figure 3.8 an additional dimension variable appears, the ligament eccentricity radius  $R_{\text{chiral}}$  which is dependent on the ligament eccentricity  $e_{\text{chiral}}$  and the lattice node depth  $B_{\text{chiral}}$  as shown in Equation 3.12.

A summary of all the parameters introduced to characterize the chiral lattice structure together with their units and nominal values is shown in Table 3.1.

$$R = \frac{e_{\text{chiral}}^2 + \frac{B_{\text{chiral}}^2}{4}}{2e_{\text{chiral}}} \quad (3.12)$$

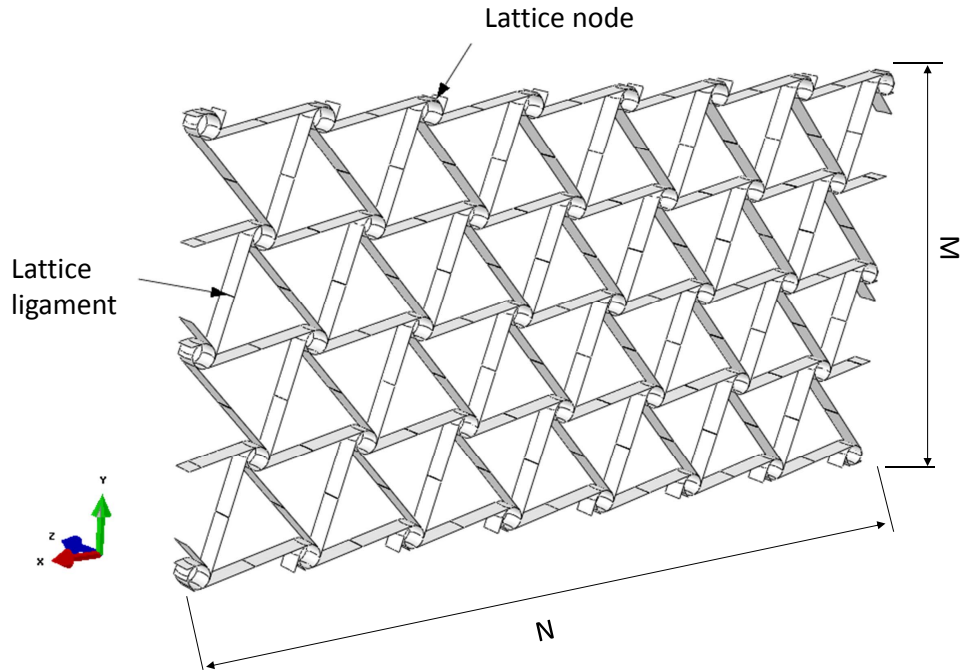


Figure 3.6: Overview of the chiral lattice part. The parameters  $N$  and  $M$  represent the number of unit cells in the longitudinal (spanwise) and transversal directions, respectively.

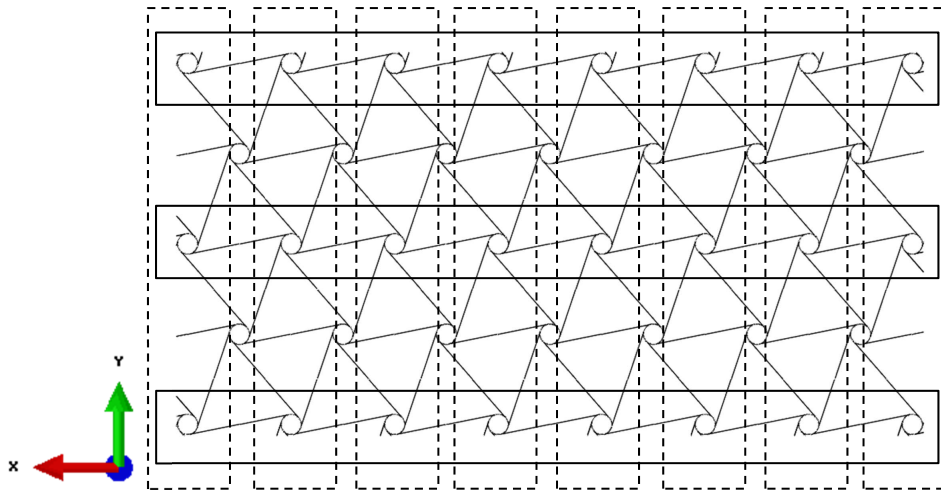


Figure 3.7: Division of the lattice structure in cell units. The sketch shows a lattice with  $N = 8$  and  $M = 3$ . The set of horizontal rectangles represent each of the transversal  $M$  divisions while the set of vertical rectangles correspond to each of the  $N$  longitudinal divisions.

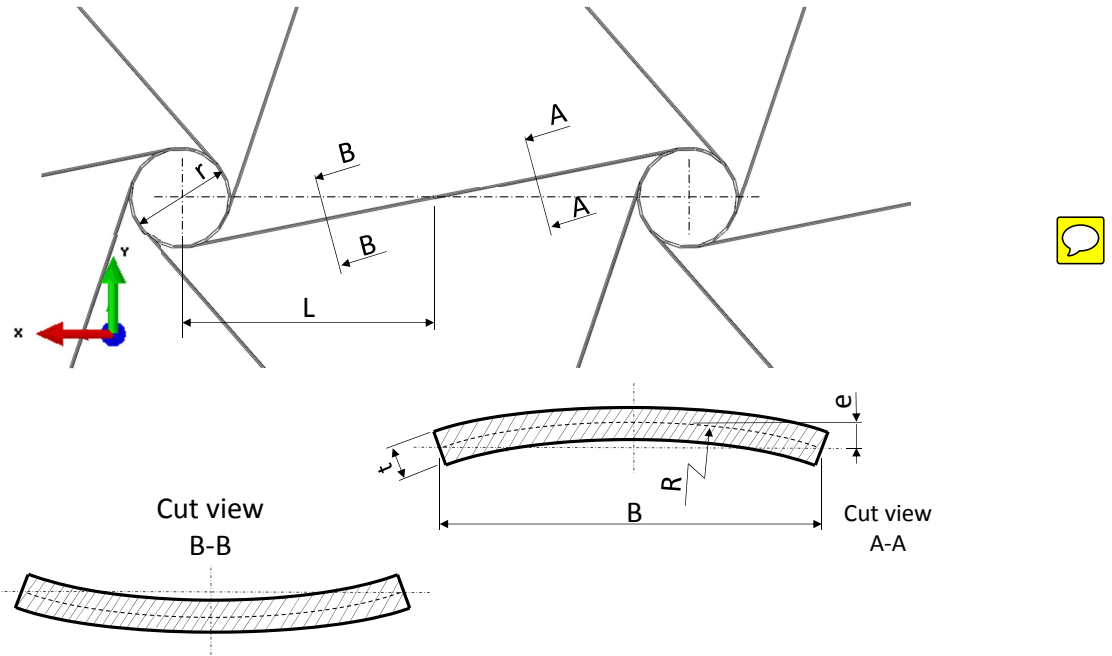


Figure 3.8: Internal parameters of the chiral lattice structure. The geometry is characterized by the the ligament eccentricity  $e_{\text{chiral}}$ , the ligament half length  $L_{\text{chiral}}$ , the lattice node depth  $B_{\text{chiral}}$ , the lattice node radius  $r_{\text{chiral}}$  and the thickness  $t_{\text{chiral}}$ . The ligament eccentricity radius  $R_{\text{chiral}}$  which is dependent on the ligament eccentricity  $e_{\text{chiral}}$  and the lattice node depth  $B_{\text{chiral}}$ , as shown in Equation 3.12

Parameter	Symbol	Units	Nominal value
<b>Dimensions</b>			
Number of unit cells in spanwise direction	$N$		8
Number of unit cells in transversal direction	$M$		3
Dimensionless ligament eccentricity ( $e/B$ )	$\hat{e}_{\text{chiral}}$		0.01
Node radius	$r_{\text{chiral}}$	mm	10
Node depth	$B_{\text{chiral}}$	mm	20
Ligament eccentricity radius	$R_{\text{chiral}}$	mm	250.1
Ligament half length	$L_{\text{chiral}}$	mm	50
Thickness	$t_{\text{chiral}}$	mm	0.5
<b>Material (ABS)</b>			
Young's modulus	$E_{\text{chiral}}$	N/mm <sup>2</sup>	3100
Poisson's ratio	$\nu_{\text{chiral}}$		0.3

Table 3.1: Parameters used for the lattice model. The mechanical properties of the material used correspond to ABS, which is a common thermoplastic polymer.

### Lattice nodes rigid body modeling

The lattice nodes is one of the essential parts of the lattice of chiral elements. These are allow to freely  rotate around its own axis. For the modeling, they are assumed to behave like a rigid body. In Figure 3.9, a closer look to the chiral nodes can be seen, showing two different approaches to manufacture a node that would behave like a rigid body compared with the rest of the structure.

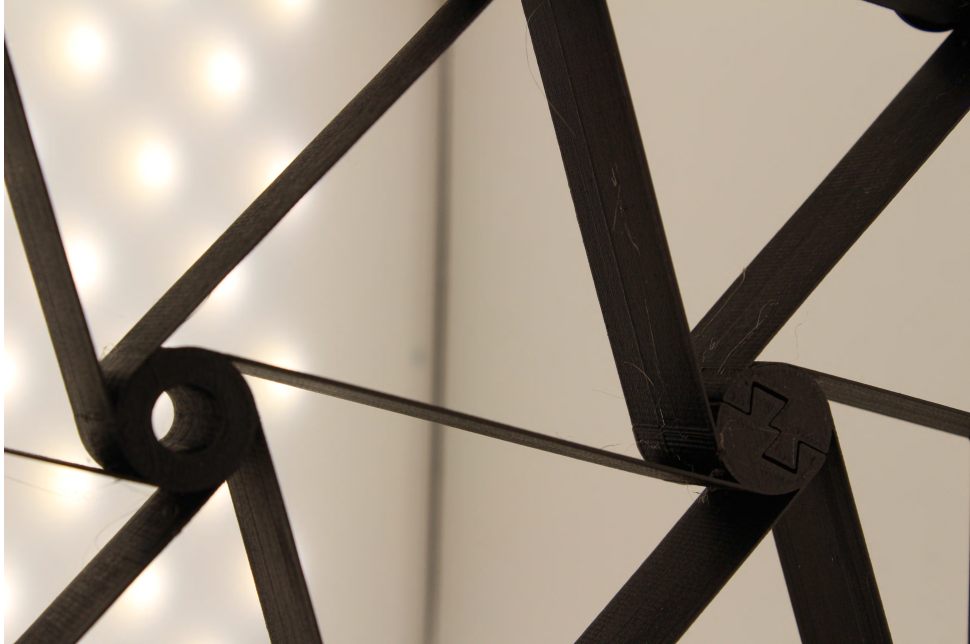


Figure 3.9: Pictured of the manufactured chiral lattice nodes. The figures shows two different approaches followed to manufacture the nodes. The one on the right was the standard one showing a cylinder with a thickness bigger than the thickness of the chiral ligaments  $t_{node} \gg t_{ligaments}$ . On the left, an alternative approach is followed in order to allow the assembly of the chiral lattice that is not manufactured as a unique piece. [31]

In the Abaqus model, different approaches were followed to create this element of the chiral lattice. The first one was to create a coupling condition using Abaqus corresponding module. In particular, a kinematic coupling was establish. A kinematic coupling constrains the motion of one or more coupling nodes, also called slave node or nodes, to the rigid body motion of a reference node, also called master node. They are imposed by eliminating degrees of freedom at the coupling nodes. In Figure 3.10, an example of a kinematic coupling can be seen.

For the considered case, the coupling nodes are those mesh nodes located faces of the lattice node and the master node is the reference point located in the center of the lattice node. In order to achieve the rigid solid behavior, all the degrees of freedom were coupled except from the translation displacements in the plane where the chiral lattice is contained, i.e. the translational displacement  $U_1$  and  $U_2$  of the plane  $X - Y$ . In Figure 3.11 an overview of this coupling condition can be viewed.

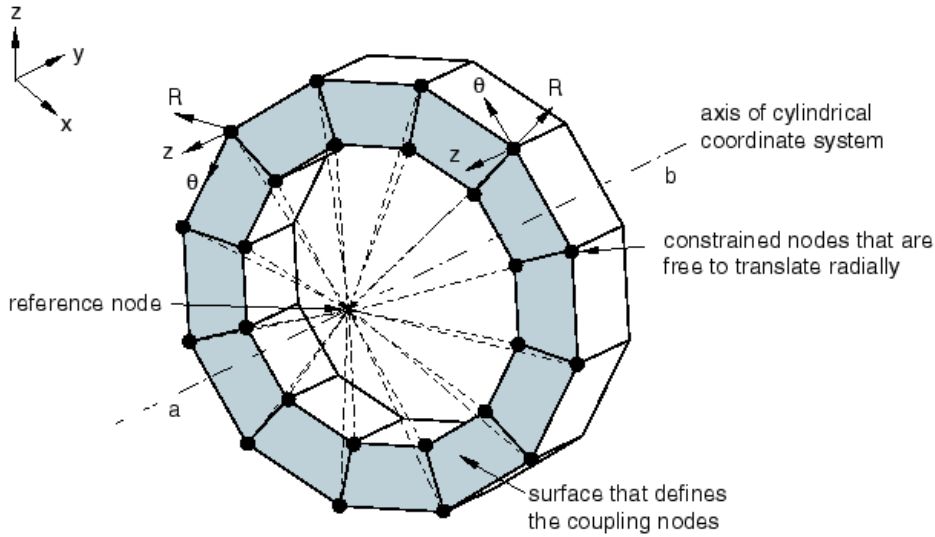


Figure 3.10: Kinematic coupling constraint. The sketch illustrates the use of a kinematic coupling constraint to prescribe a twisting motion to a model without constraining the radial motion. In this case, a local cylindrical reference system is used and the constrained nodes have two degrees of freedom coupled to those of the reference node, the angular position  $\theta$  and the position along the  $z$  axis. The coupling nodes are therefore free to translate radially, varying  $R$ . [32]

Another approach consisted in inserting an addition part inside the lattice nodes to add rigidity to the element. The proposed design of such a part, which will be referred as tyre from now on, can be seen in Figure 3.12. The internal dimensions of this element are shown in Figure 3.13. This dimensions were dependent on parameters of the chiral lattice. **In other words**, the thickness of the tyre was equal to that of the chiral lattice  $r_{\text{tyre}} = r_{\text{chiral}}$  and the same occurred for the height  $B_{\text{tyre}}$  and the radius  $r_{\text{tyre}}$  which were  $r_{\text{tyre}} = r_{\text{chiral}}$  and  $B_{\text{tyre}} = B_{\text{chiral}}$ . The added rigidity was obtained as a result of considering a different material for the tyre such that the Young's modulus of the two parts verify the condition  $E_{\text{tyre}} \gg E_{\text{chiral}}$ . Once, the connection was completed, the resulting merged part looked as shown in Figure 3.14.

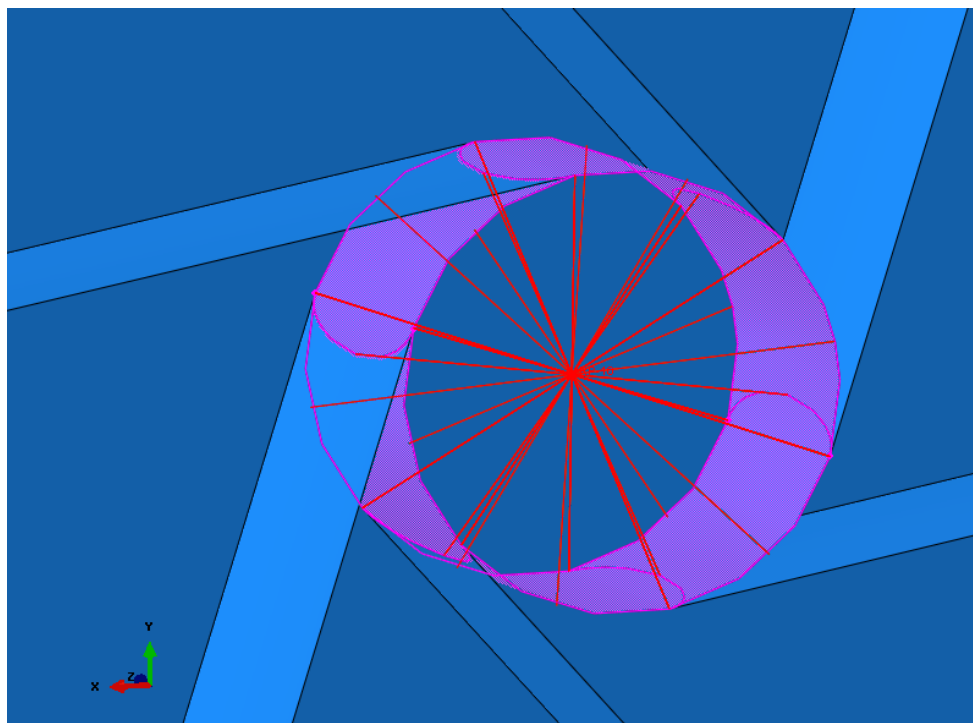


Figure 3.11: Overview of the elements that are involved in the coupling condition at the lattice nodes. The coupling condition was defined in between the mesh nodes located in the faces of the lattice node and a reference point located in the middle. All the degrees of freedom were linked except from the translation displacements in the plane where the chiral lattice is contained, i.e. the translational displacement  $U_1$  and  $U_2$  of the plane  $X - Y$ .

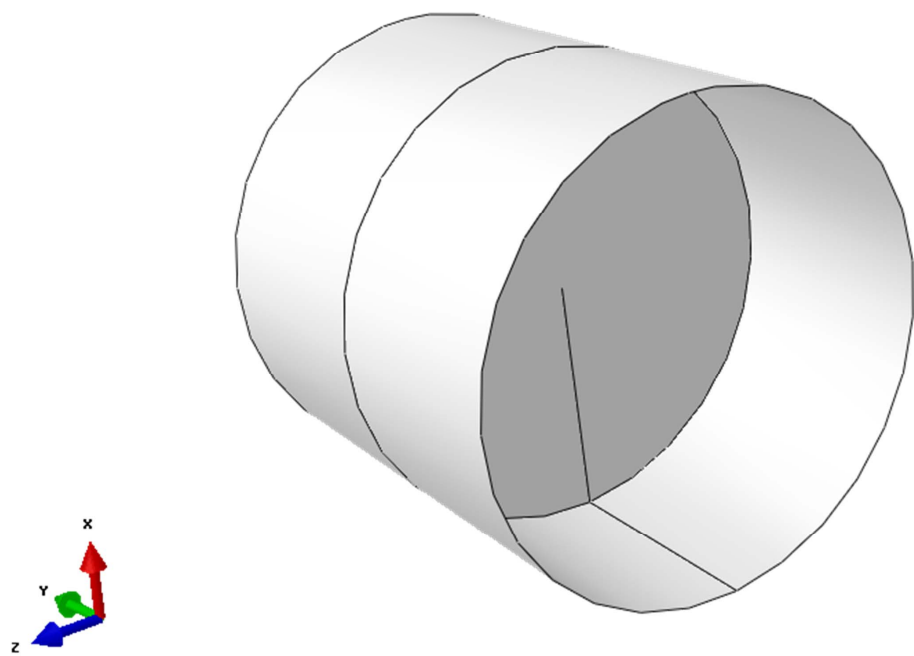


Figure 3.12: Overview of the tyre part.

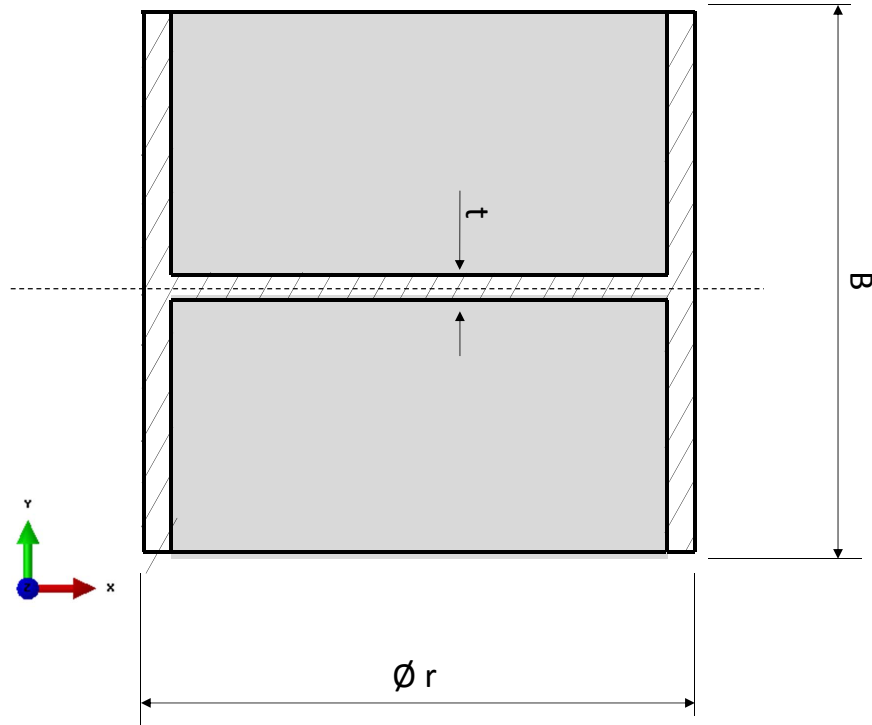


Figure 3.13: Internal parameters of the tyre part. The sketch shows a transversal cut to the part. The tyre is characterized by the radius  $r_{\text{tyre}}$ , the height  $B_{\text{tyre}}$  and the thickness  $t_{\text{tyre}}$ . All this parameters were equal to the corresponding ones in the lattice nodes, therefore:  $r_{\text{tyre}} = r_{\text{chiral}}$ ,  $B_{\text{tyre}} = B_{\text{chiral}}$  and  $t_{\text{tyre}} = t_{\text{chiral}}$ .

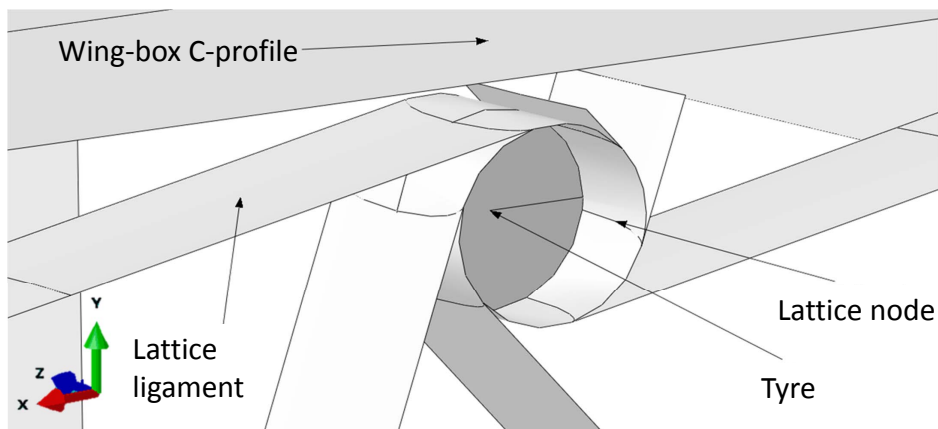


Figure 3.14: Overview of the connection between tyre and lattice node. The tyre will be embed inside the lattice node.

### Wing-box in C-profile

The model of the wing-box consisted on a beam with open C profile. The length  $L_{\text{box}}$  and height  $H_{\text{box}}$  of the part were determined from those of the lattice of chiral elements. Therefore, the tailorable parameters for this part are the width  $W_{\text{box}}$ , the thickness  $t_{\text{box}}$  and the mechanical properties  $E_{\text{box}}$  and  $\nu_{\text{box}}$  of the material used. The value of the Wing-box height  $H_{\text{box}}$  and the wing-box length  $L_{\text{box}}$  are not independent but are calculated based on the transversal and longitudinal dimensions of the chiral lattice structure, respectively.

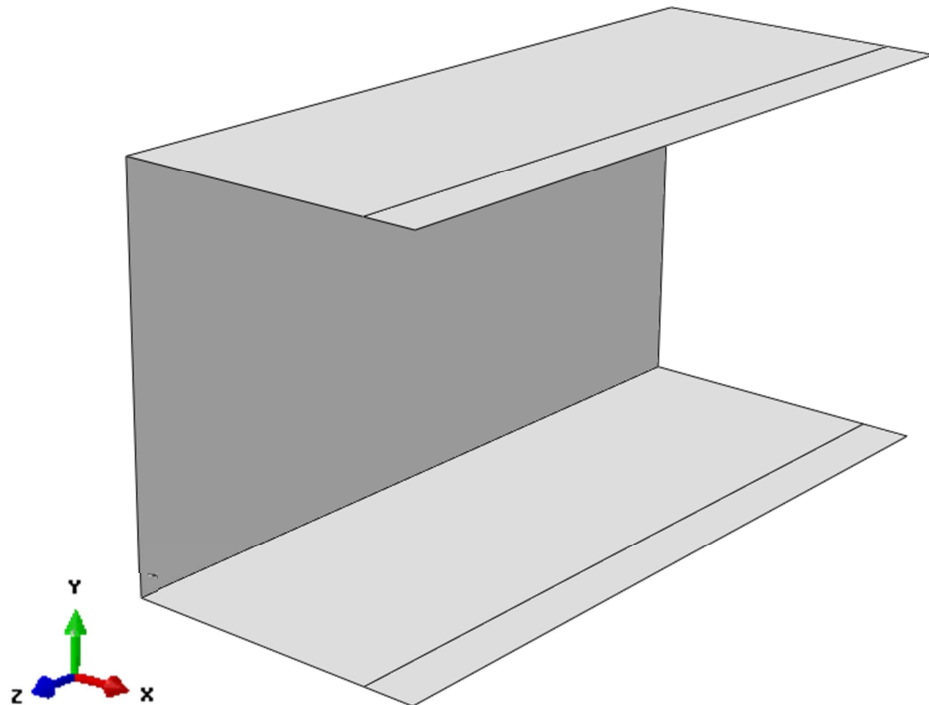


Figure 3.15: Overview of the wing-box in C-profile part

In the sketch shown in Figure 3.16 it is possible see the geometrical meaning of the parameters introduced in the previous paragraph. Additionally, the Table 3.2 shows its units and nominal values.

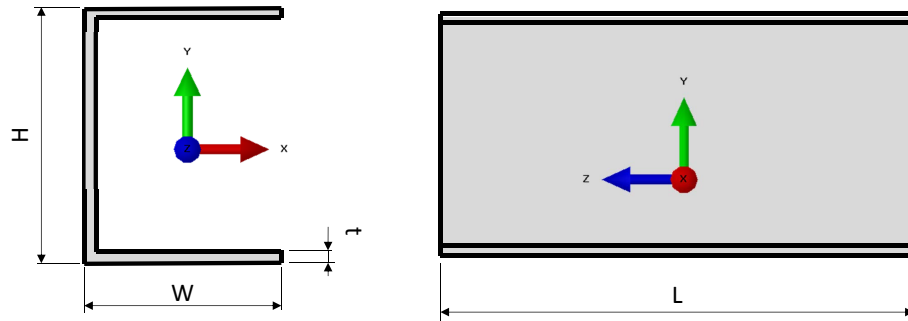


Figure 3.16: Internal parameters of the wing-box C-profile part. The geometry of the part is determined by the length  $L_{\text{box}}$ , height  $H_{\text{box}}$  and the width  $W_{\text{box}}$ . Additionally, the thickness  $t_{\text{box}}$  is measured in the  $z$  direction.

Parameter	Symbol	Units	Nominal value
<b>Dimensions</b>			
Wing-box height	$H_{\text{box}}$	mm	383.27
Wing-box length	$L_{\text{box}}$	mm	743.86
Wing-box width	$W_{\text{box}}$	mm	300
Wing-box thickness	$t_{\text{box}}$	mm	0.8
<b>Material (Aluminum)</b>			
Young's modulus	$E_{\text{box}}$	N/mm <sup>2</sup>	69000
Poisson's ratio	$\nu_{\text{box}}$		0.3269

Table 3.2: Parameters used for the wing-box in C-profile model. The mechanical properties of the material used correspond to standard aluminum. The value of the wing-box height  $H_{\text{box}}$  and the wing-box length  $L_{\text{box}}$  are not independent but are calculated based on the transversal and longitudinal dimensions of the chiral lattice structure, respectively.

## Ribs

As it was shown in Figure 3.4, there are two possible ribs that can be added to the model assembly.  will add rigidity to the wing-box. The ribs located at the tip and at the root will have a closed section, similar to a frame with width  $A_{\text{rib}}$   The width  $W_{\text{rib},\text{close}}$  and the height  $H_{\text{rib}}$  will be equal to the wing-box width  $W_{\text{box}}$  and to the chiral lattice structure height, respectively. The thickness will be  $t_{\text{rib}}$  

The inner ribs will present an open section with same height  $H_{\text{rib}}$  and thickness  $t_{\text{rib}}$  as the closed configuration but different width  $W_{\text{rib},\text{open}}$ . The value of  $W_{\text{rib},\text{open}}$  is calculated as follows:

$$W_{\text{rib},\text{open}} = B_{\text{chiral}} + W_{\text{rib},\text{close}} + d_{\text{chiral-rib}}$$

where  $d_{\text{chiral-rib}}$  represents the gap between the right edges of the inner rib and the lattice chiral structure. This gap ensures that there are not any interferences in between the rib and the lattice chiral structure. The value of this parameter was set to  $d_{\text{chiral-rib}} = 20\text{mm}$ .

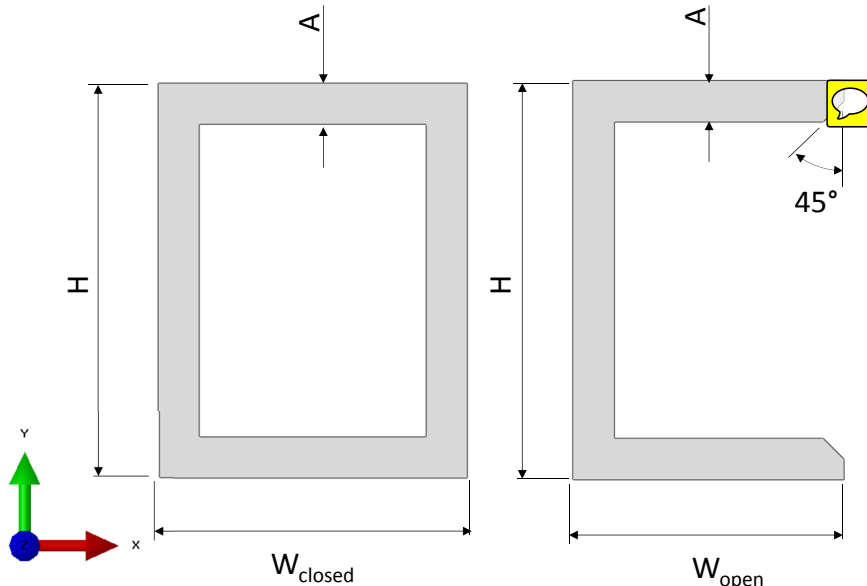


Figure 3.17: Internal parameters of the two different ribs parts.

Therefore, the only tailorable parameters for the ribs configurations are the thickness  $t_{\text{rib}}$  and the frame width  $A_{\text{rib}}$ . The nominal value and units of these two parameters together with the nominal value and units of the remaining dependent parameters can be read in Table 3.3. The Young's modulus was  increased one order of magnitude  comparison of that of the wing-box in order to ensure no out-of-plane deformation of the rib.

Parameter	Symbol	Units	Nominal value
<b>Dimensions</b>			
Rib height	$H_{\text{rib}}$	mm	383.27
Closed rib width	$W_{\text{rib,close}}$	mm	300
Frame width	$A_{\text{rib}}$	mm	30
Rib thickness	$t_{\text{rib}}$	mm	2
<b>Material (Aluminum, 10xE)</b>			
Young's modulus	$E_{\text{rib}}$	N/mm <sup>2</sup>	690000
Poisson's ratio	$\nu_{\text{rib}}$		0.3269

Table 3.3: Parameters used for the ribs model. The Young's modulus was increased one order of magnitude in comparison of that of the wing-box in order to ensure no out-of-plane deformation of the rib. The value of the rib width  $W_{\text{rib,close}}$  and the height  $H_{\text{rib}}$  will be equal to the wing-box width  $W_{\text{box}}$  and to the chiral lattice structure height, respectively.

### 3.4.2 Model mesh

In the present section, the mesh used in the model will be presented. The mesh was unstructured and it was auto-generated by Abaqus CAE for the whole assembly. The elements were a combination of quadratic and tetrahedral with 4 and 3 nodes, respectively. Different mesh elements size were assigned to different parts of the model depending of the stress complexity expected.

In Figure 3.18, it is possible to distinguish two regions that were assigned with different mesh size: the lattice structure and near region of the wing-box skin was assigned with a fine mesh size while the remaining model was assigned with a course mesh, typically one order of magnitude greater. This introduces two new parameters that are used to modify the mesh size of the different regions:

- $S_f$ : Fine mesh size
- $S_c$ : Course mesh size

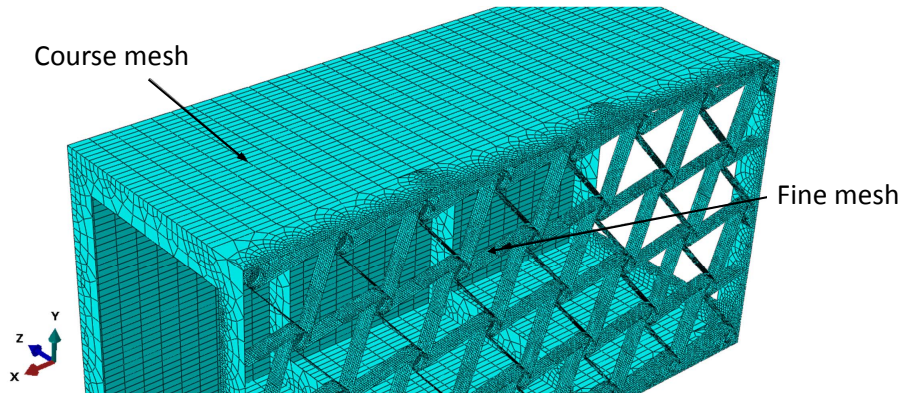


Figure 3.18: Internal parameters of the two different ribs parts. Different mesh elements size were assigned to different parts of the model. The lattice structure was assigned with a fine mesh element size while the wing-box was assigned with a course mesh element size.

### 3.4.3 Attachment points modeling

In the present subsection, the FEM modeling of the connection between the lattice nodes and the wing box is presented. This is an unavoidable transition from the lattice structure of nodes and ligaments to the skin of the wing box. Loads are transmitted to the lattice through this attachment points that is why its design results crucial.

There will be three different configurations that were studied:

**Blocked translation and rotation** The lattice nodes have all its degrees of freedom restrained

**Blocked translation and free rotation** The lattice nodes are free to rotate around its own axis but the translation the direction parallel to the skin is restrained. An sketch showing this connection can be viewed in Figure 3.20. This configuration was the one chosen for the demonstrator built in the Figure 3.19.

**Free translation and rotation** Now the lattice nodes is allowed to translate parallel to the skin. This configuration is schematically represented in Figure 3.21.



Figure 3.19: Detail of the connection between the lattice nodes and the skin. The picture shows the type of connection chosen for the manufactured demonstrator of the lattice. The lattice nodes is allowed to rotate around its own axis but cannot translate parallel to the skin  [1]

In the FEM model, the three connections where modeled using different approaches. Since the lattice of chiral elements and the skin of the wing box were not physical connected by any element, it was necessary to use of the interaction modules provided by Abaqus CAE. There a different options available to constrain the degrees of freedom of a particular set of mesh nodes to another set of mesh

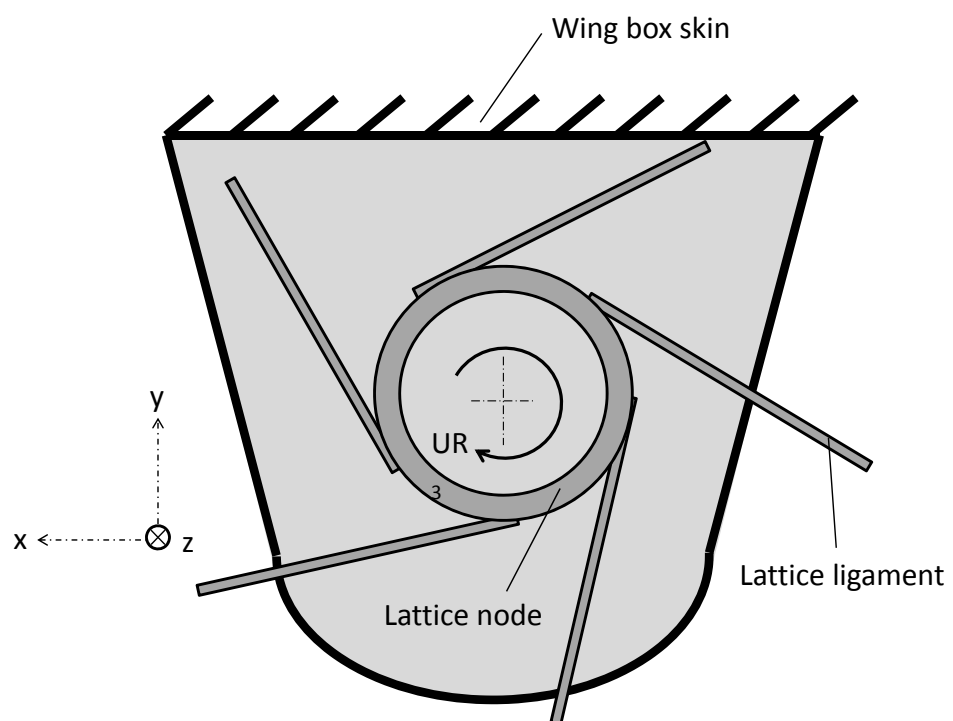


Figure 3.20: Blocked translation and free rotation connection between the lattice nodes and the skin. In this case, the only degree of freedom of the lattice node that it is not restrained the rotation around its own axis, that is the rotation  $UR_3$  around the direction  $z$ .

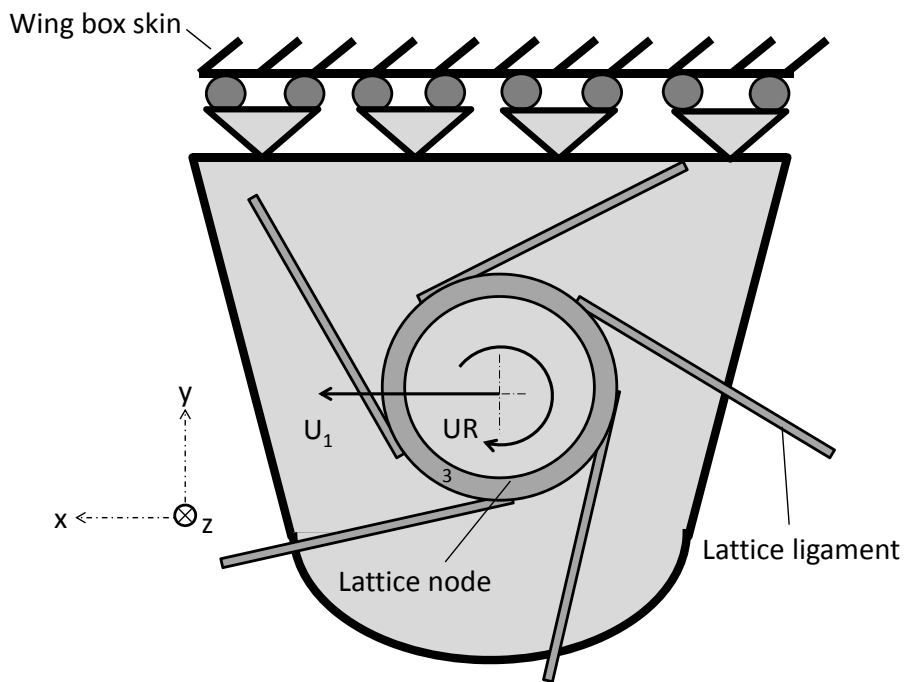


Figure 3.21: Free translation and rotation connection between the lattice nodes and the skin. For this case, the unrestrained degrees of freedom of the lattice nodes are the rotation the rotation  $UR_3$  around its own axis, i.e.: the direction  $z$ ; and the displacement  $U_1$  parallel to the wing-box wall, i.e.: along the direction  $x$ .

nodes. Some of these modules were already explored in Subsection 3.4.1 when investigating how to model the lattice nodes rigid body behavior.

### Coupling through tyre part

This approach consisted in using the tyre part that was described in Subsection 3.4.1. In each of the lattice nodes located at the border of the lattice structure, a tyre part was created and embed into the lattice node, as it was shown in Figure 3.14. Then, a coupling constraint is establish between a mesh node in the middle of the tyre and a mesh node located on the wing-box skin just above the tyre, as shown in Figure 3.22.

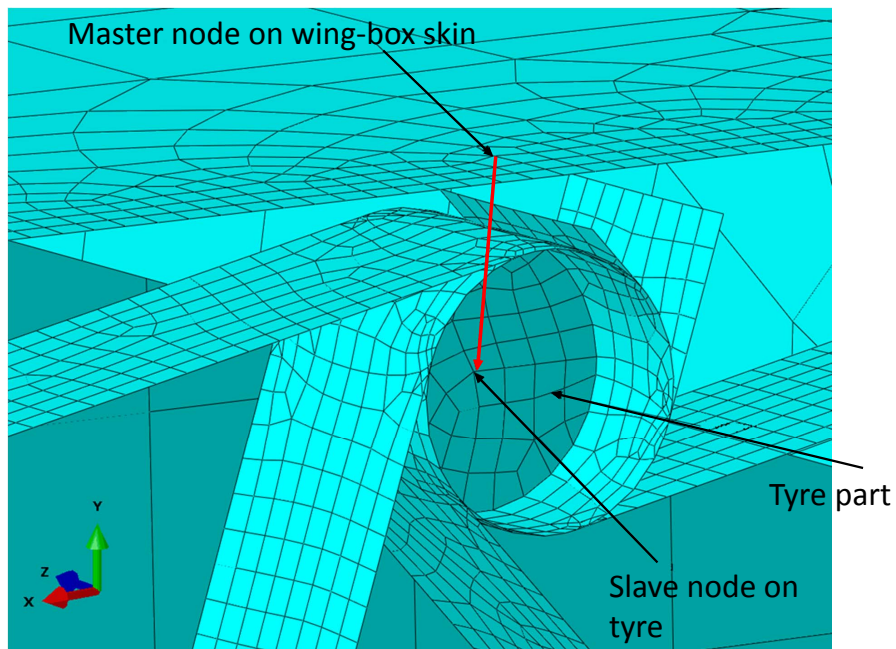


Figure 3.22: Coupling condition between the lattice node and the wing-box skin through tyre. The coupling condition is establish between a mesh node located in the wing-box skin that acts as a master node and a mesh node in the middle of the tyre that becomes the coupling node.

Depending on the type of connection considered, there will be different degrees of freedom the ones that are coupled. For the most restrictive case, in which the connection between the lattice structure and the wing-box is rigid, not allowing any displacement, the six degrees of freedom will be coupled between the mesh nodes mentioned on the previous paragraph.

For the other connection types, rotation of the lattice node is allowed around its own axis. This allowance is implemented by not constraining the rotation  $UR_3$  around the  $z$  direction in the coupling constraint definition. Finally, the last connection type explained at the beginning of the present subsection

allowed the displacement of the lattice node parallel to the wing-box skin. For this case, the translation  $U_1$  along the  $x$  direction is left uncoupled.

The rigid body motion imposed to the mesh node located at the center of the tyre is translated to the mesh nodes located in the faces of the lattice node because they are physically connected.

### Coupling through local cylindrical reference system

In this case, the rigid body characteristic provided by the tyre installation is substituted by an additional coupling condition that is established in a local cylindrical reference system located at each of the lattice nodes. This new reference system substitutes the global Cartesian coordinates system and its origin is a reference point located in the centre of the lattice node, at  $z = B/2\text{mm}$ . The position of a point in the lattice node face will be determined by the radial distance  $r$  to the origin, the angular position  $\theta$  and the position  $z$  along the node rotation axis. A sketch of this reference system is shown in Figure 3.23. In order to ensure the

In the mentioned local reference system, a kinematic coupling constraint links the rigid body motion of the radial position  $r$  and the position  $z$  of a reference point to those of a set of mesh nodes located on the lattice node faces. In the coupling definition, the reference point is the master node and the mesh nodes found in the faces of the lattice node are the slave nodes. This condition is visualized in Abaqus as shown in Figure 3.24.

Then, an additional coupling constraint is necessary to be established between the reference node that acts as the origin of the local cylindrical reference system and the wing-box skin. This is the same one that was previously established when using a tyre part and shown in Figure 3.22. The only difference is that for this case the slave node is the reference point instead of a mesh node located in the center of the tyre.

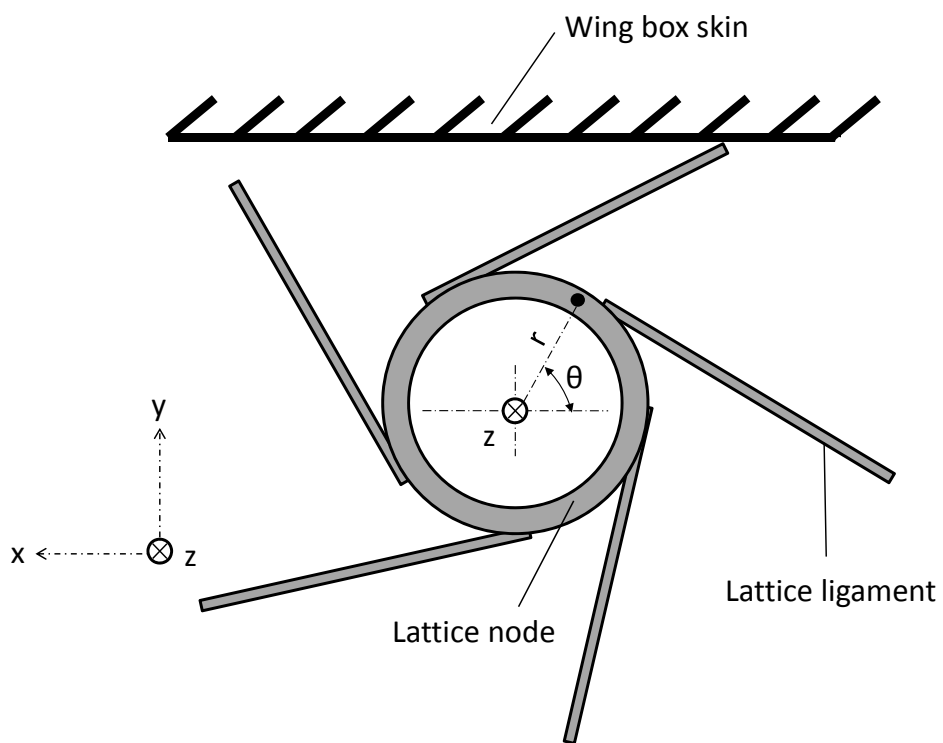


Figure 3.23: Local reference system at the lattice nodes. The position of point in the lattice node faces will be determined by the radial distance  $r$  to the origin, the angular position  $\theta$  and the position  $z$  along the node rotation axis.

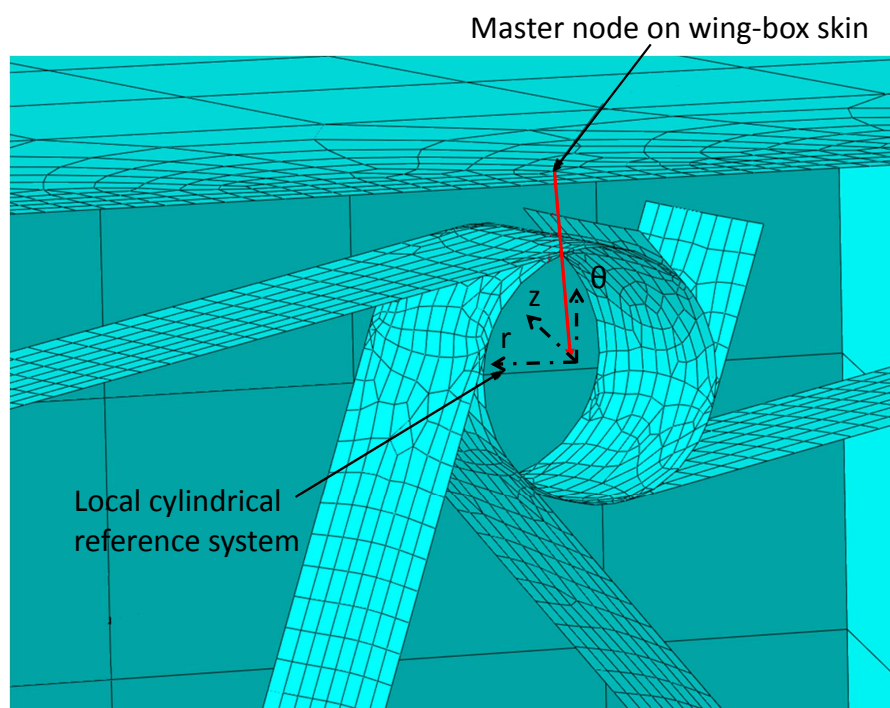


Figure 3.24: Coupling condition between the lattice node and the wing-box skin through a local reference system.

### 3.4.4 Parametric study method

The model was described in the previous subsections was implemented in a Python program that was read by the FEM software, Abaqus. This enables the possibility of executing different simulations for different values of the parameters introduced previously. An schematic characterization of the program execution is shown the flow chart represented in Figure 3.25.

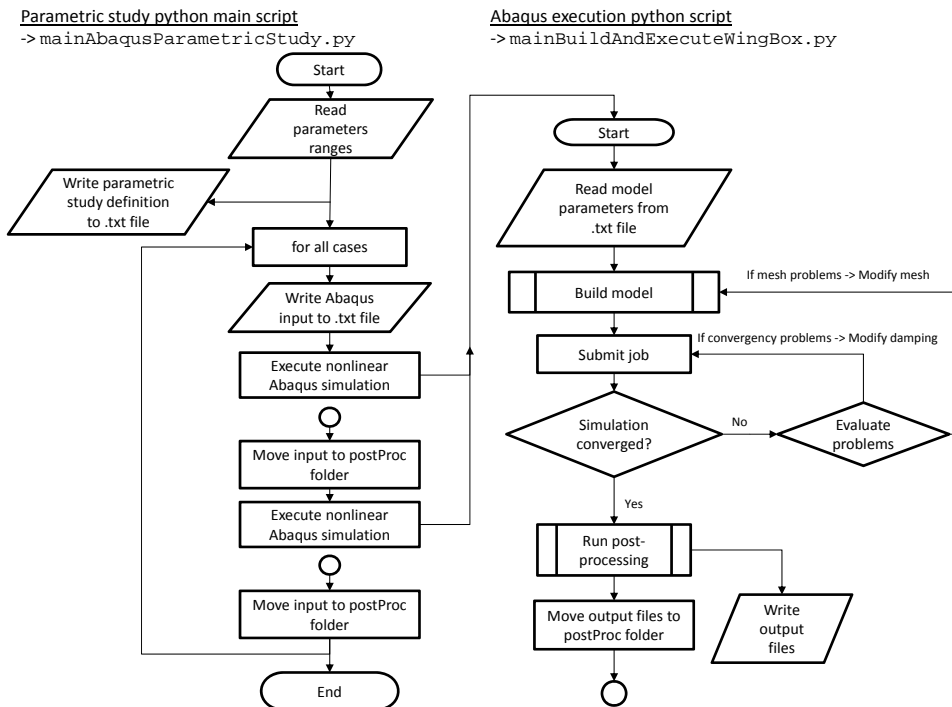


Figure 3.25: Flow chart showing the execution of the parametric study code.

# Chapter 4

## Model analysis

### 4.1 Introduction

### 4.2 Parametric study on the analytical model

In the present subsection, the variation of the beam properties for different parameter values will be shown. The beam geometry will be characterized through the cross-sectional aspect ratio  $B/H$ , the thickness ratio  $t_2/t_1$  and the slenderness ratio  $L/B$ . The effect of these parameters on the sectional properties, twist and bending stiffness, and flexural and twisting compliance will be shown. Additionally, the variance of the stiffness ratio  $E_1/E_2$  will also be included in the analysis.

#### 4.2.1 Results

The influence of the cross-sectional aspect ratio  $B/H$  on the torsional stiffness  $GI_t$ , the shear centre position  $y_{SC}$  and the flexural stiffness  $EI_y$  is shown in Figures 4.1, 4.2 and 4.3, respectively. On its side, the effect of thickness ratio  $t_2/t_1$  on the same three beam parameters is shown in Figures 4.6, 4.7 and 4.8.

Additionally, the effect of the cross-sectional aspect ratio  $B/H$  on the deflection and torsional compliance is shown on Figures 4.4 and 4.5, respectively. The corresponding plots when analysing the effect of the thickness ratio  $t_2/t_1$  on the deflection and torsional compliance are shown on Figures 4.9 and 4.10, respectively. The beam's torsional compliance will be expressed as fraction of the twist at the tip divided by the vertical force applied, that is  $|\phi_{tip}|/Q$ , while the beam deflection compliance will be expressed as fraction of the maximum vertical displacement at the tip divided by the vertical force applied, that is  $w_{0,tip}/Q$ .

The effect of the slenderness ratio  $L/B$  on the deflection and torsional compliances is shown in

Figures 4.11 and 4.12, respectively.

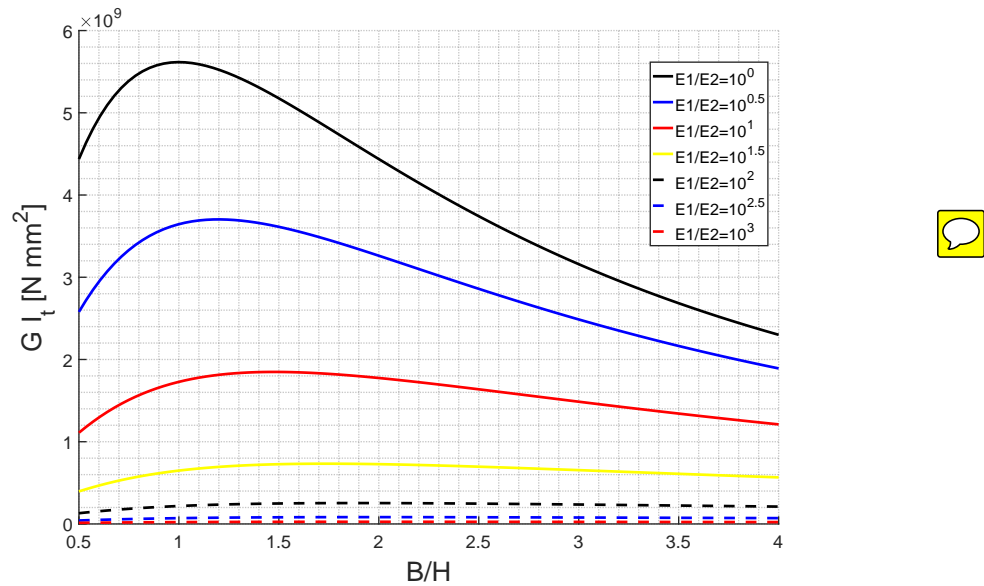


Figure 4.1: Influence of the cross-sectional aspect ratio  $B/H$  on the torsional stiffness  $GI_t$  is shown for various values of the stiffness ratio  $E_1/E_2$  ranging from  $10^0$  to  $10^3$ .

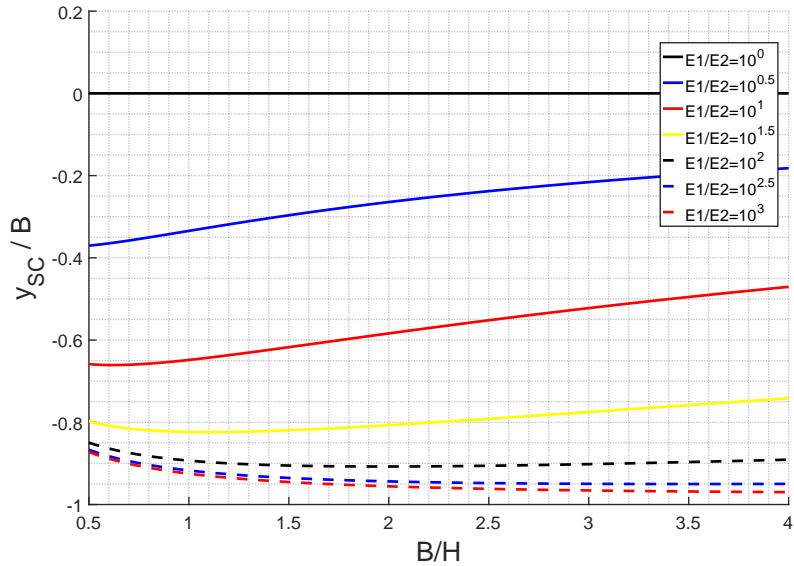


Figure 4.2: Influence of the cross-sectional aspect ratio  $B/H$  on the dimensionless shear centre position  $y_{SC}/B$  is shown for various values of the stiffness ratio  $E_1/E_2$  ranging from  $10^0$  to  $10^3$ .

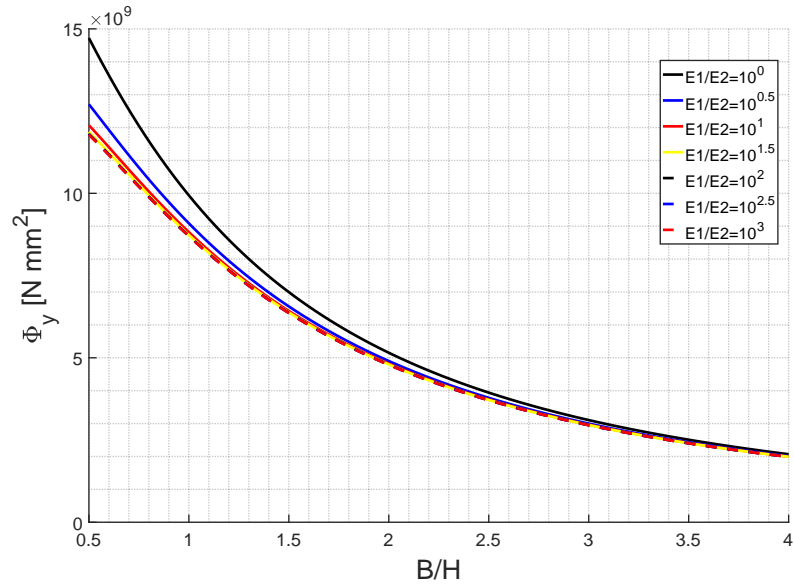


Figure 4.3: Influence of the cross-sectional aspect ratio  $B/H$  on the flexural stiffness  $EI_y = \Phi_y$  is shown for various values of the stiffness ratio  $E_1/E_2$  ranging from  $10^0$  to  $10^3$ .

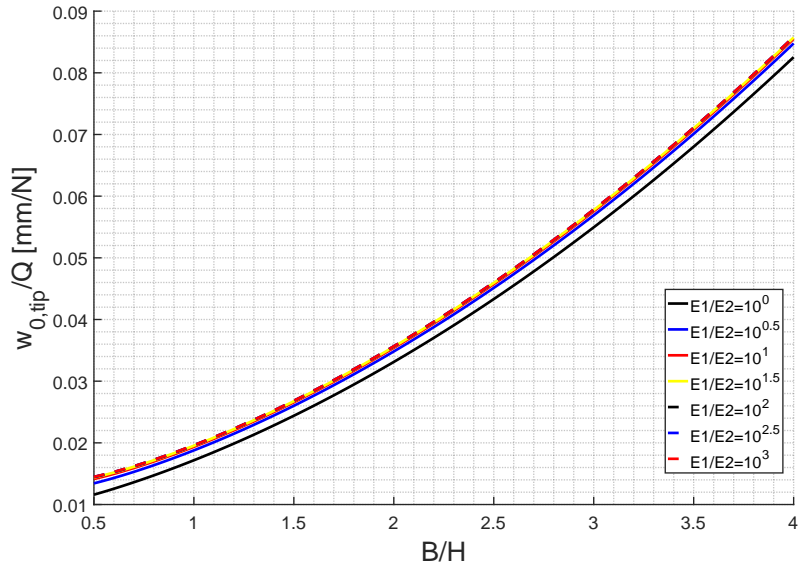


Figure 4.4: Influence of the cross-sectional aspect ratio  $B/H$  on the deflection compliance  $w_{0,tip}/Q$  is shown for various values of the stiffness ratio  $E_1/E_2$  ranging from  $10^0$  to  $10^3$ .

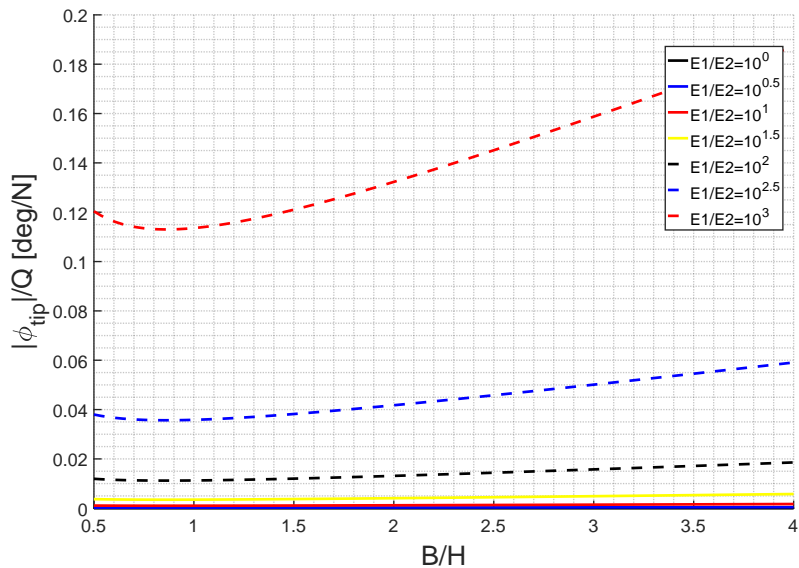


Figure 4.5: Influence of the cross-sectional aspect ratio  $B/H$  on the torsional compliance  $|\phi_{tip}|/Q$  is shown for various values of the stiffness ratio  $E_1/E_2$  ranging from  $10^0$  to  $10^3$ .

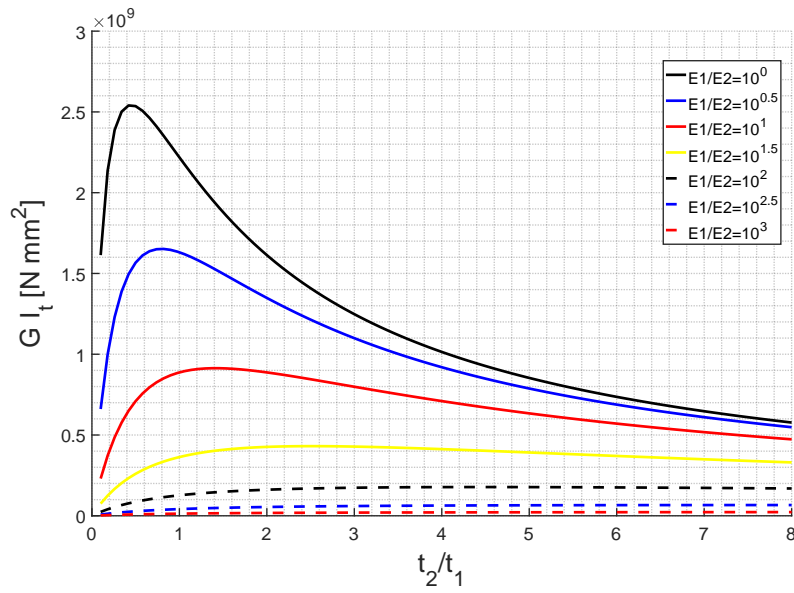


Figure 4.6: Influence of the wall thickness ratio  $t_2/t_1$  on the torsional stiffness  $GI_t$  shown for various values of the stiffness ratio  $E_1/E_2$  ranging from  $10^0$  to  $10^3$ .

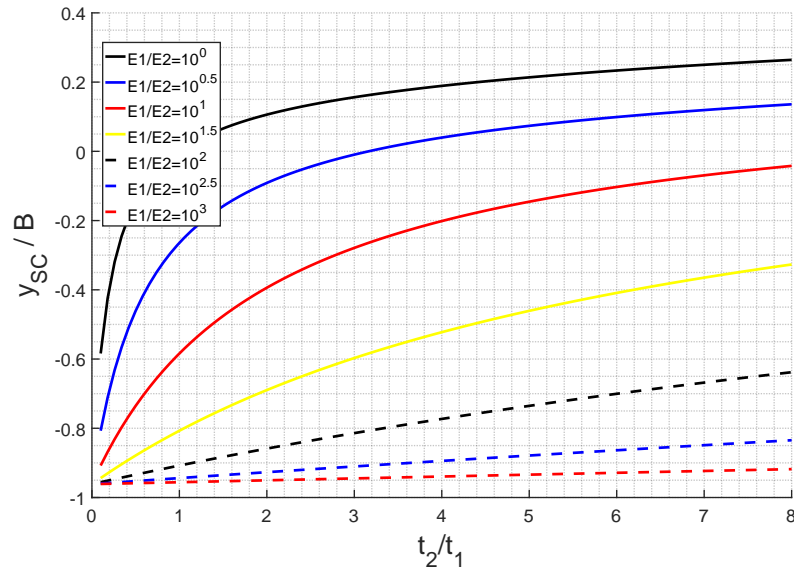


Figure 4.7: Influence of the wall thickness ratio  $t_2/t_1$  on the dimensionless shear centre position  $ysc/B$  shown for various values of the stiffness ratio  $E_1/E_2$  ranging from  $10^0$  to  $10^3$ .

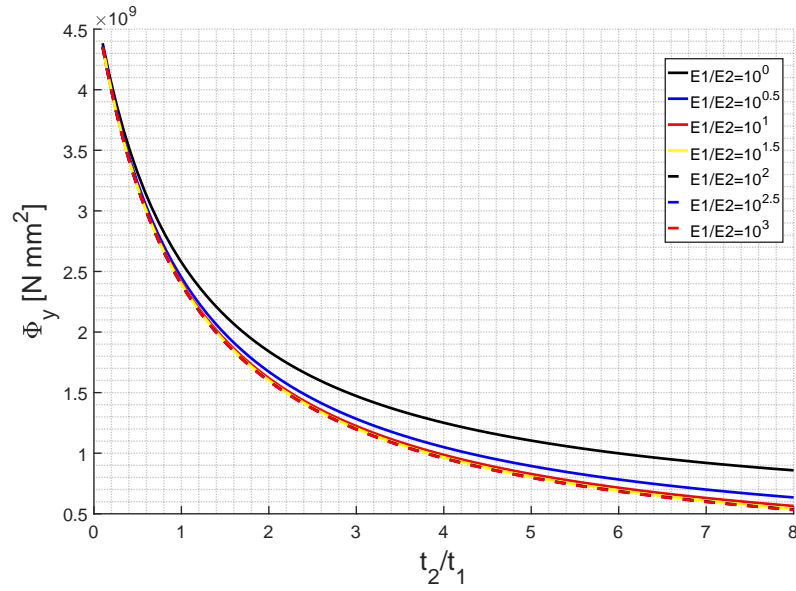


Figure 4.8: Influence of the wall thickness ratio  $t_2/t_1$  on the flexural stiffness  $EI_y = \Phi_y$  shown for various values of the stiffness ratio  $E_1/E_2$  ranging from  $10^0$  to  $10^3$ .

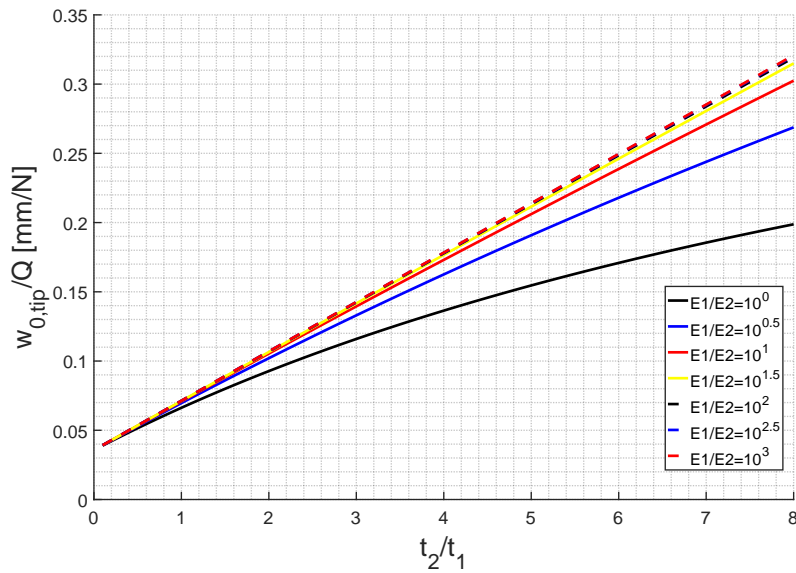


Figure 4.9: Influence of the thickness ratio  $t_2/t_1$  on the deflection compliance  $w_{0,tip}/Q$  is shown for various values of the stiffness ratio  $E_1/E_2$  ranging from  $10^0$  to  $10^3$ .

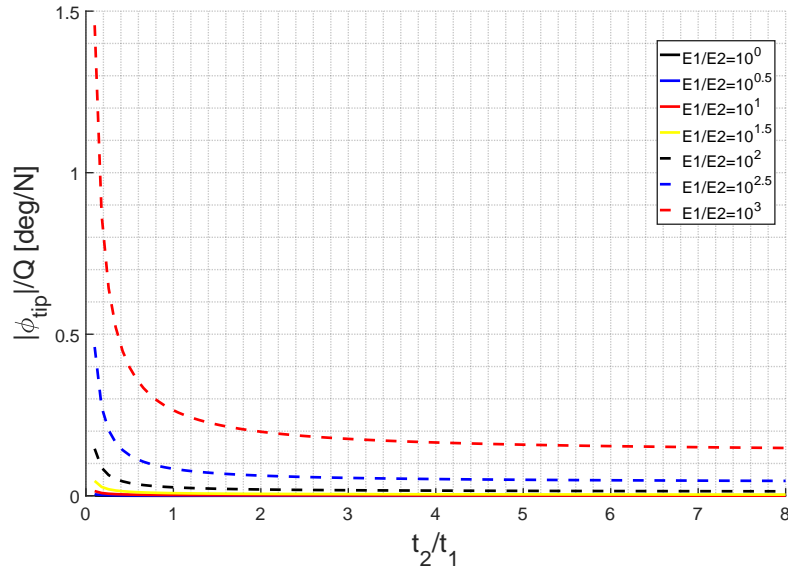


Figure 4.10: Influence of the thickness ratio  $t_2/t_1$  on the torsional compliance  $|\phi_{\text{tip}}|/Q$  is shown for various values of the stiffness ratio  $E_1/E_2$  ranging from  $10^0$  to  $10^3$ .

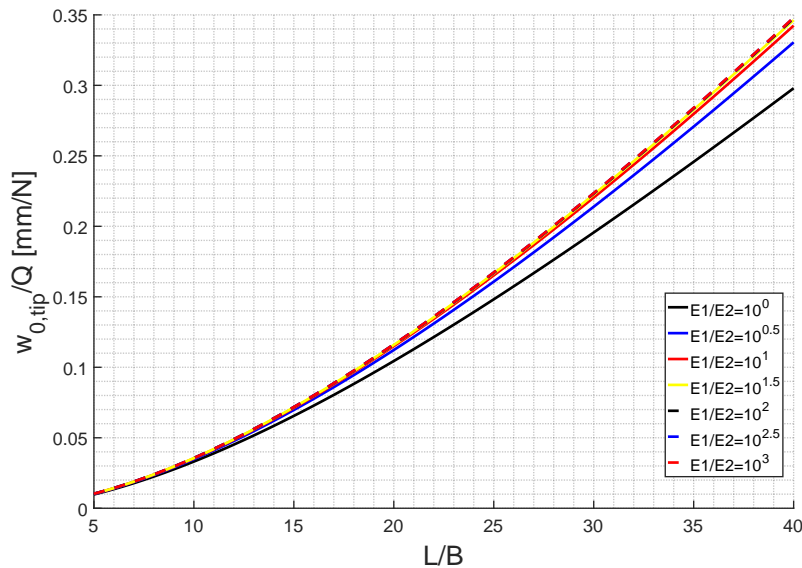


Figure 4.11: Influence of the slenderness ratio  $L/B$  on the deflection compliance  $w_{0,\text{tip}}/Q$  is shown for various values of the stiffness ratio  $E_1/E_2$  ranging from  $10^0$  to  $10^3$ .

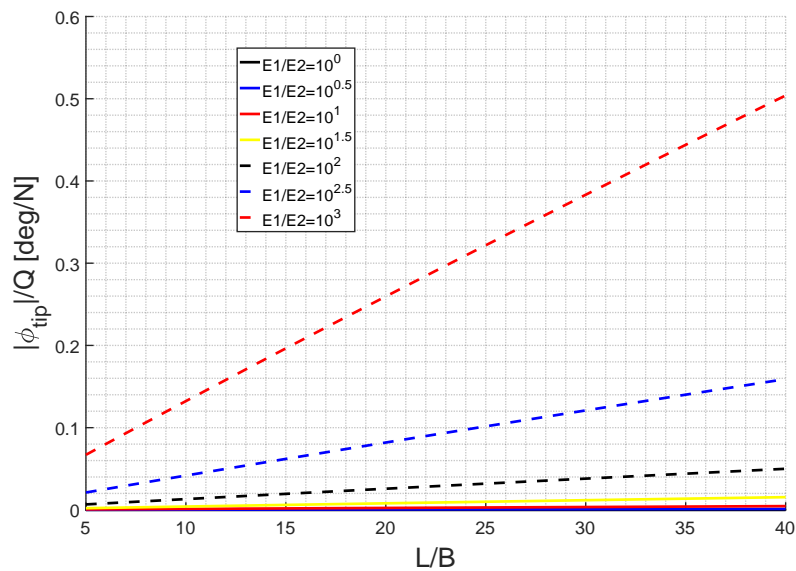


Figure 4.12: Influence of the slenderness ratio  $L/B$  on the torsional compliance  $|\phi_{\text{tip}}|/Q$  is shown for various values of the stiffness ratio  $E_1/E_2$  ranging from  $10^0$  to  $10^3$ .

### 4.2.2 Discussion of the results

The maximum torsional stiffness  $GI_t$  as a function on the cross-sectional aspect ratio  $B/H$  can be visualized in Figure 4.1. It can be seen that it appears for  $B/H = 1$  when  $E_1/E_2 = 1$ . Therefore, as it is also shown in [23], the closer the torsional stiffness to the doubly symmetric case, the higher its torsional stiffness. However, when  $E_1/E_2 > 10$ , the maximum torsional stiffness is shown to appear for  $B/H > 1$ . A similar conclusion can be extract when analysing the Figure 4.6, that shows the influence of the thickness ratio  $t_2/t_1$  on the torsional stiffness  $GI_t$ .

In Figure 4.2 it can be seen that for values  $E_2 \ll E_1$ , the shear centre position  $y_{SC}$  is approximately constant for  $B/H$  variations. In this context, the beam approximates its behavior as if it has an open profile section. However, as the value of  $E_1/E_2$  decreases, the influence of the ratio  $B/H$  increases showing a bigger influence of the web where the Young's modulus  $E_2$  applies. On the other hand, Figure 4.7 shows that the bigger the thickness ratio  $t_2/t_1$  is, the closer that the shear centre  $y_{SC}$  will be to the vertical axis of simmetry. However, for  $E_2 \ll E_1$  the influence of the thickness ratio  $t_2/t_1$  is reduced.

The influence of the cross-sectional aspect ratio  $B/H$  and the tickness ratio  $t_2/t_1$  on the flexural stiffness  $EI_y$  is shown to be bigger than that of the Young's modulus ratio  $E_1/E_2$ , as shown on Figures 4.3 and 4.8, respectively.

## 4.3 Computational model analysis

### 4.3.1 Connection between the chiral lattice and the wing-box skin

### 4.3.2 Mesh

The model was build using cell shell elements as the fundamental constituting part. The thickness is assigned in the perpendicular direction, as it was shown in Figure 3.5.

This type of element is a 2D element that it was used to build 3D structures. This kind of procedure may incur some distortion in the mesh elements due to shell elements intersecting in the same line at different angles.

For the designed model, this situation occurred at the chiral lattice at certain points. It can be seen in Figure 4.13 that the distorted elements appear at mainly at two different positions. Firstly, at the plane where the two ligaments with different curvature join. At this point, the sharp angles that appear in between the part geometrical lines induce the appearance of tetrahedral distorted mesh elements. The second typical location for appearance of distorted elements is along the curve where the lattice nodes and the curved ligaments join.

It was seen that the number of distorted elements had a significant effect in the simulation convergence evolution. For a high number of distorted elements, the simulation could not go further from the

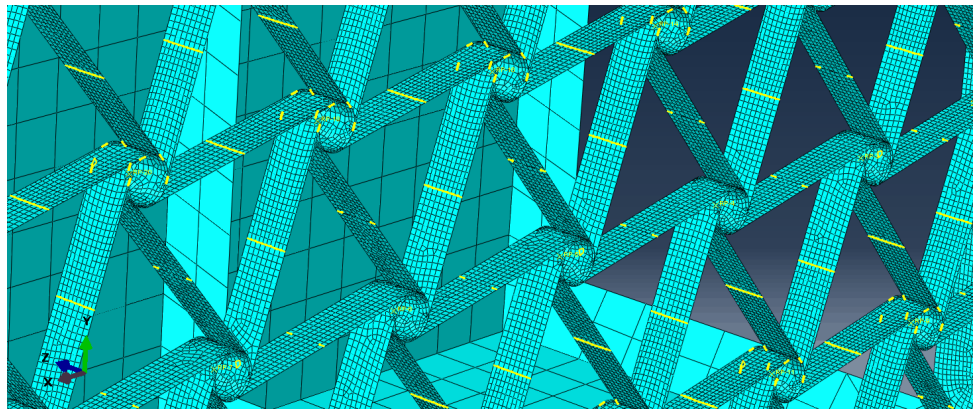


Figure 4.13: Distorted mesh elements in the model. The number of distorted elements was found to be crucial for the simulation convergence.

first step. No attempts to locally modify the mesh at the mentioned locations were made, instead, it was found that modifying the global mesh size gave enough control over the number of distorted elements to be able to overcome this limitation. The bigger the mesh size in the area, the less distorted elements appear after completing the meshing operations.

**4.3.3 Load definition**

#### 4.3.4 Boundary condition

The boundary condition was the one shown in Figure 4.14. It consisted in a kinematic coupling similar to the one introduced in Section 3.4.1 to model the rigid body behavior of the lattice nodes. In this case, the kinematic coupling is established between a reference point located approximately at the centre of the root rib and the faces of this mentioned rib. The reference point acts as a master node while the mesh nodes located at the faces of the rib are the slave nodes. The reference point is next fixed in all its degrees of freedom using the corresponding boundary condition Abaqus module.

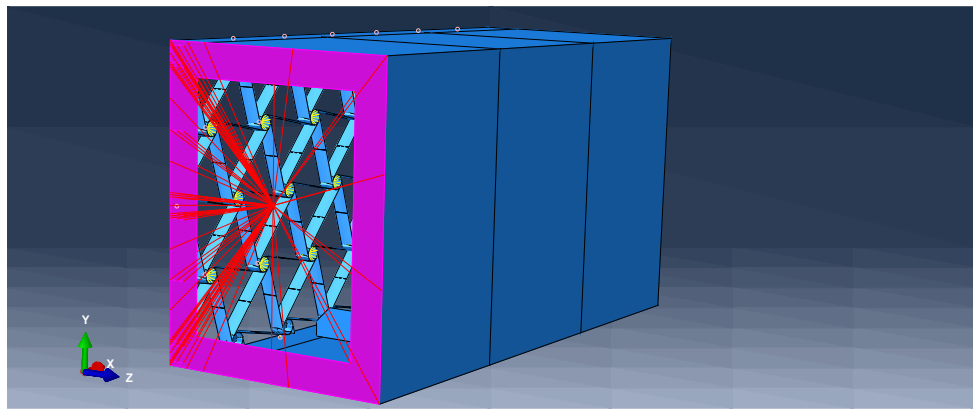


Figure 4.14: Boundary condition for the model. The condition is established through a coupling interaction between a reference point and the faces of the rib at the root. The reference point is fixed in all its degrees of freedom using the corresponding boundary condition Abaqus module.

#### 4.3.5 Results analysis

The results obtained from the Abaqus simulations were analyzed in two different ways. Firstly, qualitatively by means of the deformation plots that shown by the Abaqus. And, secondly, extracting values of different magnitudes directly from the mesh nodes or elements located at certain positions of interest.

Through the definition of paths in Abaqus, it is possible to obtain the value of a determined magnitude for all the mesh elements located along the path. In Figure 4.15, an example of a path located on the upper skin of the wing-box is shown.

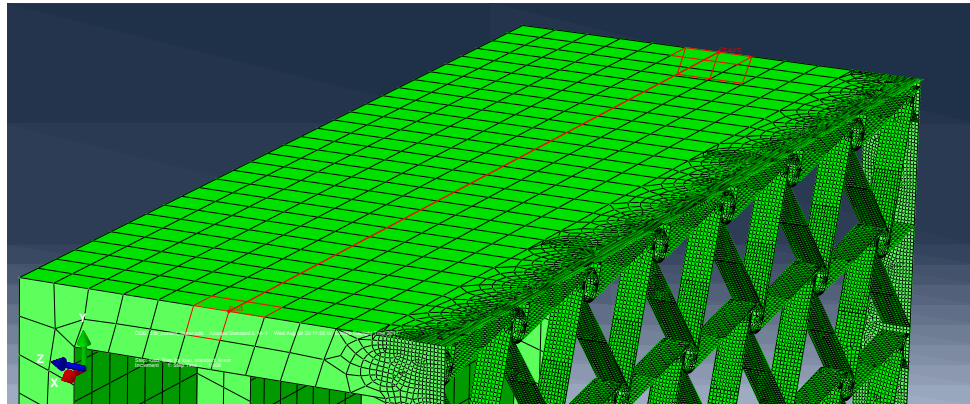


Figure 4.15: Path of mesh elements on the solution model.

### 4.3.6 Nonlinear problem and automatic stabilization

For the case under study, nonlinear simulations will be carried out as is expected to find a nonlinear load-displacement curve as a result of the analysis. In Abaqus, to execute nonlinear simulation involves the following, as shown in [32]:

- a combination of incremental and iterative procedures;
- using the Newton method to solve the nonlinear equations;
- determining convergence;
- defining loads as a function of time; and
- choosing suitable time increments automatically.

Therefore, Abaqus breaks the step where the load is applied into increments. The software will automatically choose the size of each of the increments based on the convergence evolution of previous increments.

Also, nonlinear static problems may become unstable. One of the possible sources of such instabilities is buckling. A model where buckling appears locally may not be resolvable using general solution methods. For this kind of cases, it becomes necessary to either solve the problem dynamically or with the aid of artificial damping.

Since the above situation represents what it is expected to be found in the model response, a constant artificial damping factor will be used throughout the whole step to account for the appearance of local instabilities.

Automatic stabilization with a constant damping factor implies that viscous forces of the form:

$$F_v = c\mathbf{M}\mathbf{v}$$

are added to the global equilibrium equations:

$$\mathbf{P} - \mathbf{I} - \mathbf{F}_v = 0,$$

where  $\mathbf{I}$  represents the internal forces,  $\mathbf{P}$  the external forces,  $\mathbf{M}$  is the artificial mass matrix calculated with unity density,  $c$  is the defined damping factor,  $\mathbf{v} = \Delta\mathbf{u}/\Delta t$  is the vector of nodal velocities, and  $\Delta t$  is the increment of simulation time.

The final value that is going to be used during the simulations was chosen after performing a small parametric study of the different possibilities. As a result, the plot shown in Figure 4.16 was produced. This plot represents the evolution of the twist at the tip as the load is increased step by step during the nonlinear simulation. As it will be explained in Section 5.2, the use of automatic stabilization becomes

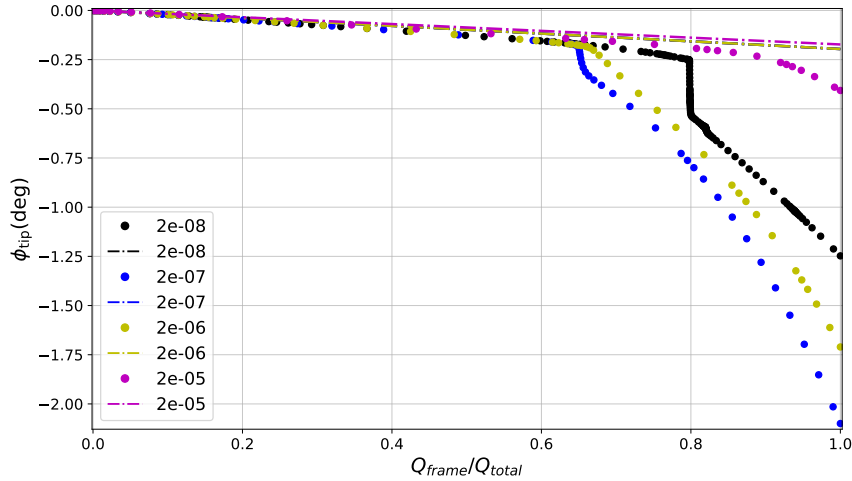


Figure 4.16: Force-displacement curve for various values of constant artificial damping factor.

necessary to capture the dynamics that involve buckling on the chiral ligaments and the ultimate collapse of the structure.

As it can be seen in the mentioned figure, all the different values of the damping factors success to capture the rapidly change in tip twist that occurs for fractions of load applied  $> 60\%$ . However, special care needs to be taken in order not ensure that the inclusion of artificial damping factor is not leading to inaccurate results due to over-damping of the structure. This can be done why comparing the fraction of the static energy that it is dissipated compared to the external work that its put into the system. This is done for a values of  $c = 2 \times 10^{-5}$ ,  $c = 2 \times 10^{-8}$  and  $c = 2 \times 10^{-9}$  in Figures 4.17, 4.18 and 4.19, respectively. In this plots, the moment where the structure collapses due to the buckling phenomena occurring on the chiral ligaments can be seen as a sudden change in the slope of both curves. Here it can be seen that the case of  $c = 2 \times 10^{-5}$ , the slope of the curve showing the energy dissipated through artificial stabilization is positive, which is a sign of over-damping in this region. On the other hand, for the case of  $c = 2 \times 10^{-8}$ , the slope remains of the curve remains zero. Finally, for the case of  $c = 2 \times 10^{-9}$ , the slope also remains zero and the final value for the energy dissipated is smaller than for  $c = 2 \times 10^{-8}$ .

Finally and based on what has been previously explained, it was decided to use damping factor  $c = 2 \times 10^{-9}$  for the simulations perform ahead.

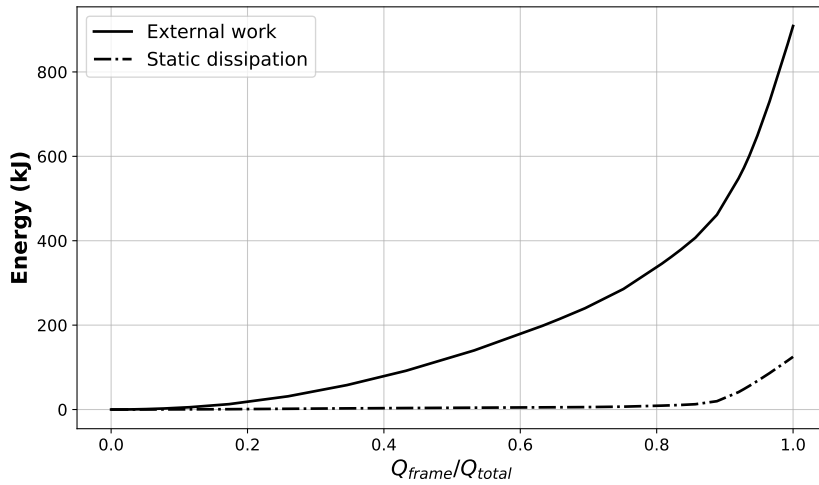


Figure 4.17: External work and static dissipation for a damping factor equal to  $2 \times 10^{-5}$ . The positive slope of the curve showing the energy used in the static dissipation is a sign of over-damping.

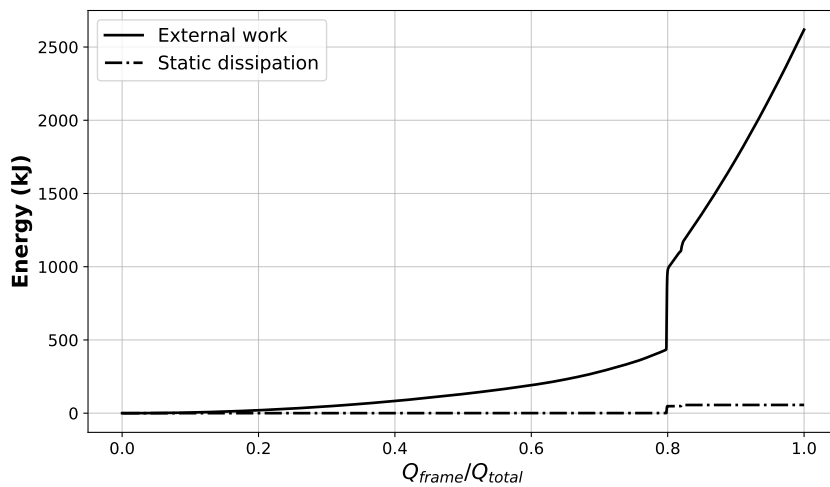


Figure 4.18: External work and static dissipation for a damping factor equal to  $2 \times 10^{-8}$ . After the structure collapse the static dissipation energy remains constant and small compared with the external work introduced into the system.

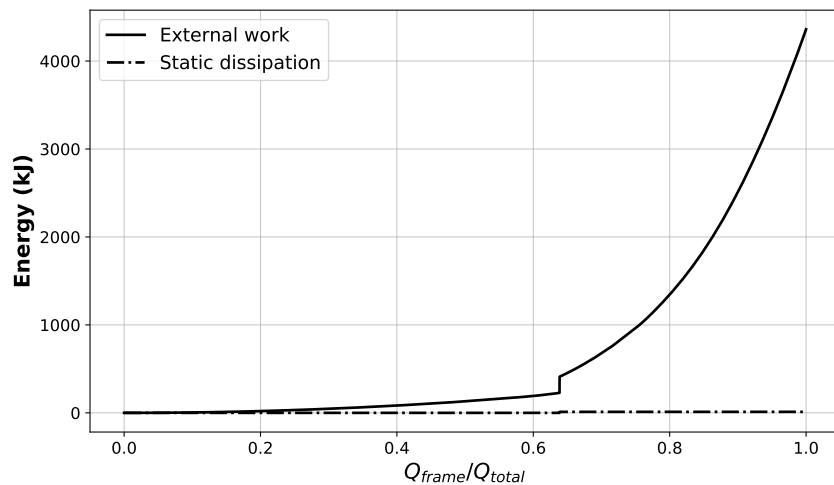


Figure 4.19: External work and static dissipation for a damping factor equal to  $2 \times 10^{-9}$ . After the structure collapse the static dissipation energy remains constant and negligible compared with the external work introduced into the system.

### 4.3.7 Inner ribs

Initially, the model did not incorporate inner ribs and the ribs located at the tip and the root had an open profile. In Figure 4.20, it can be seen an example of the response seen for this type of configuration.

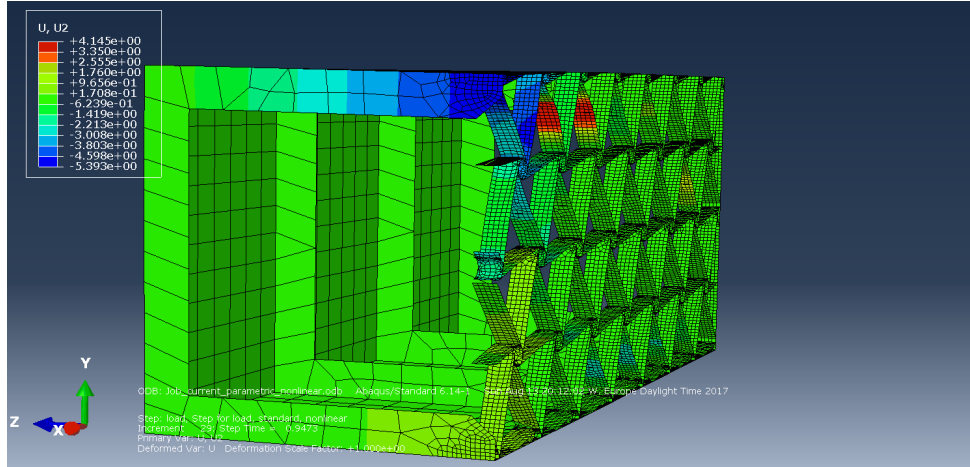


Figure 4.20: Vertical displacement  $v$  at the tip rib. The color contour shows those mesh nodes located on the upper flange of the rib have a higher  $v$ , therefore showing how the rib is closing under the prescribed load (800 N)

For this reason, it was decided to use ribs with a close profile. The simulations then provided a solution like the one shown in Figure 4.21. For this case, the initial buckling occurs in ligaments located far from the root. The twist of the beam, measured as the angular rotation  $UR_1$  around the  $x$  axis is of 0.3 deg. The prescribed load was -800 N and the simulation converged to the 0.95% of the prescribed load.

In order to investigate further deformations of the ligaments, it was decided to carry out simulations that incorporate automation stabilization through artificial damping artificial damping factor, as it was explained in Subsection 4.3.6. After this, the results showed a deformation like the one shown in Figure 4.22. This figure shows how big local deformations appear on the wing-box upper skin for this case. Also, it can be seen that the buckling phenomena has moved backwards to the ligaments close to the root.

In order to reduce the local deformations occurring on the wing-box, a pair of inner ribs as described in Subsection 3.4.1 were added to the model. This element added stiffness to the structure in bending. Now, the response of the model was shown to be like the one represented in Figure 4.23. Here it can be seen that the ligaments that start to buckle are located at the same position as they were in the response of the model that did not incorporate inner ribs seen in Figure 4.21. However, now the degree of deformation has decreased due to the stiffness added to the structure as a result of the inner ribs addition.

However, for this last case, the simulation was only able to converge up to 13% of the prescribed

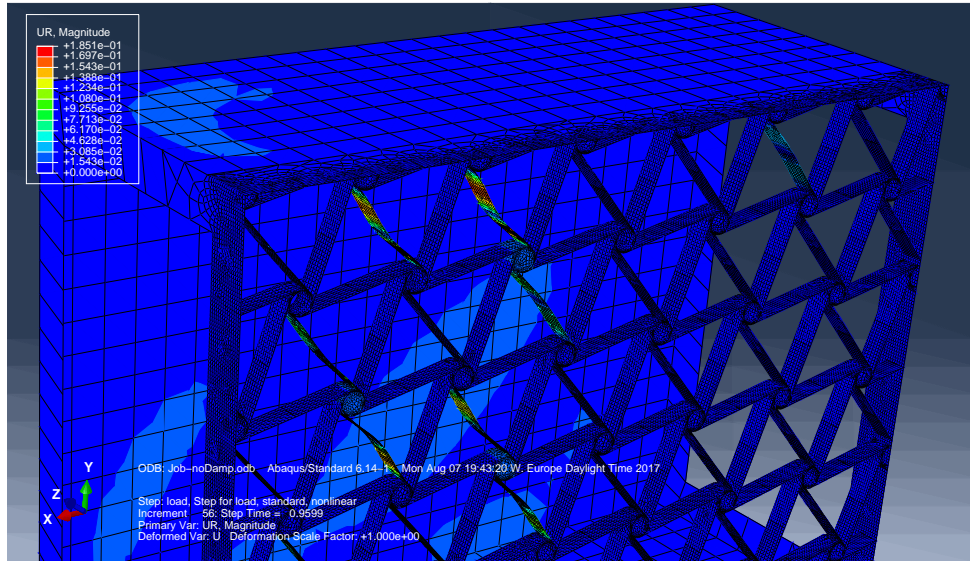


Figure 4.21: Model response without the use of inner ribs nor automatic stabilization.

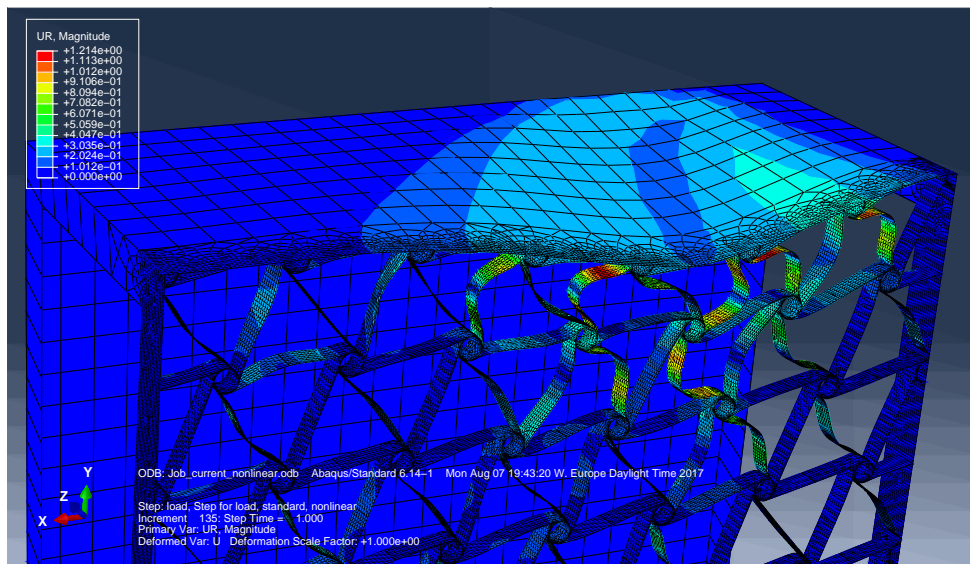


Figure 4.22: Model response without the use of inner ribs with automatic stabilization.

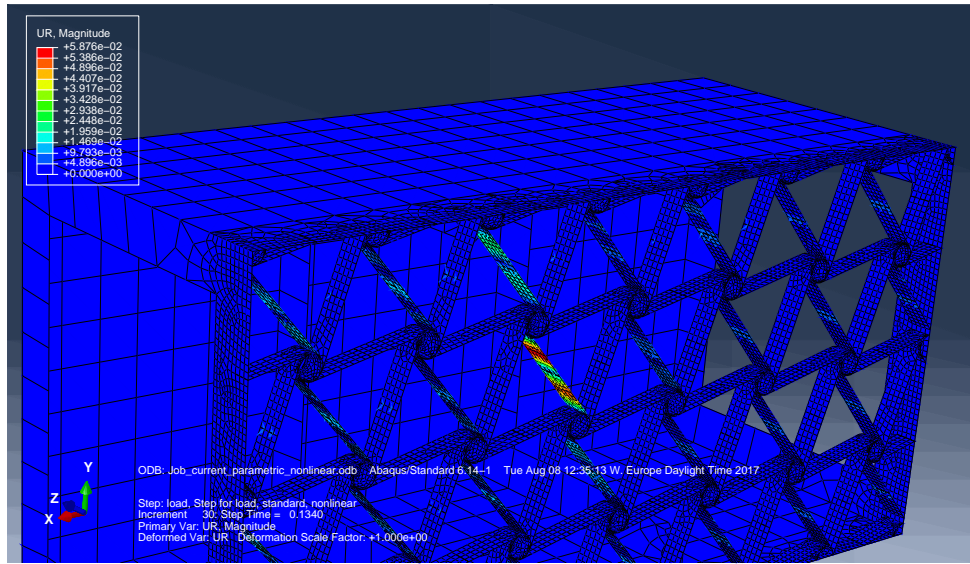


Figure 4.23: Model response incorporating inner ribs and without automatic stabilization

load. In order to progress further in the analysis, the use of automatic stabilization becomes necessary again. For this reason, in the final configuration, automatic stabilization through constant damping factor will be used together with the inner ribs. A description of the response of the structure for this last case is presented on next chapter.

# Chapter 5

## Simulations results

### 5.1 Introduction

### 5.2 General response characterization

In this section, the general response of the model will be characterized. For the wing-box, the nominal value of its characteristic parameters are those shown in Table 3.2, while Tables 3.1 and 3.3 contain the nominal values of the main parameters for the chiral lattice and the ribs, respectively. Also, the baseline configuration will incorporate a pair of inner ribs and the load will be applied on a single mesh node on the upper flange of the tip rib, as described in Subsection 4.3.3.

In the simulations, automatic stabilization artificial through constant damping factor is included. For this case, the response of the structure when 65% of the prescribed load has been applied is the one shown in Figure 5.1. It can be seen that buckling starts and it is more severe in the ligament located just after the inner rib located closer to the root. In a further load increment, buckling phenomena moves backwards and those ligaments located close to the root and at a higher  $y$  coordinate, start to deform even more severely. At this point, the structure collapses and the twist increases for smaller increments in the applied load. This can be seen in Figure 5.2.

This is the point at which the local instabilities are such that there is need of adding artificial damping factor in order to capture this dynamics. After this point, the artificial damping allows the simulation to continue. As it was explained in Subsection 4.3.6, special care needs to be taken in order not ensure that the inclusion of artificial damping factor is not leading to inaccurate results due to over-damping of the structure. This can be done by comparing the fraction of the static energy that it is dissipated compared to the external work that its put into the system. The Figure 5.3 makes this comparison possible. It can be seen that effectively, the static dissipation through automatic stabilization is negligible in comparison with the external work. This figure also shows the abrupt increment in external work at the point where the structure collapses due to sudden buckling of the chiral ligaments.

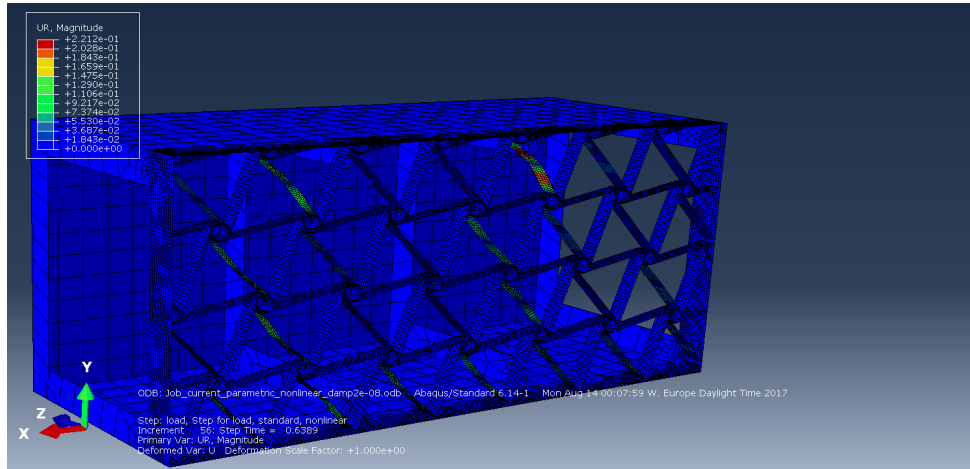


Figure 5.1: Baseline model response when the fraction of load applied equals to 63% of the prescribed load (700 N). Buckling has appeared and it is more severe on the chiral ligament located closer to the inner rib located closer to the root.

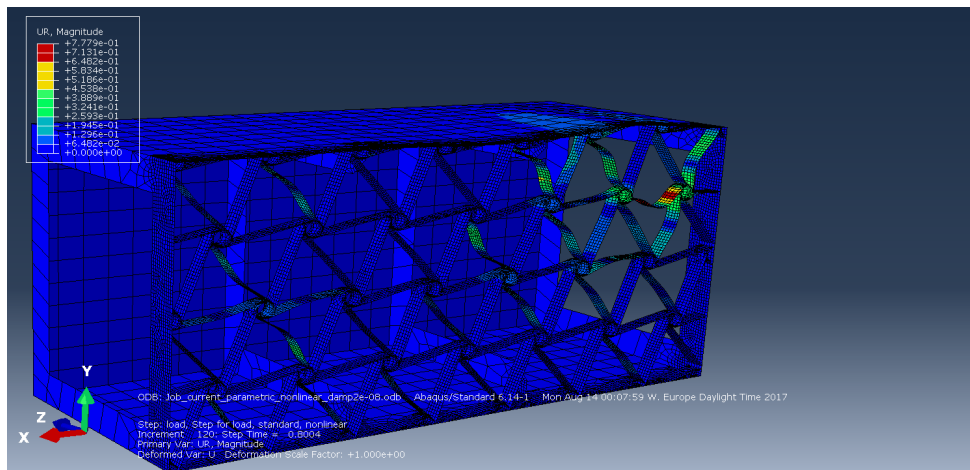


Figure 5.2: Baseline model response when the fraction of load applied equals to 80% of the prescribed load (700 N). Severe buckling appears in those chiral ligaments located at the root and with a higher y coordinate. This is the point when the structure collapses and the twist increases for smaller increments in the applied load.

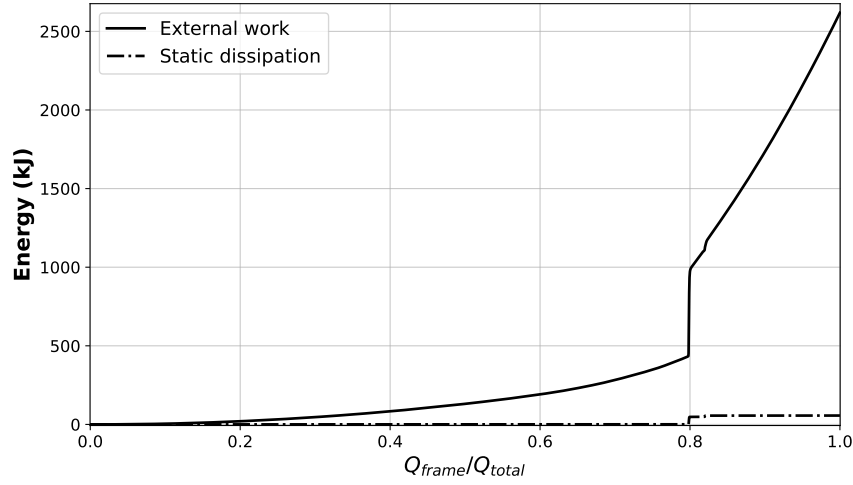


Figure 5.3: External work and static dissipation for a simulation of the baseline configuration. It can be seen that the static dissipation through automatic stabilization is negligible in comparison with the external work showing that the inclusion of artificial damping factor is unluckily to be leading to inaccurate results. The abrupt change in the external work shows the point where structure collapses due to sudden buckling of the chiral ligaments.

In order to see the overall system response as load increases, a load-displacement curve can be plotted. The Figure 5.4 shows the typical twist variation as the load is increased. On this plot, the results from the nonlinear simulations are shown as the set of scatter points while the dotted line represents the forecast final twist from the linear simulation. In the case shown, the linear simulation arises a twist at the tip  $\phi_{tip}$  equal to  $-0.196$  degrees while the nonlinear simulation predicts a final twist of  $-1.248$  degrees. This shows how the problem under study is highly nonlinear.

The nonlinear response also shows the point where the structure collapses that its located at the point where approximately 80% of the load has been applied. The deformation state of the structure at this point was the one shown in Figure 5.2. The plot also, shows another point where the deformation rapidly changes. This point is approximately located at the point where the load fraction is 82%. This shows the structure entering in the second stage of its deformation. Here, the buckling is more generalized and buckling appears in more ligaments apart from those at the root. This can be seen in Figure 5.5. The location of this second deformation breakdown varies widely with the choose of parameters.

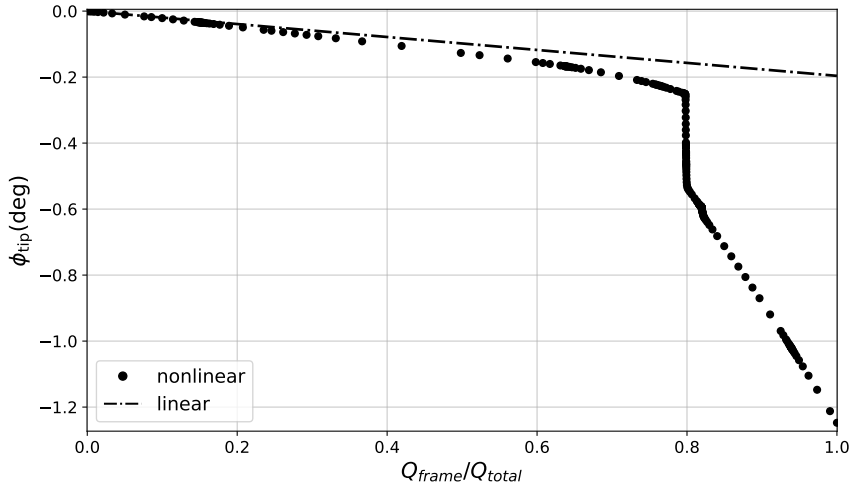


Figure 5.4: Force-displacement curve for the baseline configuration. Two breakdowns for the buckling deformation are shown in the plot. The first one is located at the point where the fraction of applied load equals to 80% and the second one at the point where the fraction is 82%.

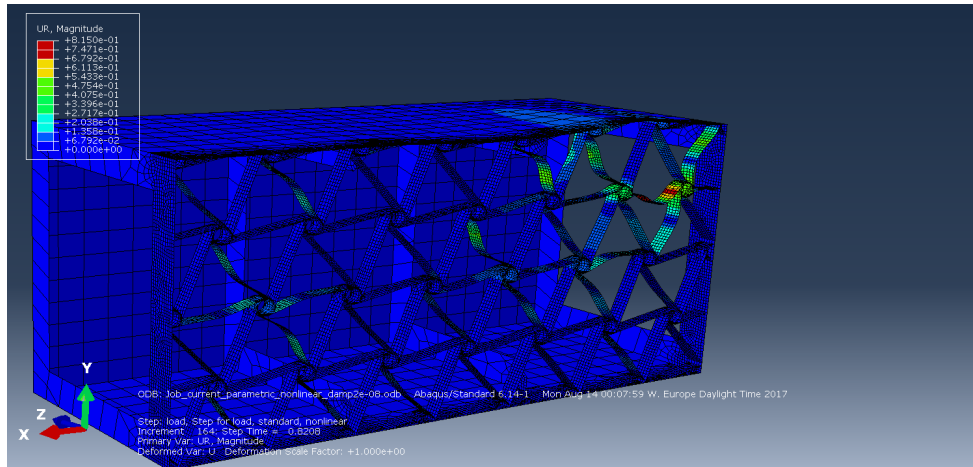


Figure 5.5: Baseline model response when the fraction of load applied equals to 82% of the prescribed load (700 N). In this case, not only the ligaments located at the root show severe buckling but also, other located at different points of the chiral lattice has started to buckle at the same time, inducing rapidly growing deformation for small increments in load.

## 5.3 Parametric study on the computational model

The aim of this section is to show the effect of each parameter on the nonlinear response of the structure. The parameters that will be included in the analysis are the following:

- Wing-box thickness  $t_{\text{box}}$
- Number of unit cells in the transversal direction  $M$
- Number of unit cells in the spanwise direction  $N$
- Chiral node depth  $B_{\text{chiral}}$
- Chiral node radius  $r_{\text{chiral}}$
- Chiral lattice thickness  $t_{\text{chiral}}$
- Chiral ligament half length  $L_{\text{chiral}}$
- Dimensionless ligament eccentricity  $\hat{e}_{\text{chiral}}$

### 5.3.1 Wing-box thickness

In the present subsection the effect of different values for the wing-box thickness  $t_{\text{box}}$  on the structure response is investigated.

The results from the simulations carried out can be seen in Table 5.1. In the table, the twist at the tip of the wing-box for the Abaqus nonlinear simulation  $\phi_{\text{tip}}$  and for the linear simulation  $\tilde{\phi}_{\text{tip}}$  are shown. This result is obtained by evaluating the value of the angular deformation  $u$  at a number of nodes located in different parts of the beam, as explained in the Subsection 4.3.5. Therefore, the maximum deviation from the calculated mean twist has also been included. Finally, the Table 5.1 also shows the maximum vertical displacement found in the nodes located on the upper wing-box skin.

The evolution of the twist as a function of the load applied can be seen in Figure 5.6 for each of the values of  $t_{\text{box}}$  studied. It can be seen how the structure only collapses for  $t_{\text{box}} = 0.8$  mm and the final value of the twist is much higher than for the remaining cases. For this case, the curve shows the post-buckling evolution of the twist response for increasing values of load applied. The slope of the curve has decreased drastically and the twist achieved after all the prescribed load has been applied is equal to  $\phi_{\text{tip}} = -2.15$  deg.

The collapse of the structure for  $t_{\text{box}} = 0.8$  mm appears when 60% of the load has been applied, as shown in Figure 5.7. This last plot represents a detailed view of the force-displacement curve that also shows how the nonlinear response differs from the linear one for all the considered cases.

$t_{\text{box}}(\text{mm})$	$\phi_{\text{tip}}$ (deg)	$e(\phi_{\text{tip}})(\%)$	$\tilde{\phi}_{\text{tip}}$ (deg)	$e(\tilde{\phi}_{\text{tip}})(\%)$	$v_{\max}$	$\hat{z}_{v_{\max}}$	$\hat{x}_{v_{\max}}$
0.8	-2.15	13.575	-0.196	-10.067	-16.908	1	0.334
1	-0.206	9.954	-0.164	-11.316	-1.292	1	0.971
1.2	-0.174	10.288	-0.143	-12.16	-1.081	1	0.971
1.4	-0.158	12.909	-0.13	-14.06	-0.95	1	0.971

Table 5.1: Results from parametric study on the wing-box thickness  $t_{\text{box}}$ . The results show the twist at the tip of the wing-box for the Abaqus nonlinear simulation  $\phi_{\text{tip}}$  and for the linear simulation  $\tilde{\phi}_{\text{tip}}$ . The maximum relative error of the mean calculation, expressed as percentage, for these two magnitudes is  $e(\phi_{\text{tip}})$  and  $e(\tilde{\phi}_{\text{tip}})$ , respectively. The table also shows the maximum vertical displacement  $v_{\max}$  among all the mesh nodes located on the upper skin of the wing-box and the dimensionless position in the spanwise direction  $\hat{x}_{v_{\max}}$  and in the chordwise direction  $\hat{z}_{v_{\max}}$  of the node that shows  $v = v_{\max}$ .

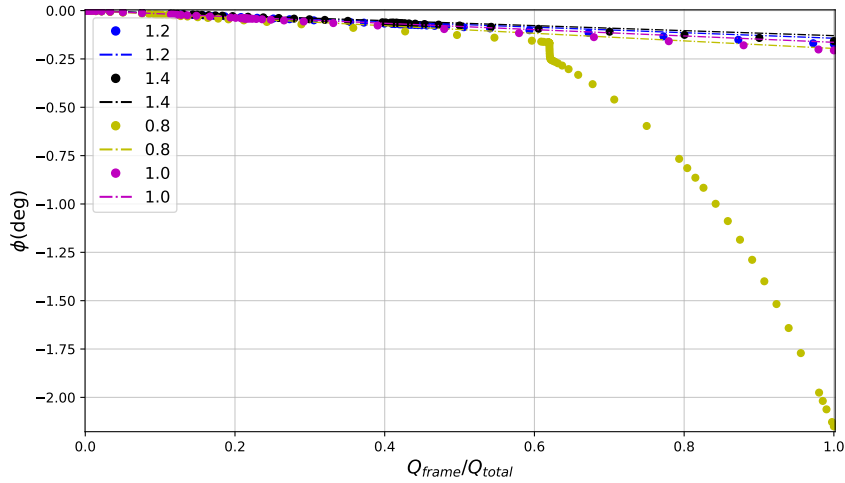


Figure 5.6: Force-displacement curve for various values of the wing-box thickness  $t_{\text{box}}$ . For all the cases shown, the force applied was located on the upper flange of the tip rib and its magnitude was equal to -800 N.

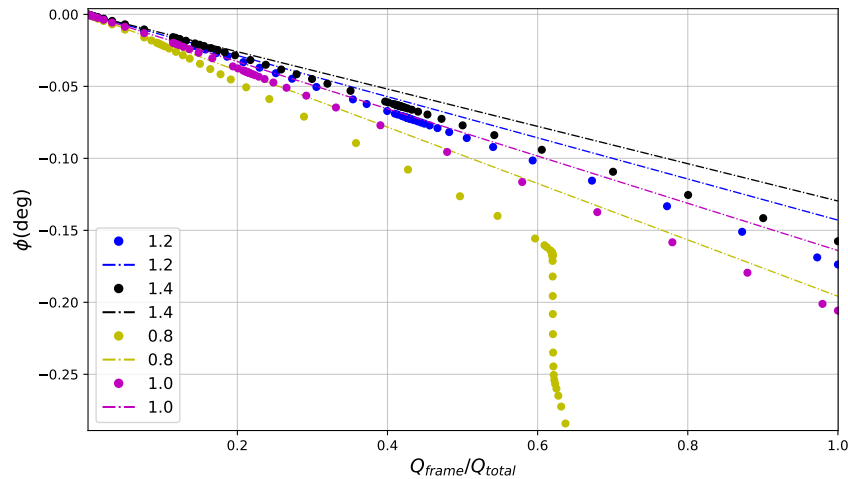


Figure 5.7: Detail of the force-displacement curve for various values of the wing-box thickness  $t_{\text{box}}$ . For all the cases shown, the force applied was located on the upper flange of the tip rib and its magnitude was equal to -800 N.

The differences in response for the different cases are also shown the color contour plots provided by Abaqus visualization module. The deformation in the ligaments for  $t_{\text{box}} = 1.2$  mm when buckling occurs is shown in Figure 5.8 that shows the total rotational displacement of the mesh elements on the color contour. It can be seen that buckling does not propagate to other parts of the lattice and it stays where it had appeared on first place, at the first ligaments after the inner rib located further from the root.

On the other hand, in Figure 5.9 the same plot is shown for a value of wing-box thickness of  $t_{\text{box}} = 0.8$  mm. This figure shows the post-buckling state of the structure. In this region, each of the ligaments that had buckled increase its deformation. There are not any new ligaments starting to buckle. It is possible to see that some local deformation has been induced into the upper skin of the wing-box in between the root and the first inner rib. As shown in Table 5.1, for the case  $t_{\text{box}} = 0.8$  mm, the point with the maximum vertical is shown to appear close to the root, where  $\hat{x}_{v_{\max}} = 0.334$ .

A further study was performed in order to see the relationship between the wing-box thickness and the value of the force applied that induces the structure to collapse. As a result, the plot shown in Figure 5.10 was produced.

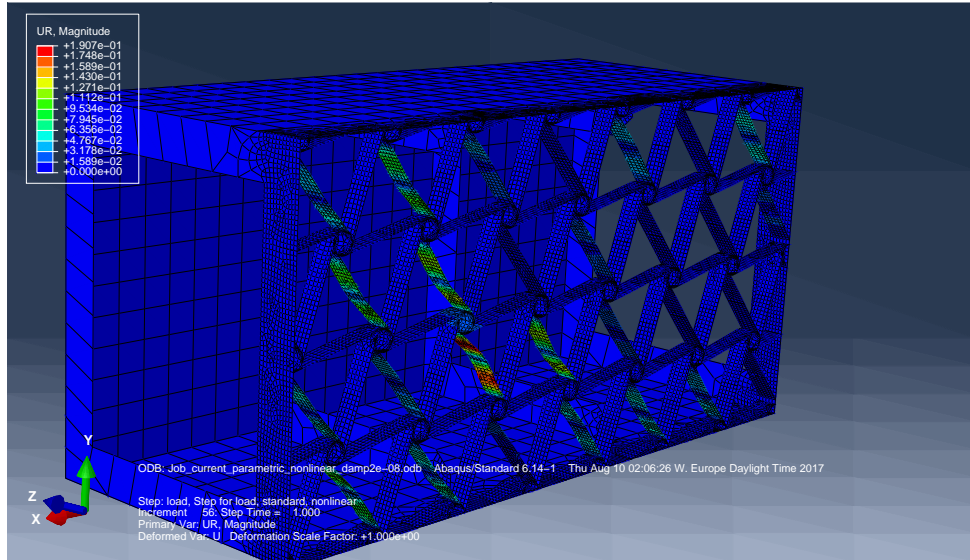


Figure 5.8: Color contour representation of the total angular displacement of the mesh elements on the deformed structure for  $t_{\text{box}} = 1.2 \text{ mm}$ . This case is shown after all the prescribed load (800 N) has been applied.

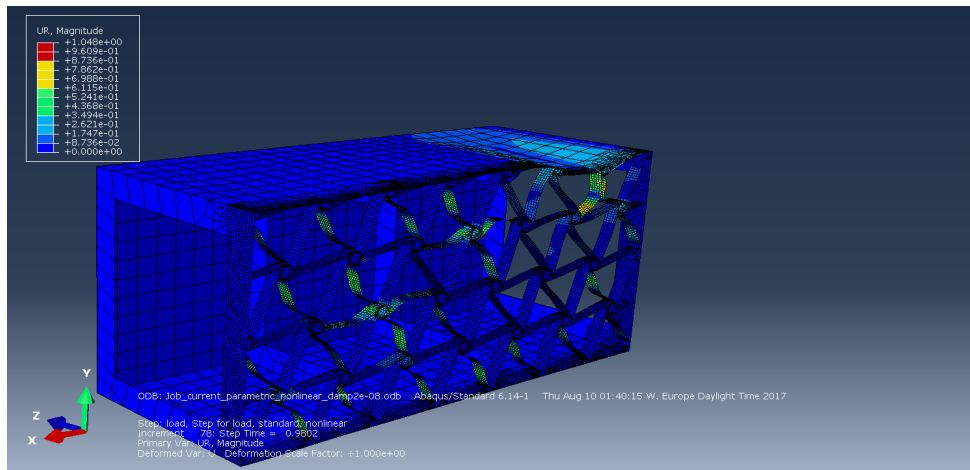


Figure 5.9: Color contour representation of the total angular displacement of the mesh elements on the deformed structure for  $t_{\text{box}} = 0.8 \text{ mm}$ .

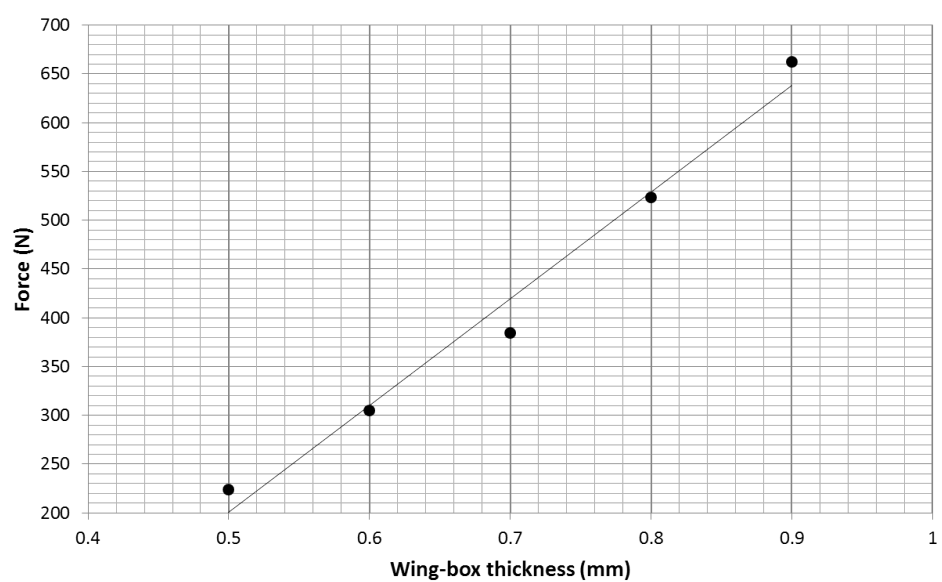


Figure 5.10: Force that induces the structure to collapse as a function of the wing-box thickness  $t_{\text{box}}$ .

### 5.3.2 Number of unit cells in the chiral lattice

Now the effect of the number of units cells in the transversal direction  $M$  and in the spanwise direction  $N$  on the structural response is investigated.

Firstly, the number of unit cells in the transversal direction  $M$  is varied. This parameter modifies the height of the model. Similarly as it was done for the study of the wing-box thickness  $t_{\text{box}}$  influence in the structure response, the results from the different simulations are shown in Table 5.2. Also, the force-displacement curve is shown in Figure 5.11. It can be seen from results that increments a higher  $M$  resulted on a decrement of the structure sensitivity to buckling. For the case of  $M = 5$ , the structure did not collapse under the prescribed load of 1000 N.

$M$	$\phi_{\text{tip}}$ (deg)	$e(\phi_{\text{tip}})$ (%)	$\tilde{\phi}_{\text{tip}}$ (deg)	$e(\tilde{\phi}_{\text{tip}})$ (%)	$v_{\max}$	$\hat{z}_{v_{\max}}$	$\hat{x}_{v_{\max}}$
3	-5.179	13.559	-0.245	-10.074	-29.166	1	0.971
4	-0.392	22.16	-0.148	-10.447	-6.093	1	0.334
5	-0.214	14.893	-0.164	-17.526	-1.018	0.6	0.971

Table 5.2: Results from parametric study on the number of unit cells in the transversal direction  $M$ . The results show the twist at the tip of the wing-box for the Abaqus nonlinear simulation  $\phi_{\text{tip}}$  and for the linear simulation  $\tilde{\phi}_{\text{tip}}$ . The maximum relative error of the mean calculation, expressed as percentage, for these two magnitudes is  $e(\phi_{\text{tip}})$  and  $e(\tilde{\phi}_{\text{tip}})$ , respectively. The table also shows the maximum vertical displacement  $v_{\max}$  among all the mesh nodes located on the upper skin of the wing-box and the dimensionless position in the spanwise direction  $\hat{x}_{v_{\max}}$  and in the chordwise direction  $\hat{z}_{v_{\max}}$  of the node that shows  $v = v_{\max}$ .

From the results shown in Table 5.5 it can be seen how for the case of  $M = 3$ , the point that shows  $v = v_{\max}$  is located at the wing-box tip where  $\hat{x}_{v_{\max}} = 0.971$ , due to the high twist of the structure. However, for  $M = 4$ , the structure has gained stiffness in shear and, even the prescribed load makes the structure to collapse when buckling phenomena appears, the achieved twist  $\phi_{\text{tip}}$  is  $\approx 7\%$  inferior than what it was obtained for  $M = 3$ . For  $M = 5$ , the structure is so stiff that  $v_{\max}$  appears approximately at the point where the load is applied. This shows that deformation is only achieved in the vicinity of the load introduction point due to the high stiffness in shear of the structure.

The effects of the variation of the number of unit cells in the spanwise direction  $N$ , parameter responsible of the wing-box length is investigated next. The results from the parametric study carried out are shown in Table 5.3. The force-displacement curve for the simulations carried out is shown in Figure 5.12. It can be seen that the bigger the wing-box length, the earlier that the buckling of the lattices cause the collapse of the structure.

In the last plot introduced it can be seen a second change in the slope of the curve for the cases of  $N = 10$  and  $N = 11$ . This happens when, as explained in Section 5.2, the buckling phenomena progresses from the ligaments at the root to be more generalized in other parts of the structure. This characteristic can be seen in Figure 5.13, where the response of the structure for the case of  $N = 10$  and load fraction of 96% is shown.

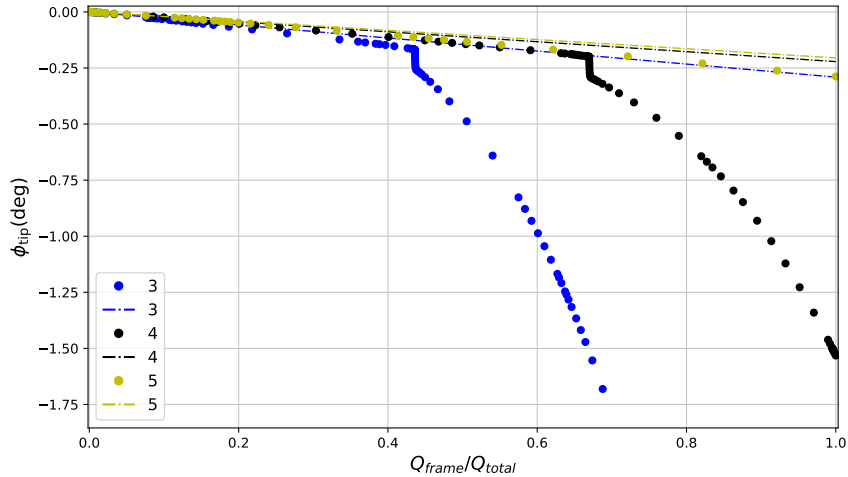


Figure 5.11: Force-displacement curve for various values of the number of unit cells in the transversal direction  $M$ . For all the cases shown, the load introduction point was located in the middle of the upper flange of the tip rib and its magnitude was equal to -1200 N.

$N$	$\phi_{\text{tip}}$ (deg)	$e(\phi_{\text{tip}})$ (%)	$\tilde{\phi}_{\text{tip}}$ (deg)	$e(\tilde{\phi}_{\text{tip}})$ (%)	$v_{\max}$	$\hat{z}_{v_{\max}}$	$\hat{x}_{v_{\max}}$
7	-0.185	16.474	-0.14	-12.506	-1.061	1	0.971
8	-0.878	9.517	-0.17	-10.196	-9.844	1	0.334
9	-4.582	11.091	-0.209	-7.848	-25.781	1	0.971
10	-8.116	6.192	-0.248	-6.398	-46.636	1	0.971
11	-17.659	4.954	-0.299	-5.098	-107.229	1	0.971
12	-22.007	6.527	-0.337	-3.08	-137.131	1	0.971

Table 5.3: Results from parametric study on the number of unit cells in the spanwise direction  $M$ . The results show the twist at the tip of the wing-box for the Abaqus nonlinear simulation  $\phi_{\text{tip}}$  and for the linear simulation  $\tilde{\phi}_{\text{tip}}$ . The maximum relative error of the mean calculation, expressed as percentage, for these two magnitudes is  $e(\phi_{\text{tip}})$  and  $e(\tilde{\phi}_{\text{tip}})$ , respectively. The table also shows the maximum vertical displacement  $v_{\max}$  among all the mesh nodes located on the upper skin of the wing-box and the dimensionless position in the spanwise direction  $\hat{x}_{v_{\max}}$  and in the chordwise direction  $\hat{z}_{v_{\max}}$  of the node that shows  $v = v_{\max}$ .

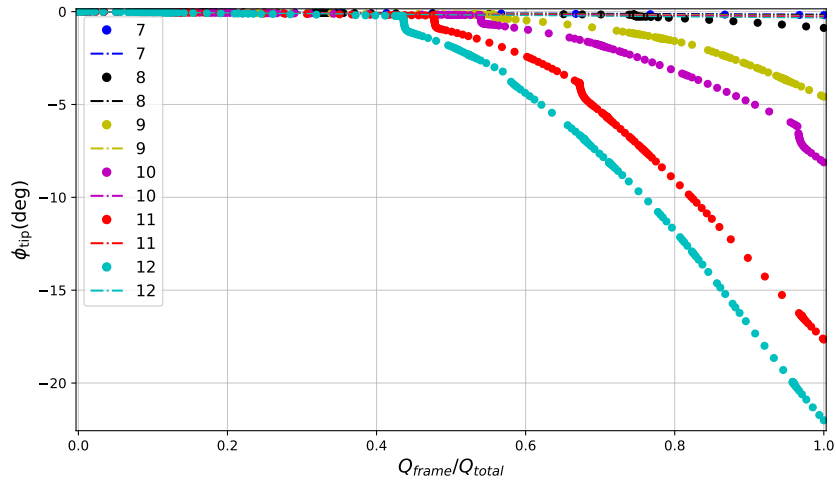


Figure 5.12: Force-displacement curve for various values of the number of unit cells in the spanwise direction  $N$ . For all the cases shown, the load introduction point was located in the middle of the upper flange of the tip rib and its magnitude was equal to -700 N.

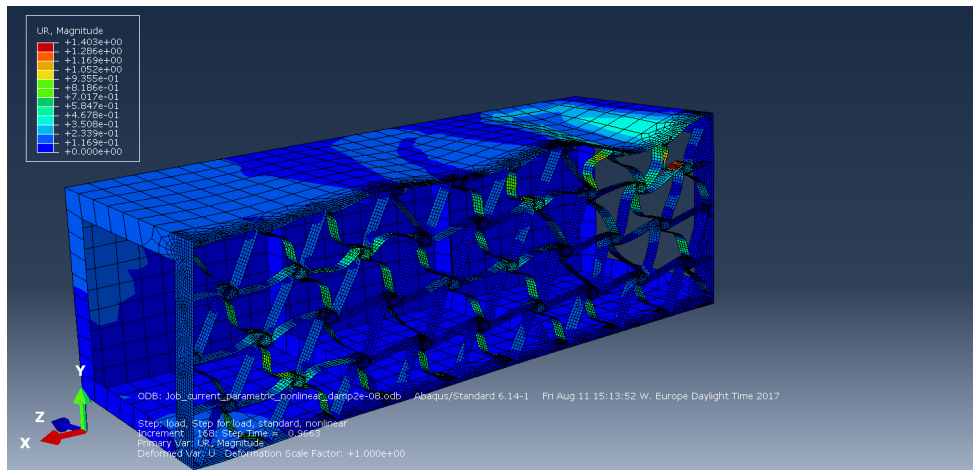


Figure 5.13: Model response when the fraction of load applied equals to 96% of the prescribed load (700 N) and  $N = 10$ . The plot shows how the buckling phenomena is generalized for the whole chiral structure.

### 5.3.3 Chiral lattice parameters

In the present subsection, different parameters of the chiral lattice structure are varied and its effect of the system response are shown.

#### Dimensionless chiral ligament eccentricity $\hat{e}_{\text{chiral}}$

The first of the chiral parameter that is going to be studied is the ligament eccentricity  $e_{\text{chiral}}$ , in its dimensionless form  $\hat{e}_{\text{chiral}}$ . The numeric results from the simulations carried out can be seen in Table 5.4.

The force-deformation curve for the range of simulations carried out can be seen in Figure 5.14. Here it can be seen that the collapse of the structure occurs for all the cases except for  $\hat{e}_{\text{chiral}}=0.1$ . The deformation state of the structure for this case can be seen in Figure 5.15 that shows how the excessive eccentricity of the ligaments keep them from buckling and causing the structure collapse.

$\hat{e}_{\text{chiral}}$	$\phi_{\text{tip}}$ (deg)	$e(\phi_{\text{tip}})$ (%)	$\tilde{\phi}_{\text{tip}}$ (deg)	$e(\tilde{\phi}_{\text{tip}})$ (%)	$v_{\max}$	$\hat{z}_{v_{\max}}$	$\hat{x}_{v_{\max}}$
0.0	-0.903	9.547	-0.166	-10.14	-9.806	1	0.334
0.001	-1.314	13.715	-0.168	-9.931	-12.441	1	0.334
0.01	-0.877	9.525	-0.17	-10.196	-9.831	1	0.334
0.05	-0.724	9.511	-0.188	-10.598	-8.483	1	0.334
0.1	-0.222	9.444	-0.194	-10.601	-1.416	1	0.971

Table 5.4: Results from parametric study on chiral ligament eccentricity  $\hat{e}_{\text{chiral}}$ . The results show the twist at the tip of the wing-box for the Abaqus nonlinear simulation  $\phi_{\text{tip}}$  and for the linear simulation  $\tilde{\phi}_{\text{tip}}$ . The maximum relative error of the mean calculation, expressed as percentage, for these two magnitudes is  $e(\phi_{\text{tip}})$  and  $e(\tilde{\phi}_{\text{tip}})$ , respectively. The table also shows the maximum vertical displacement  $v_{\max}$  among all the mesh nodes located on the upper skin of the wing-box and the dimensionless position in the spanwise direction  $\hat{x}_{v_{\max}}$  and in the chordwise direction  $\hat{z}_{v_{\max}}$  of the node that shows  $v = v_{\max}$ .

The Figure 5.14 also shows that the case of  $\hat{e}_{\text{chiral}}=0.0$ , that is when the ligaments are flat, is not the case that shows the structure as more sensitive to buckling. Instead, for  $\hat{e}_{\text{chiral}}=0.001$  the structure collapses at a smaller load. In order to investigate the load required to make the structure collapse for each particular value of  $t_{\text{chiral}}$ , the plot shown in Figure 5.16 was produced. This shows a minimum for  $\hat{e}_{\text{chiral}}=0.001$  showing that different buckling mechanism occurs when the eccentricity is null and when it is not. To investigate this characteristic, the deformed state of the structure is shown for  $\hat{e}_{\text{chiral}}=0.0$  and  $\hat{e}_{\text{chiral}}=0.001$  in Figures 5.17 and 5.18, respectively. This shows effectively, that the buckling mechanism change from case to case. When the eccentricity is null, the structure collapses when buckling appears in two ligaments at the upper part of the root making them to deform and displace the one against the other. However, when the eccentricity is not null, these two ligaments where buckling occurs displace in the same direction towards decreasing values of  $x$ .

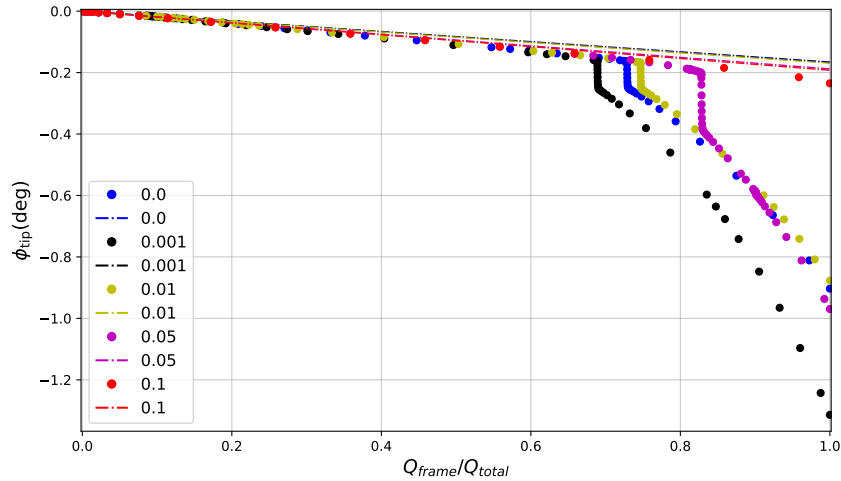


Figure 5.14: Force-displacement curve for various values of the dimensionless chiral ligament eccentricity  $\hat{\epsilon}_{\text{chiral}}$ . The plot shows how the collapse of the structure occurs for all the cases except for  $\hat{\epsilon}_{\text{chiral}}=0.1..$

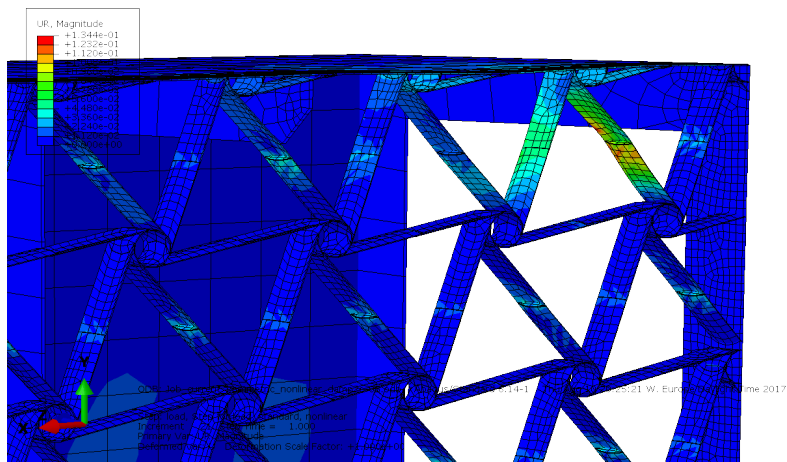


Figure 5.15: Model response when the fraction of load applied equals to 100% of the prescribed load (700 N) and  $\hat{\epsilon}_{\text{chiral}}=0.1$ . For this case, the excessive ligament eccentricity at the end of the simulation keeps it from buckling and causing the structure collapse.

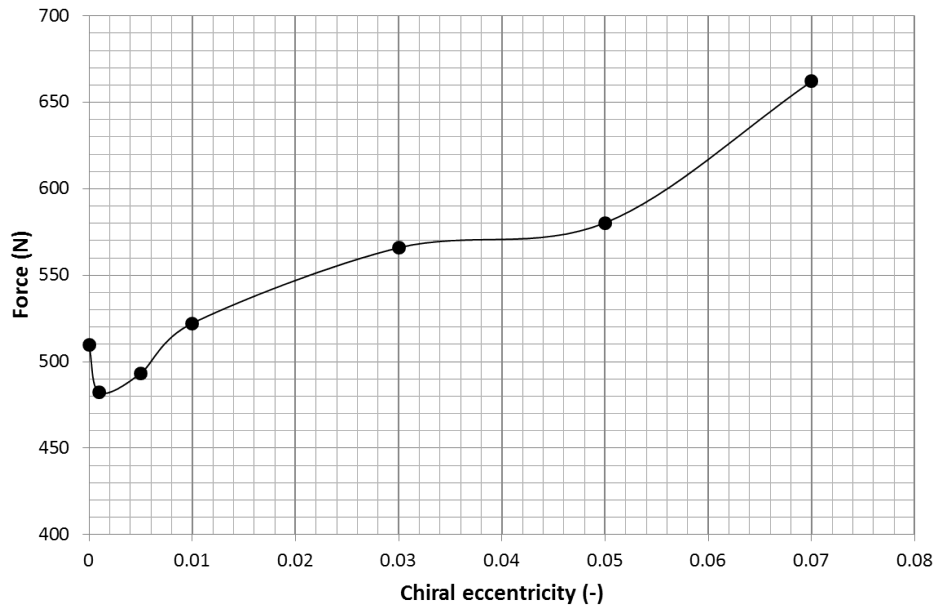


Figure 5.16: Force that induces the structure to collapse as a function of the chiral ligament eccentricity  $\hat{e}_{\text{chiral}}$ . It can be seen that the .

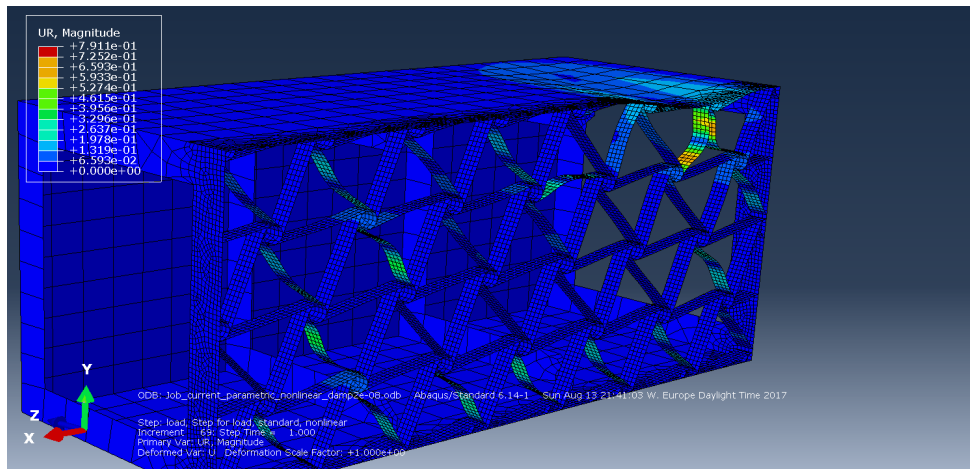


Figure 5.17: Model response when the fraction of load applied equals to 72% of the prescribed load (700 N) and  $\hat{e}_{\text{chiral}} = 0.0$ . For this case, the structure collapse occurs when buckling appears on the ligaments located at the upper part of the root. The deformation makes ligaments to displace the one against each other.

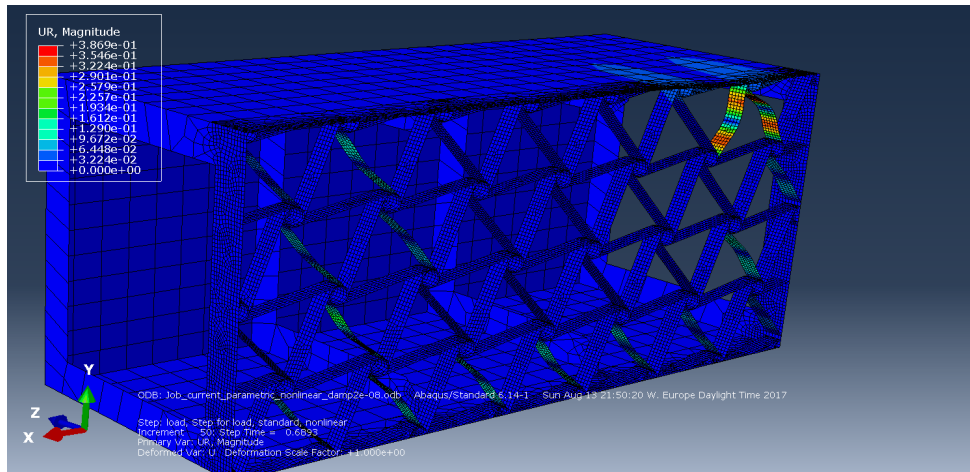


Figure 5.18: Model response when the fraction of load applied equals to 68% of the prescribed load (700 N) and  $\hat{\epsilon}_{\text{chiral}} = 0.001$ . For this case, the structure collapse occurs when buckling appears on the ligaments located at the upper part of the root. The deformation makes ligaments to displace in the same direction towards decreasing values of  $x$ .

### Chiral node depth $B_{\text{chiral}}$

The numeric results from the parametric analysis on the chiral node depth  $B_{\text{chiral}}$  can be seen in Table 5.5. The force-displacement curve can be seen in Figure 5.19 for various values of  $B$ . This plot shows how the bigger  $B_{\text{chiral}}$  is, the more abrupt the collapse is, showing a bigger sudden increment on the measured twist at the tip  $\phi_{\text{tip}}$ .

The Figure 5.20 shows the rotation  $u$  around the  $x$  direction of the mesh elements located on the upper skin of the wing-box and close to the root. This is represented for the case of  $B_{\text{chiral}} = 30$  mm, at the moment when collapse of the structure occurs which is at 86% of the prescribed load and in the area where local deformation of the skin takes place. Examination of the plot arises that the value of  $u$  in this area is approximately double to that corresponding to  $B_{\text{chiral}} = 10$  mm which can be seen in Figure 5.21. This shows that the bigger  $B_{\text{chiral}}$  is, the more area is affected by the ligaments deformation when buckling occurs and the greater the local deformation will be.

When plotting the force that makes the structure to collapse against the corresponding value of chiral node depth depth  $B_{\text{chiral}}$ , the Figure 5.22 was produced.

$t_{\text{chiral}}$	$\phi_{\text{tip}}$ (deg)	$e(\phi_{\text{tip}})$ (%)	$\tilde{\phi}_{\text{tip}}$ (deg)	$e(\tilde{\phi}_{\text{tip}})$ (%)	$v_{\max}$	$\hat{z}_{v_{\max}}$	$\hat{x}_{v_{\max}}$
10	-1.082	9.61	-0.187	-10.614	-10.941	1	0.334
20	-0.877	9.525	-0.17	-10.196	-9.831	1	0.334
30	-0.71	9.528	-0.16	-9.838	-8.75	1	0.334

Table 5.5: Results from parametric study on chiral node depth  $B_{\text{chiral}}$ . The results show the twist at the tip of the wing-box for the Abaqus nonlinear simulation  $\phi_{\text{tip}}$  and for the linear simulation  $\tilde{\phi}_{\text{tip}}$ . The maximum relative error of the mean calculation, expressed as percentage, for these two magnitudes is  $e(\phi_{\text{tip}})$  and  $e(\tilde{\phi}_{\text{tip}})$ , respectively. The table also shows the maximum vertical displacement  $v_{\max}$  among all the mesh nodes located on the upper skin of the wing-box and the dimensionless position in the spanwise direction  $\hat{x}_{v_{\max}}$  and in the chordwise direction  $\hat{z}_{v_{\max}}$  of the node that shows  $v = v_{\max}$ .

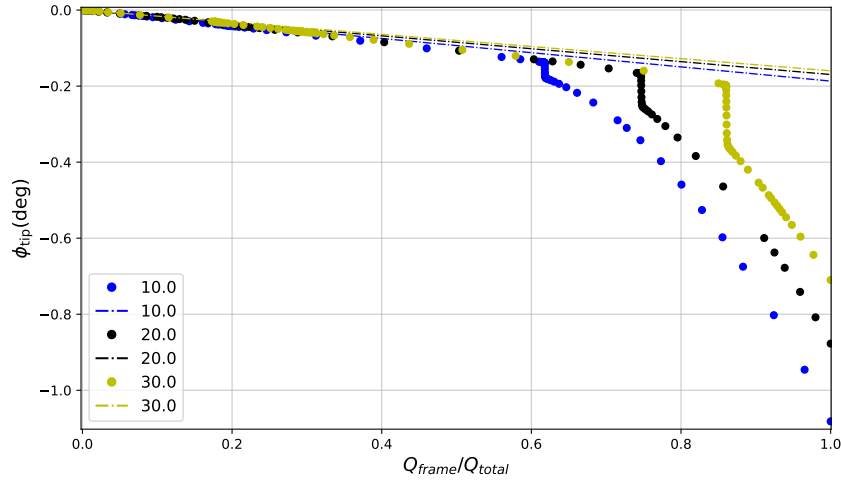


Figure 5.19: Force-displacement curve for various values of the dimensionless chiral node depth  $B_{chiral}$ . Results show how the bigger the node depth  $B_{chiral}$  is, the later the collapse of the structure occurs but the more abrupt is its.

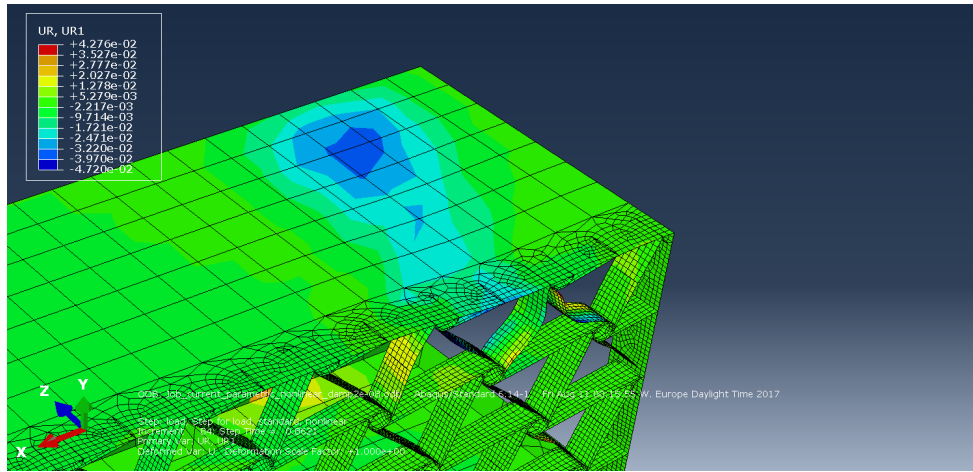


Figure 5.20: Model response when the fraction of load applied equals to 86% of the prescribed load (700 N) and  $B_{chiral}=30$  mm. The plot shows a color contour with the value of the rotational displacement  $u$  around the  $x$  direction at the moment in which the structure collapses. In the area where the local deformation occurs, the value of  $u$  is approximately equal to  $-0.033$  rad.

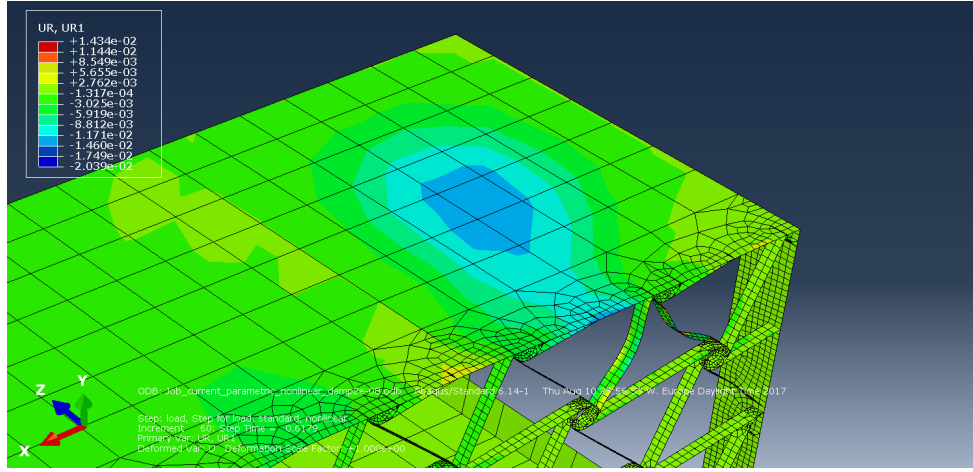


Figure 5.21: Model response when the fraction of load applied equals to 62% of the prescribed load (700 N) and  $B_{\text{chiral}} = 10 \text{ mm}$ . The plot shows a color contour with the value of the rotational displacement  $u$  around the  $x$  direction at the moment in which the structure collapses. In the area where the local deformation occurs, the value of  $u$  is approximately equal to  $-0.015 \text{ rad}$ .

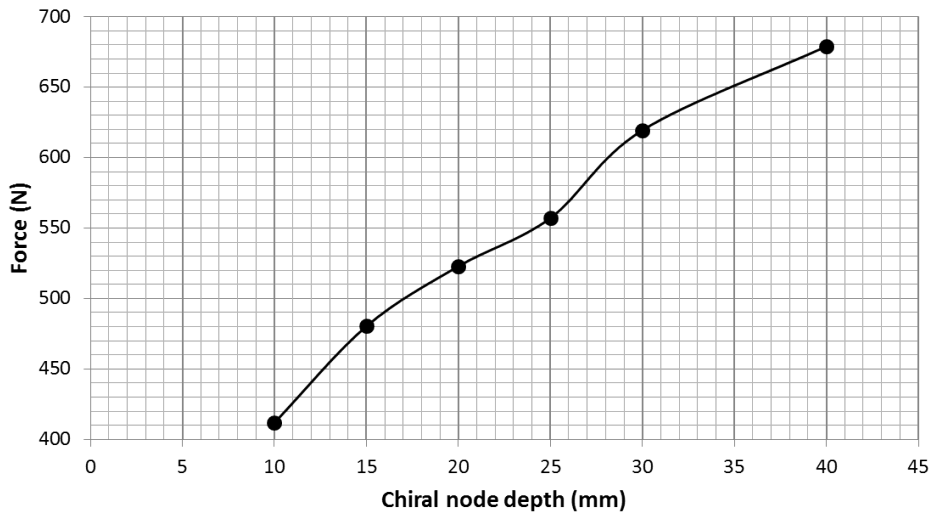


Figure 5.22: Force that induces the structure to collapse as a function of the chiral node depth  $B_{\text{chiral}}$ .

### Chiral node radius $r_{\text{chiral}}$

In the case of the chiral node radius  $r_{\text{chiral}}$ , the possible values were limited by the geometry of the chiral lattice. For values  $r_{\text{chiral}} \leq 5$  mm, it was not possible to build the mode due to interferences between the different ligaments that joined at each of the nodes. The numeric results from the simulations are presented in Table 5.6.

The force-displacement curve obtained from the simulations is shown in Figure 5.23. This curve shows how the structure collapses for analyzed cases except for  $r_{\text{chiral}} = 17.5$  mm and  $r_{\text{chiral}} = 20$  mm. For  $r_{\text{chiral}} = 12.5$  mm, the buckling ligaments are located at the root, as it can be seen in Figure 5.24. However, for the case of  $r_{\text{chiral}} = 17.5$  mm, buckling do not occur on the ligaments located at the root but in those located just after the inner rib located closer to the root, with smaller  $x$ . This explains the characteristic seen in Figure 5.23 for the case of  $r_{\text{chiral}} = 17.5$  mm which breaks the trend followed by values  $r_{\text{chiral}} < 17.5$  mm. Then, the chiral node radius  $r_{\text{chiral}}$  value shifts the position of the buckling ligaments that origin the collapse of the structure.

The variation of the force that makes the structure to collapse as a function of the chiral node radius  $r_{\text{chiral}}$  can be seen in Figure 5.26.

$r_{\text{chiral}}$	$\phi_{\text{tip}}$ (deg)	$e(\phi_{\text{tip}})(\%)$	$\tilde{\phi}_{\text{tip}}$ (deg)	$e(\tilde{\phi}_{\text{tip}})(\%)$	$v_{\max}$	$\hat{z}_{v_{\max}}$	$\hat{x}_{v_{\max}}$
7.5	-1.184	13.64	-0.171	-10.046	-11.586	1	0.331
10	-0.877	9.525	-0.17	-10.196	-9.831	1	0.334
12.5	-0.886	9.596	-0.17	-10.247	-10.051	1	0.337
15	-1.121	13.638	-0.173	-10.134	-11.677	1	0.342
17.5	-0.273	9.481	-0.171	-10.215	-4.169	1	0.568
20	-0.229	12.686	-0.171	-8.848	-1.433	1	1.026

Table 5.6: Results from parametric study on chiral node radius  $r_{\text{chiral}}$ . The results show the twist at the tip of the wing-box for the Abaqus nonlinear simulation  $\phi_{\text{tip}}$  and for the linear simulation  $\tilde{\phi}_{\text{tip}}$ . The maximum relative error of the mean calculation, expressed as percentage, for these two magnitudes is  $e(\phi_{\text{tip}})$  and  $e(\tilde{\phi}_{\text{tip}})$ , respectively. The table also shows the maximum vertical displacement  $v_{\max}$  among all the mesh nodes located on the upper skin of the wing-box and the dimensionless position in the spanwise direction  $\hat{x}_{v_{\max}}$  and in the chordwise direction  $\hat{z}_{v_{\max}}$  of the node that shows  $v = v_{\max}$ .

### Chiral ligament half length $L_{\text{chiral}}$

The numeric results obtained for the parametric study on the chiral ligament half length  $L_{\text{chiral}}$  are shown in Table 5.7. The force-displacement curve for the set of values analyzed is shown in Figure 5.27. This plot shows that the bigger the ligament half length is, the earlier that the structure will collapse after severe buckling of the ligaments at the root. For the case of  $L_{\text{chiral}} = 30$ , the structure does not collapse as the structure has become very stiff.

Again, in a further step, the force that causes the structure to collapse for a given value of the half

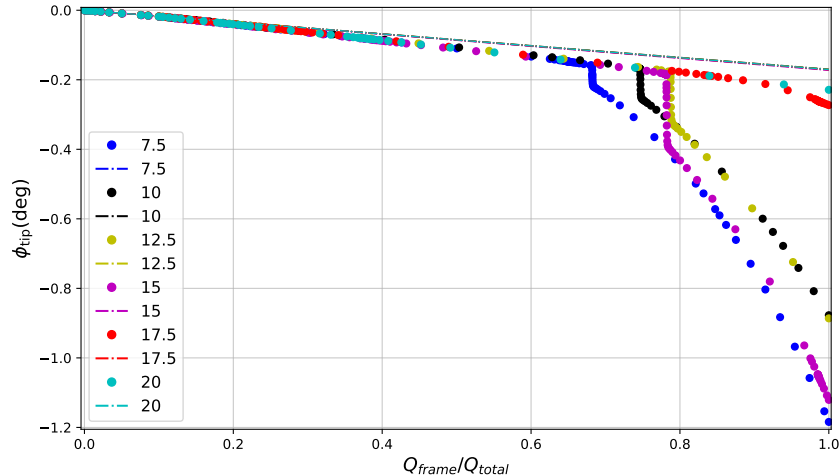


Figure 5.23: Force-displacement curve for various values of the chiral node radius  $r_{\text{chiral}}$ .

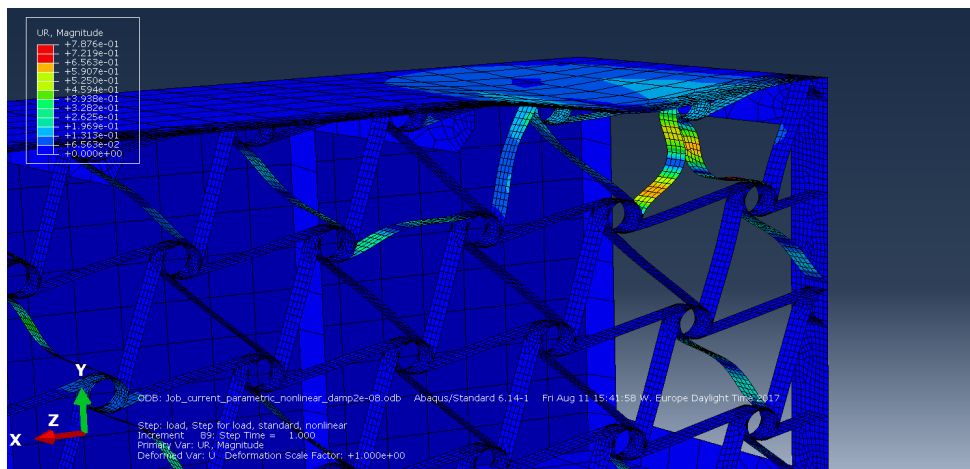


Figure 5.24: Model response when the fraction of load applied equals to 100% of the prescribed load (700 N) and  $r_{\text{chiral}} = 12.5$  mm. Results show that buckling occurs here for ligaments located at the root, as shown in for the baseline configuration.

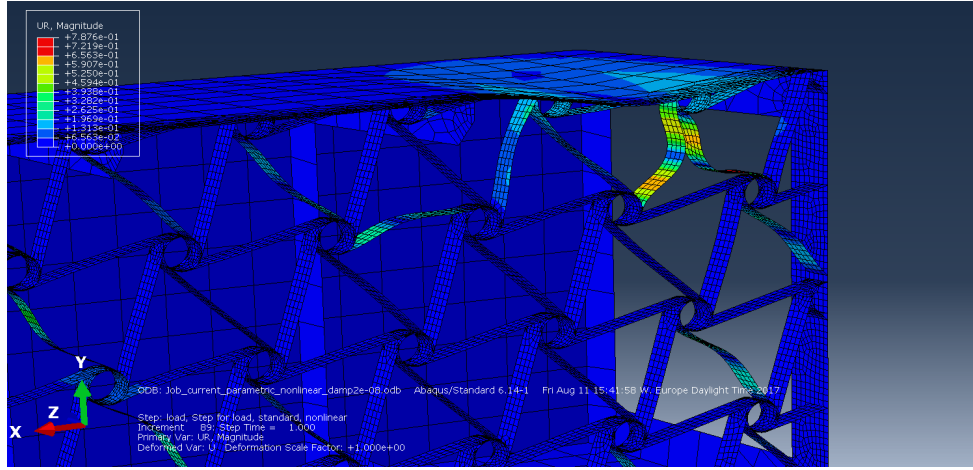


Figure 5.25: Model response when the fraction of load applied equals to 100% of the prescribed load (700 N) and  $r_{\text{chiral}} = 17.5$  mm. Here, the excessive value of

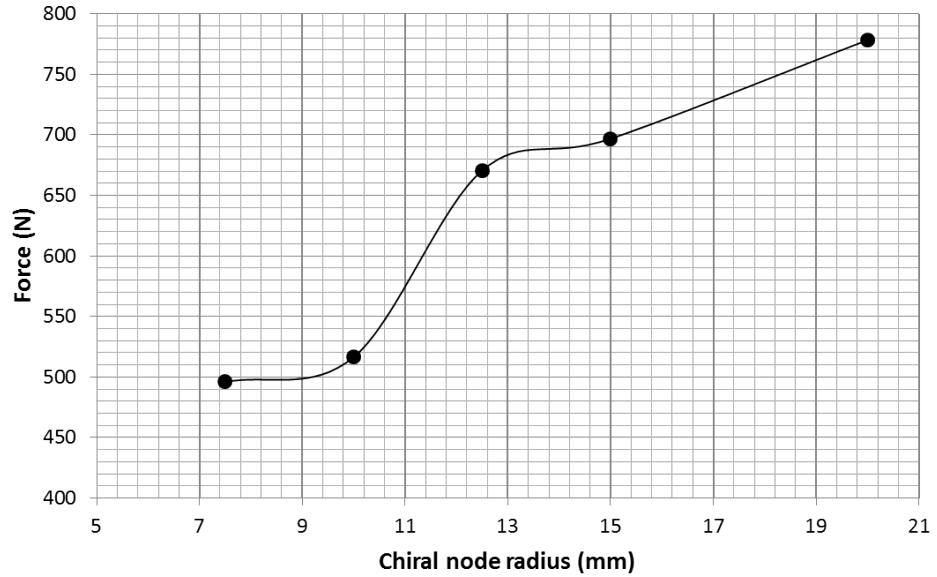


Figure 5.26: Force that induces the structure to collapse as a function of the chiral node radius  $r_{\text{chiral}}$ .

length  $L_{\text{chiral}}$  parameter was investigated. The resulting plot is shown in Figure 5.28.

$L_{\text{chiral}}$	$\phi_{\text{tip}}$ (deg)	$e(\phi_{\text{tip}})$ (%)	$\tilde{\phi}_{\text{tip}}$ (deg)	$e(\tilde{\phi}_{\text{tip}})$ (%)	$v_{\max}$	$\hat{z}_{v_{\max}}$	$\hat{x}_{v_{\max}}$
30	-0.162	11.739	-0.124	-9.441	-1.032	1	0.602
50	-0.877	9.525	-0.170	-10.196	-9.831	1	0.334
70	-4.374	8.563	-0.205	-9.915	-27.936	1	0.463

Table 5.7: Results from parametric study on chiral ligament half length  $r_{\text{chiral}}$ . The results show the twist at the tip of the wing-box for the Abaqus nonlinear simulation  $\phi_{\text{tip}}$  and for the linear simulation  $\tilde{\phi}_{\text{tip}}$ . The maximum relative error of the mean calculation, expressed as percentage, for these two magnitudes is  $e(\phi_{\text{tip}})$  and  $e(\tilde{\phi}_{\text{tip}})$ , respectively. The table also shows the maximum vertical displacement  $v_{\max}$  among all the mesh nodes located on the upper skin of the wing-box and the dimensionless position in the spanwise direction  $\hat{x}_{v_{\max}}$  and in the chordwise direction  $\hat{z}_{v_{\max}}$  of the node that shows  $v = v_{\max}$ .

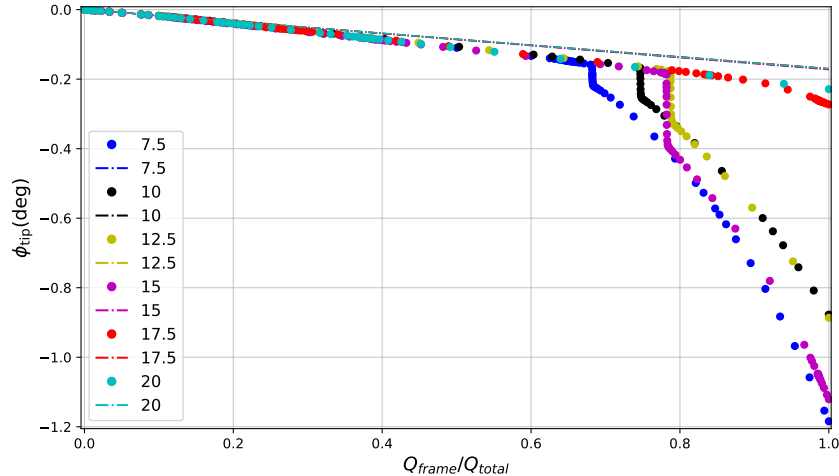


Figure 5.27: Force-displacement curve for various values of the chiral ligament half length  $L_{\text{chiral}}$ . The bigger the ligament half length is, the earlier that the structure will collapse after severe buckling of the ligaments at the root.

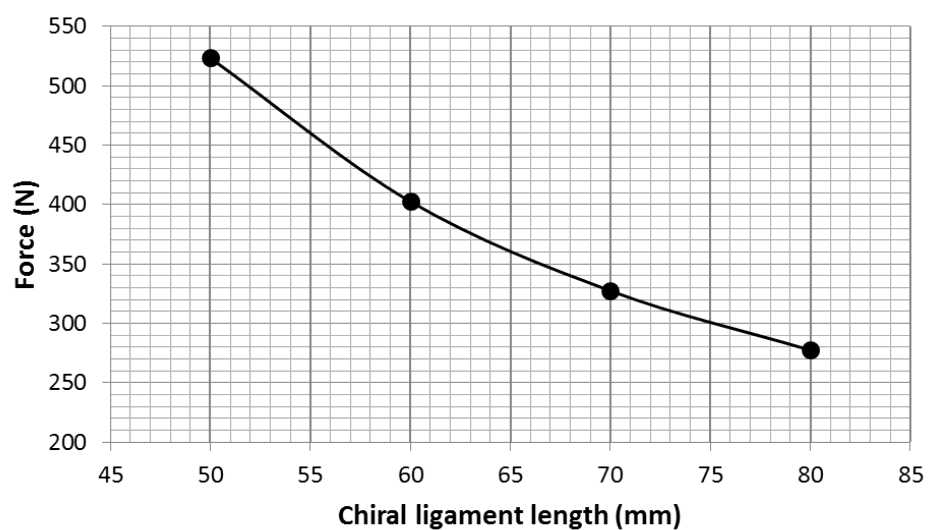


Figure 5.28: Force that induces the structure to collapse as a function of the chiral ligament half length  $L_{\text{chiral}}$ .

**Chiral structure thickness  $t_{\text{chiral}}$** 

The results for the parametric study performed on the chiral structure thickness  $t_{\text{chiral}}$  are shown in Table 5.8. The force-displacement curve is shown in Figure 5.29. Here it can be seen that a thicker chiral structure delays the structure collapse. Similarly as it occurred for the chiral node depth  $B_{\text{chiral}}$ , the more bigger the thickness  $t_{\text{chiral}}$  is, the more abrupt is the decrement in tip twist is.

Finally, the required force to induce the structure to collapse was plot against the corresponding value of the chiral structure thickness  $t_{\text{chiral}}$ , resulting on the curve shown in Figure 5.30.

$t_{\text{chiral}}$	$\phi_{\text{tip}}$ (deg)	$e(\phi_{\text{tip}})$ (%)	$\tilde{\phi}_{\text{tip}}$ (deg)	$e(\tilde{\phi}_{\text{tip}})$ (%)	$v_{\max}$	$\hat{z}_{v_{\max}}$	$\hat{x}_{v_{\max}}$
0.2	-1.201	9.464	-0.199	-10.637	-11.878	1	0.334
0.4	-1.026	9.503	-0.179	-10.334	-10.896	1	0.334
0.6	-0.922	13.874	-0.164	-9.816	-10.036	1	0.334
0.8	-0.232	14.445	-0.15	-9.323	-1.449	1	0.971

Table 5.8: Results from parametric study on chiral structure thickness  $t_{\text{chiral}}$ . The results show the twist at the tip of the wing-box for the Abaqus nonlinear simulation  $\phi_{\text{tip}}$  and for the linear simulation  $\tilde{\phi}_{\text{tip}}$ . The maximum relative error of the mean calculation, expressed as percentage, for these two magnitudes is  $e(\phi_{\text{tip}})$  and  $e(\tilde{\phi}_{\text{tip}})$ , respectively. The table also shows the maximum vertical displacement  $v_{\max}$  among all the mesh nodes located on the upper skin of the wing-box and the dimensionless position in the spanwise direction  $\hat{x}_{v_{\max}}$  and in the chordwise direction  $\hat{z}_{v_{\max}}$  of the node that shows  $v = v_{\max}$ .

Figure 5.29: Force-displacement curve for various values of the chiral structure thickness  $t_{\text{chiral}}$ . The bigger the ligament half length is, the earlier that the structure will collapse after severe buckling of the ligaments at the root.

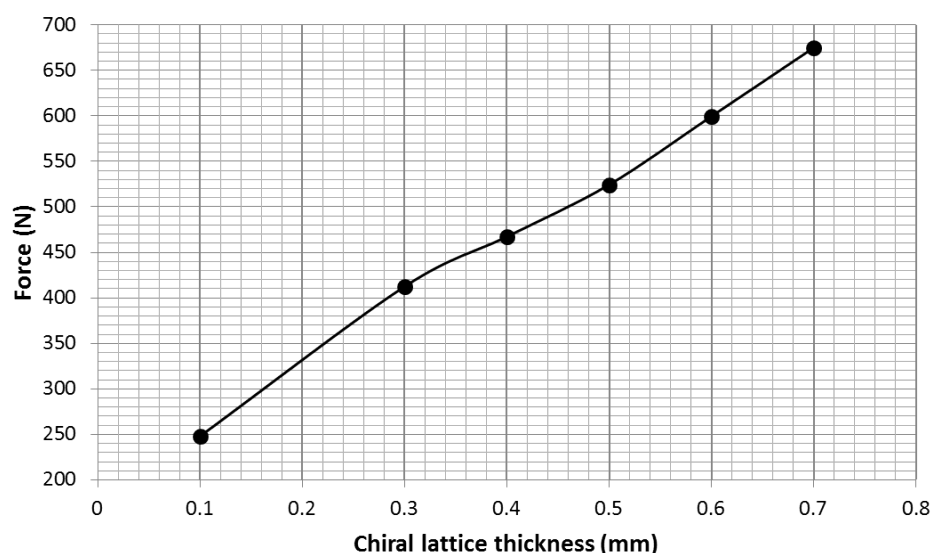


Figure 5.30: Force that induces the structure to collapse as a function of the chiral structure thickness  $t_{\text{chiral}}$ .

# Bibliography

- [1] “Part of “the dream of flight” online exhibit in the American Treasures section at the U.S. Library of Congress..” <http://www.loc.gov/exhibits/treasures/images/>. Accessed: 29 July 2017.
- [2] P. a. Lloyd, “Requirements for smart materials,” *Proceedings of the Institution of Mechanical Engineers, Part G: Journal of Aerospace Engineering*, vol. 221, no. 4, pp. 417–478, 2007.
- [3] S. Boye, “A passenger aircraft with a downwardly foldable wing tip device.” UK Patent: GB2524827. Available at: <https://www.gov.uk/browse/business/intellectual-property/>, 2015. Accessed: 27 July 2017.
- [4] S. Barbarino, O. Bilgen, R. M. Ajaj, M. I. Friswell, and D. J. Inman, “A Review of Morphing Aircraft,” *Journal of Intelligent Material Systems and Structures*, vol. 22, no. 9, pp. 823–877, 2011.
- [5] G. D. Miller, “ACTIVE FLEXIBLE WING (AFW) TECHNOLOGY,” tech. rep., 1988.
- [6] E. Pendleton, P. Flick, D. Paul, D. Voracek, E. Reichenbach, and K. Griffin, “The X-53 A Summary of the Active Aeroelastic Wing Flight Research Program,” *48th AIAA/ASME/ASCE/AHS/ASC Structures, Structural Dynamics, and Materials Conference*, no. April, 2007.
- [7] R. S. Lakes, “Deformation mechanisms in negative Poisson’s ratio materials: structural aspects,” *Journal of Materials Science*, vol. 26, no. 9, pp. 2287–2292, 1991.
- [8] D. Prall and R. Lakes, “Properties of a chiral honeycomb with a poisson’s ratio of 1,” *International Journal of Mechanical Sciences*, vol. 39, no. 3, pp. 305–314, 1997.
- [9] P. Bettini, A. Aioldi, G. Sala, L. D. Landro, M. Ruzzene, and A. Spadoni, “Composite chiral structures for morphing airfoils: Numerical analyses and development of a manufacturing process,” *Composites Part B: Engineering*, vol. 41, no. 2, pp. 133–147, 2010.
- [10] A. Spadoni, M. Ruzzene, and F. L. Scarpa, “Global and local linear buckling behavior of a chiral cellular structure,” *Physica Status Solidi (B)*, vol. 242, no. 3, pp. 695–709, 2005.
- [11] J. Zhang and M. F. Ashby, “Buckling of honeycombs under in-plane biaxial stresses,” *International Journal of Mechanical Sciences*, vol. 34, no. 6, pp. 491–509, 1992.
- [12] L. J. Gibson and M. F. Ashby, *Cellular Solids: Structure and Properties*, vol. 7. 1999.

- [13] F. Scarpa, S. Blain, T. Lew, D. Perrott, M. Ruzzene, and J. R. Yates, “Elastic buckling of hexagonal chiral cell honeycombs,” *Composites Part A: Applied Science and Manufacturing*, vol. 38, no. 2, pp. 280–289, 2007.
- [14] W. Miller, C. W. Smith, F. Scarpa, and K. E. Evans, “Flatwise buckling optimization of hexachiral and tetrachiral honeycombs,” *Composites Science and Technology*, vol. 70, no. 7, pp. 1049–1056, 2010.
- [15] B. Haghpanah, J. Papadopoulos, D. Mousanezhad, H. Nayeb-Hashemi, and A. Vaziri, “Buckling of Regular, Chiral and Hierarchical Honeycombs under a General Macroscopic Stress State,” *Proceedings of the Royal Society A: Mathematical, Physical and Engineering Sciences*, vol. 470, no. 2167, p. 20130856, 2014.
- [16] G. Ramstein, *Experimental Validation of Chiral Structures with Local Controlled Instabilities*. Semester project no. 16-015, ETH Zürich, 2016.
- [17] D. Bornengo, F. Scarpa, and C. Remillat, “Evaluation of hexagonal chiral structure for morphing airfoil concept,” *Proceedings of the Institution of Mechanical Engineers, Part G: Journal of Aerospace Engineering*, vol. 219, no. 3, pp. 185–192, 2005.
- [18] A. Spadoni and M. Ruzzene, “Static Aeroelastic Response of Chiral-core Airfoils,” *Journal of Intelligent Material Systems and Structures*, vol. 18, no. October, pp. 1067–1075, 2007.
- [19] A. Spadoni and M. Ruzzene, “Numerical and experimental analysis of the static compliance of chiral truss-core airfoils,” *Journal of Mechanics of Materials and Structures*, vol. 2, no. 5, pp. 965–981, 2007.
- [20] a. Spadoni, M. Ruzzene, and F. Scarpa, “Dynamic Response of Chiral Truss-core Assemblies,” *Journal of Intelligent Material Systems and Structures*, vol. 17, no. November, pp. 941–952, 2006.
- [21] A. Airolidi, M. Crespi, G. Quaranti, and G. Sala, “Design of a Morphing Airfoil with Composite Chiral Structure,” *Journal of Aircraft*, vol. 49, no. 4, pp. 1008–1019, 2012.
- [22] A. Airolidi, P. Bettini, P. Panichelli, M. F. Oktem, and G. Sala, “Chiral topologies for composite morphing structures - Part I: Development of a chiral rib for deformable airfoils,” *Physica Status Solidi (B) Basic Research*, vol. 252, no. 7, pp. 1435–1445, 2015.
- [23] W. Raither, A. Bergamini, and P. Ermanni, “Profile beams with adaptive bending-twist coupling by adjustable shear centre location,” *Journal of Intelligent Material Systems and Structures*, vol. 24, no. 3, pp. 334–346, 2013.
- [24] A. Bergamini, R. Christen, B. Maag, and M. Motavalli, “A sandwich beam with electrostatically tunable bending stiffness,” *Smart Materials and Structures*, vol. 15, no. 3, pp. 678–686, 2006.
- [25] W. Raither, A. Bergamini, F. Gandhi, and P. Ermanni, “Adaptive bending-twist coupling in laminated composite plates by controllable shear stress transfer,” in *Composites Part A: Applied Science and Manufacturing*, vol. 43, pp. 1709–1716, 2012.

- [26] W. Raither, M. Heymanns, A. Bergamini, and P. Ermanni, “Morphing wing structure with controllable twist based on adaptive bending-twist coupling,” *Smart Materials and Structures*, vol. 22, no. JUNE 2013, p. 065017, 2013.
- [27] F. Runkel, A. Reber, G. Molinari, A. F. Arrieta, and P. Ermanni, “Passive twisting of composite beam structures by elastic instabilities,” *Composite Structures*, vol. 147, pp. 274–285, 2016.
- [28] R. Andreas, *Experimental investigation of the structural response of a wing model with structurally tailored buckling elements for morphing*. Master thesis no. 15-007, ETH Zürich, 2015.
- [29] N. Hu and R. Burgueño, “Buckling-induced smart applications: recent advances and trends,” *Smart Materials and Structures*, vol. 24, no. 6, p. 063001, 2015.
- [30] P. M. Reis, “A perspective on the revival of structural (in) stability with novel opportunities for function: From buckliphobia to buckliphilia,” *Journal of Applied Mechanics*, vol. 82, no. 11, p. 111001, 2015.
- [31] R. Vincenz, *Airfoil camber morphing exploiting chiral structures: Manufacturing and testing*. Semester project no. 17-041, ETH Zürich, 2017.
- [32] Dassault Systèmes, *Abaqus 6.14 Online Documentation*, 2014.

## **Appendix A: Python code generated**

All the code generated for this project can be downloaded from the following Github repository:  
<https://github.com/AlejandroValverde/abaqus.git>.